The Dissertation Committee for Vladimir Mancevski Certifies that this is the approved version of the following dissertation:

FABRICATION AND ANALYSIS OF CARBON NANOTUBE BASED EMITTERS

Committee:

John Markert, Supervisor

Zhen Yao

Chih-Kang Shih

Qian Niu

Benito Fernandez

FABRICATION AND ANALYSIS OF CARBON NANOTUBE BASED EMITTERS

by

Vladimir Mancevski, B.S.M.E., M.S.E.

Dissertation

Presented to the Faculty of the Graduate School of
The University of Texas at Austin
in Partial Fulfillment
of the Requirements
for the Degree of

Doctor of Philosophy

The University of Texas at Austin
August 2011

Dedication

This Dissertation is dedicated to my wife Teresa and my son Alex for believing in me and in my science and encouraging me to continue pursuing my dreams; to my father Aleksandar for his advice that I can do anything if I put my mind and effort to do it, to my mother Olivera who always encourages me to stay happy and positive; and to my American parents, Jack and Laura, who have been my leadership models and who have always been there for me.

Acknowledgements

I thank my colleague Paul McClure from Xidex for reading and editing every single research work done and every report that I have written, and checking this dissertation for logic and language. I also thank him for his helpful suggestions on the direction of the research I have conducted and for the analysis he did on the size of the light spots from the field emitters.

I thank Ryan Williams for spending numerous hours of work with me on the SEM and FIB tools, preparing field emitters and conducting experiments. His exceptional skills in SEM and FIB made many of the research ideas become practical. His ion milling work made the perfect base for emitters. I thank him for traveling with me to California to conduct the cool experiment on operating an SEM with a CNT emitter.

I thank Leonid Karpov from Xidex for the great and insightful suggestions on how to make a perfect field emission experiment and for his help in conducting some of the experiments. We have spent many hours discussing and interpreting the field emission results. I thank him for the great MEMS ideas on how to fabricate the emitter arrays.

I thank Philip Rack from The University of Tennessee at Knoxville and ORNL for his guidance in setting up and conducting the CNT editing experiments. I thank him for the numerous telephone and email discussions on how to interpret the results and in understanding the gas injection models they have developed. I also thank his student Matthew Lassiter for conducting the first set of water etching experiments at their SEM, and for performing the models of the localized pressure and etch rates.

I thank John Markert for being so patient with me over an extended period of time and for his encouragement to continue working on my Ph.D. degree while working at

Xidex. I thank him for the guidance in many of my experiments. I thank him for always having time to talk to me when I would drop by his office, even if not being scheduled; most of them not being scheduled. I thank him for helping me edit and prepare this Dissertation.

I thank Keith Stevenson from the Department of Chemistry and Biochemistry for his helpful advice with making and testing the field emitters. I thank Earl Weltmer from ScanService Corporation for letting us use his SEM as a test platform for the CNT emitters. I thank David Joy at the University of Tennessee at Knoxville and ORNL for providing support related to emitter design and interpretation of test results. I thank Victor Vartanian and John Allgair from International SEMATECH Manufacturing Initiative (ISMI) for funding the work on CNT electrical conductivity. I also thank Hal Bogardus for sponsoring early work done for SEMATECH and for encouragement in pursuing the work further. I thank Yong Lee for the initial information on how to build a nanomanipulator. I thank Boris Begus for the CAD designs of the nanomanipulator and the field emission rig.

Finally, I thank my wife Teresa and my son Alex for being patient with me when I had to juggle work and graduate work and for believing that I can do both. I thank them for their continuous support in everything I decide to do.

The research work presented here was partially funded by DOE grant number DE-FG02-06ER84408 and NSF grant number IIP-0712036.

FABRICATION AND ANALYSIS OF CARBON NANOTUBE BASED EMITTERS

Vladimir Mancevski, Ph.D.
The University of Texas at Austin, 2011

Supervisor: John Markert

We have advanced the state-of-the-art for nano-fabrication of carbon nanotube (CNT) based field emission devices, and have conducted experimental and theoretical investigations to better understand the reasons for the high reduced brightness achieved. We have demonstrated that once the CNT emitter failure modes are better understood and resolved, such CNT emitters can easily reach reduced brightness on the order of 10^9 A m^{-2} sr^{-1} V^{-1} and noise levels of about 1%. These results are about 10% better than the best brightness results from a nanotip emitter archived to date. Our CNT emitters have order of magnitude better reduced brightness than state-of-the-art commercial Schottky emitters. Our analytical models of field emission matched our experimental results well. The CNT emitter was utilized in a modified commercial scanning electron microscope (SEM) and briefly operated to image a sample.

We also report a successful emission from a lateral CNT emitter element having a single suspended CNT, where the electron emission is from the CNT sidewall. The lateral CNT emitters have reduced brightness on the order of 10^8 A m^{-2} sr^{-1} V^{-1}, about 10X less than the vertical CNT emitters we fabricated and analyzed. The characteristics of the lateral field emitter were analyzed for manually fabricated and directly grown CNT emitters. There was no significant difference in performance based on the way the CNT

emitter was fabricated. We showed that the fabrication technique for making a single CNT emitter element can be scaled to an array of elements, with potential density of 10^6-10^7 CNT emitters per cm^2.

We also report a new localized, site selective technique for editing carbon nanotubes using water vapor and a focused electron beam. We have demonstrated the use of this technique to cut CNTs to length with 10s of nanometers precision and to etch selected areas from CNTs with 10s of nanometers precision. The use of this technique was demonstrated by editing a lateral CNT emitter. We have conducted investigations to demonstrate the effects of higher local water pressure on the CNT etching efficiency. This was achieved by developing a new method of localized gas delivery with a nano-manipulator.

Table of Contents

List of Tables

List of Figures

Chapter 1: Introduction

The main subjects of research presented here are carbon nanotube (CNT) based devices, and in particular, carbon nanotube based field emitters. We have focused our research on discovering new fabrication methods for making CNT based devices and have analyzed their properties and figures of merit. We also present new tools that were developed in order to fabricate and/or analyze the CNT devices. Although our methods and devices were demonstrated with carbon nanotubes, the findings are applicable to other nanomaterials and nanodevices.

In this presentation we have dedicated a Chapter to each of the following related subjects: carbon nanotubes field emitters as sources for scanning electron microscopes, lateral nanotubes field emitters, and site selective carbon nanotube editing.

In Chapter 2 we present theoretical models for field emission from a carbon nanotube tip. We showed that the operation of the CNT emitter can be theoretically predicted by the Fowler–Nordheim equation in its simplified form. We verified the CNT field emission model with experimental data and found that the model fits well for a CNT nanotip and a similar Pt nanotip, both with 10s of nanometers diameter and a cylindrical shank. Chapters 4 and 5 of this work will use the above derived equations to demonstrate and analyze field emission from a CNT emitter.

In Chapter 3 we review the equipment and the components that were used, modified, and/or developed for the investigation conducted in Chapters 4 to 6. The instruments used for this work include a Scanning Electron Microscope (SEM), a nanomanipulator, a gas injection system, and a field emission testing vacuum chamber. SEMs are primarily used as imaging tools that allow viewing of nanometer sized objects and materials. There is a new trend in nanotechnology to use the SEM instrument as nanofabrication tool. Being on the forefront of this trend, we have developed a new type of nanomanipulator that was used to fabricate and investigate the CNT emitters, as described in Chapters 4 and 5. We also developed a new type of gas injection system that was used to improve the fabrication of the CNT emitters reported in Chapters 4 and 5. The emission testing vacuum chamber was built to help us investigate the CNT emitters.

In Chapter 4 we report on the experimental and theoretical investigations to better understand how to achieve CNT emitters with high reduced brightness, on the order of 10^9 A m^{-2} sr^{-1} V^{-1}, and noise levels of about 1%. We developed two fabrication methods for making CNT emitters using: manual mounting of carbon nanotubes and direct carbon nanotube growth. During this work we made and tested more than 40 different CNT emitters, either grown or mounted, and analyzed 27 CNT emitters. We investigated the failure mechanisms and found ways to improve the operation of the field emitter. As a result of the findings we advanced the state-of-the-art for nano-fabrication of CNT based field emission devices. A few CNT emitters were utilized in a modified commercial SEM and briefly operated to image a sample. Therefore, we demonstrated the proof-of-concept of operating an SEM instrument with a CNT emitter.

In Chapter 5 we present a new type of emitter, a lateral CNT emitter element having a single suspended CNT, where the electron emission is from the CNT sidewall. The lateral CNT emitters have reduced brightness on the order of 10^8 A m^{-2} sr^{-1} V^{-1}, about 10X less than the vertical CNT emitters we fabricated and analyzed in Chapter 4. However, the lateral CNT emitters are more suitable for operating in an array configuration. We showed that the fabrication technique for making a single CNT emitter element can be scaled to an array of elements, with potential density of 10^6-10^7 CNT emitters per cm^2. We developed two fabrication methods for making lateral CNT emitters using: manual mounting of carbon nanotubes and direct CNT growth. There was no significant difference in performance based on the way the CNT emitter was fabricated. We used the CNT editing methods described in Chapter 6 to modify and improve a lateral CNT emitter that was fabricated with a direct growth method described in Chapter 5.

In Chapter 6 we report a new localized, site selective technique for editing CNTs using water vapor and a focused electron beam. We investigated the relevant electron beam parameters (beam current and the beam energy) and determined their role in the electron beam-based CNT etching process. We also investigated the gas precursor parameters (localized precursor pressure, precursor flux, and precursor sample chemistry) and understood their role to the chemistry and physics of the carbon nanotube etching. We have conducted investigations to demonstrate the effects of higher local water pressure on the CNT etching efficiency. This was achieved by developing a new method of localized gas delivery with a nano-manipulator. As a result of these findings we have advanced the state-of-the-art of electron beam induced etching of carbon nanotubes. Finally, we have demonstrated the use of this technique to cut CNTs to length with 10s of nanometers precision and to etch selected areas from CNTs with 10s of nanometers precision.

Chapter 2: Theoretical Models of Carbon Nanotube Based Emitters

2.1 ELECTRON EMISSION OVERVIEW

Electron emission from the surface of a metal can occur due to thermionic emission, field emission, and Schottky emission, as shown in Figure 2.1. In a brief description we note that for thermionic emission to occur the material needs to be heated so as to give the electrons sufficient energy to overcome the potential barrier of the material. The potential barrier is known as work function ϕ. The physics of thermionic emission follows Richardson's Law in terms of the current density (J) from the source to the operating temperature (T).

The field emission process can be understood as follows. The metal can be considered a potential box, filled with electrons to the Fermi level, which lies below the vacuum level. The distance from Fermi to vacuum level is called the work function, ϕ. The vacuum level represents the potential energy of an electron at rest outside the metal, in the absence of an external field. In the presence of an electric field E the potential outside the metal will be deformed along a diagonal line so that a triangular barrier is formed, through which electrons can tunnel. Most of the emission will occur from the vicinity of the Fermi level where the barrier is thinnest. Since the electron distribution in the metal is not strongly temperature-dependent, field emission is only weakly temperature-dependent and would occur even at the absolute zero of temperature.

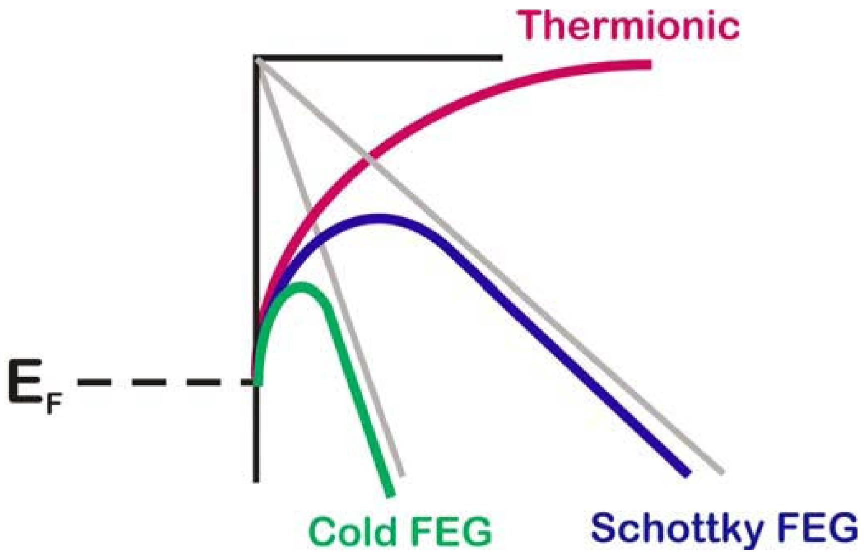

Figure 2.1: Illustration of the potential barrier of a metal surface with respect to a vacuum level. The barrier can be lowered by applying temperature as in thermionic emission, applying high electric field as in field emission, and applying both as in Schottky emission.

2.2 CNT FIELD EMISSION MODEL ANALYSIS

The carbon nanotube (CNT) based electron emitter is a field emitter which is operated by applying a strong electric field between the nanotube cathode and an anode separated some distance away from the cathode. The operation of the CNT emitter can be theoretically predicted by the Fowler–Nordheim theory [2.1, 2.2] which describes the field emission process in terms of a tunneling current through the potential barrier between a metal surface and a vacuum under influence of a strong electrical field.

The current density *J*, drawn from a point by field emission, for the one-dimensional Fowler–Nordheim case of a cold metallic planar emitter with parallel planar anode is known to be [2.2, 2.3]:

$$J = \frac{I}{S} = \frac{c_1}{\phi t(y)} F^2 exp\left(-\frac{c_2\,\phi^{\frac{3}{2}}\,v(y)}{F}\right) \qquad \text{Eq. 2.1}$$

where I is the electrical current flowing from surface S, ϕ is the emitter work function, F is the applied electric field, ε_0 is the permittivity of free space, and where, c_1

and c_2 are expressed in terms of universal constants (electron charge *e*, electron mass *m*, and Plank’s constant *h*) as:

$$c_1 = \frac{e^3}{8\pi h} = 1.541 \times 10^{-6}\,\frac{AeV}{V^2} \text{ and } c_2 = \frac{8\pi\sqrt{2}m}{3eh} = 6.831 \times 10^{9}\,\frac{V/m}{eV^{\frac{3}{2}}},$$

and where *t(y)* and *v(y)* are dimensionless functions of *y*:

$$y = \left(\frac{e^3 F}{4\pi\varepsilon_0\phi^2}\right)^{\frac{1}{2}}.$$

It has been shown that in the case of a triangular potential barrier the functions *t(y)* and *v(y)* can be approximated to be unity [2.3]. Therefore the simplified Fowler–Nordheim equation can be expressed as:

$$J = \frac{I}{S} = c_1 \frac{F^2}{\phi} exp\left(-c_2 \frac{\phi^{\frac{3}{2}}}{F}\right) = 1.54 \times 10^{-6} \frac{F^2}{\phi} exp\left(-6.83 \times 10^{9} \frac{\phi^{\frac{3}{2}}}{F}\right) \qquad \text{Eq. 2.2}$$

This model of the Fowler–Nordheim equation has been proven to work for field emission from sharp tips up to temperatures of several hundred °C, after which the other two emission mechanisms, Schottky emission and thermionic emission, play a role. Saito et al. [2.4] have noticed that an additional correction may be necessary for the case of CNTs since the density of states in CNTs is not energy independent around the Fermi level as it is the case for metals. Nevertheless, experimental results have confirmed that field emission from CNTs can be described to a first approximation by the simple Fowler–Nordheim equation (Eq. 2.2), and this is the approximation used here.

We will now review how to compute the field emitter parameters from the experimental *I-V* curve and the Fowler–Nordheim equation. The experimental setup is shown in Figure 2.2.

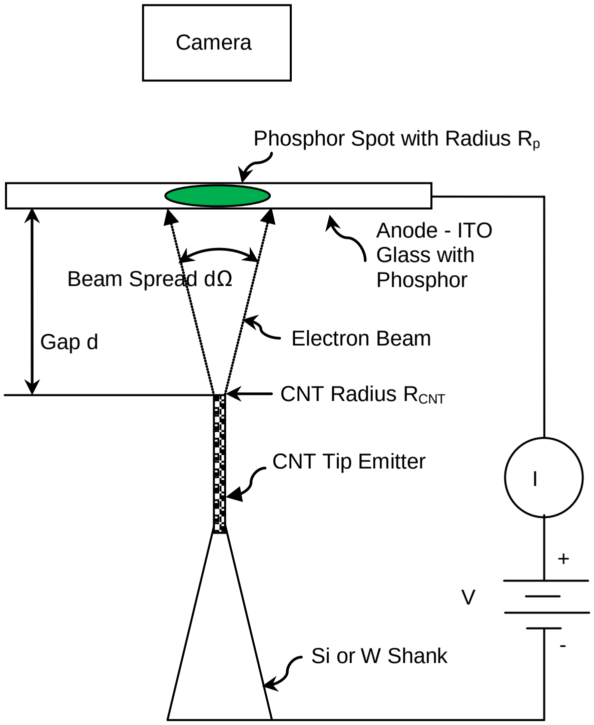

Figure 2.2: Schematic drawing of a CNT emitter experiment with key parameters annotated.

The electric field F at the surface of a free sphere with radius R at potential V is given by:

$$F = \frac{V}{R} \qquad \text{(Eq. 2.3a)}$$

However, in the presence of a tip shank the electric field is reduced, so that the electric field has to be adjusted by a correction factor k. Therefore, the electric field from a sharp tip, such as a carbon nanotube with a hemispherical cap of radius R_{CNT}, can be approximated by as:

$$F = \frac{V}{k\ R_{CNT}} \qquad \text{(Eq. 2.3b)}$$

The experimental value of k for a hemisphere on a thin cylinder has been estimated to be $k = 5$. In reality the field strength also depends on the real shape of the tip, the tip shank, and the cathode-anode distance but in first order approximation of the field emission phenomena these factors can be neglected. In our analysis we will use this first order approximation. In cases where other effects are significant, numerical simulation can be used to solve for the electric field for any tip and tip-shank shape and cathode-anode distance.

Substituting for F as described in Eq. 2.3b into Eq. 2.2 we get:

$J=\frac{I}{S}=c_1\,\frac{V^2}{k^2R_{CNT}^2\,\phi}\,exp\left(-c_2\,\frac{\phi^{\frac{3}{2}}}{V}\,k\,R_{CNT}\right)$, which can be rewritten as:

$\frac{I}{V^2}=c_1\,\frac{S}{k^2R_{CNT}^2\,\phi}\,exp\left(-c_2\,\phi^{\frac{3}{2}}\,k\,R_{CNT}\,\frac{1}{V}\right)=A_k\,exp\left(-B_k\,\frac{1}{V}\right)$, (Eq. 2.4a)

where, $A_k=c_1\,\frac{S}{k^2R_{CNT}^2\,\phi}$ $and\ B_k=c_2\,\phi^{\frac{3}{2}}\,k\,R_{CNT}$, are functions of the measured radius of the emitter R_{CNT}, the estimated or measured work function of the emitter material ϕ, the estimated correction factor k, and the unknown emitting area S. In logarithmic terms, Equation 4a can also be written as:

$\ln[\frac{I}{V^2}]=\ln[A_k]-B_k\,\frac{1}{V}$. (Eq. 2.4b)

A linear fit of experimental current-voltage (I-V) data to a Fowler-Nordheim approximation indicates an evidence of field emission. From the slope and the ordinate intercept line of the best linear fit in the $ln\left[\frac{I}{V^2}\right]\ vs\ \frac{1}{V}$ plot one can determine several key parameters of the field emission. In particular we can compute the correction factor k, the apparent emitting area S, and the virtual source R_V. If the linear fit is expressed as:

$ln\left[\frac{I}{V^2}\right]=-Intercept-Slope\,\frac{1}{V}$, where *Intercept* and *Slope* are experimentally determined values. Then according to Eq. 2.4a:

$A_k=c_1\,\frac{S}{k^2R_{CNT}^2\,\phi}=\exp(-Intercept)=A\ and$ (Eq. 2.5a)

$B_k=c_2\,\phi^{\frac{3}{2}}\,k\,R_{CNT}=Slope=B$ (Eq. 2.5b)

From these relations the correction factor k can be computed as:

$k=\frac{B}{c_2\,\phi^{\frac{3}{2}}R_{CNT}}$ (Eq. 2.5c)

And the apparent emitter area S can be computed as:

$S=\frac{A\,k^2R_{CNT}^2\,\phi}{c_1}$ (Eq. 2.5d)

Substituting Eq. 2.5c into 2.5d we get:

$S=\frac{A}{c_1}\left(\frac{B}{c_2\phi}\right)^2$ (Eq. 2.5e) where the apparent emitter area S only depends on the *I-V* coefficients and the work function ϕ. For an emitter with a circular cross section, like a closed end CNT, the virtual source R_v can be computed from the apparent emitter area S as:

$$R_v = \sqrt{\frac{S}{\pi}} \qquad \text{(Eq. 2.5f)}$$

Therefore, the correction factor k, the apparent emitter area S, and the virtual source R_v can all be computed from the linear fit of the experimental *I-V* data.

The electric field F can also be expressed in terms of the applied voltage V, the electrode gap d, and a field enhancement factor β that takes into account the shape and the size of the tip and its support:

$$F = \beta \frac{V}{d} \qquad \text{(Eq. 2.6)}$$

Substituting for F as described in Eq. 2.6 into Eq. 2.2 we get:

$J = \frac{I}{S} = c_1 \frac{\beta^2 V^2}{d^2\,\phi} exp\left(-c_2 \frac{\phi^{\frac{3}{2}}}{V\,\beta} d\right)$, which can be rewritten as:

$$\frac{I}{V^2} = c_1\, S\, \frac{\beta^2}{d^2\,\phi} exp\left(-c_2 \frac{\phi^{\frac{3}{2}}}{V\,\beta} d\right) = A_\beta\, exp\left(-B_\beta \frac{1}{V}\right), \qquad \text{(Eq. 2.7a)}$$

where, $A_\beta = c_1\, S\, \frac{\beta^2}{d^2\,\phi}\ and\ B_\beta = c_2 \frac{\phi^{\frac{3}{2}}}{\beta} d$ are functions of the measured electrode gap d, the estimated or measured work function of the emitter material ϕ, the estimated field enhancement factor β, and the unknown emitting area S. In logarithmic terms, Equation 7a can also be written as:

$$\ln\left[\frac{I}{V^2}\right] = \ln[A_\beta] - B_\beta \frac{1}{V}. \qquad \text{(Eq. 2.7b)}$$

Again, if the linear fit to the experimental current-voltage (*I-V*) data is expressed as:

$ln\left[\frac{I}{V^2}\right] = -Intercept - Slope\ \frac{1}{V}$, where *Intercept* and *Slope* are experimentally determined values, then according to Eq. 2.7a:

$$A_\beta = c_1\, S\, \frac{\beta^2}{d^2\,\phi} = \exp(-Intercept) = A\ and \qquad \text{(Eq. 2.8a)}$$

$$B_\beta = c_2 \frac{\phi^{\frac{3}{2}}}{\beta} d = Slope = B \qquad \text{(Eq. 2.8b)}$$

From these relations the field enhancement factor β can be computed as:

$$\beta = c_2 \frac{\phi^{\frac{3}{2}}}{B} d \qquad \text{(Eq. 2.8c)}$$

And the apparent emitter area S can be computed as:

$$S = \frac{A\, d^2\ \phi}{c_1\, \beta^2} \qquad \text{(Eq. 2.8d)}$$

Substituting Eq. 2.8c into 2.8d we get:

$$S = \frac{A}{c_1} \left(\frac{B}{c_2 \phi} \right)^2 \qquad \text{(Eq. 2.8e)}$$

where the apparent emitter area S only depends on the I-V coefficients and the work function ϕ. For an emitter with a circular cross section, like a closed end CNT, the virtual source R_V can be computed from the apparent emitter area S as:

$$R_v = \sqrt{\frac{S}{\pi}} \qquad \text{(Eq. 2.8f)}$$

Therefore, field enhancement factor β, the apparent emitter area S, and the virtual source R_V can all be computed from the linear fit of the experimental I-V data.

The virtual source of an electron emitter with a circular cross section, like a closed end CNT, is the area $S = \pi R_V^2$ from which the electrons appear to originate when they are traced back along their trajectories. We show in the above description that the apparent emitter area S can be computed from the experimental I-V coefficients and the work function ϕ.

It is important to know whether this model applies to a virtual source of a CNT emitter. de Jonge et al. [2.5] experimentally measured the size of the virtual source using TEM imaging and a point projection microscope and concluded that the use of the advanced Fowler–Nordheim equation (Eq. 2.1) produced larger discrepancies in the computation of the virtual source than the simple Fowler–Nordheim equation (Eq. 2.2). de Jonge et al. propose that there are generally three types of CNT ends and that each of them has a different virtual source radius r_V. For CNT tips with a hemispherical CNT cap, such as the one illustrated in Figure 2.3a, the virtual source radius r_V can be computed as we have derived in Eq. 2.5. However, for a CNT with a flat cap, as illustrated in Figure 2.3b, they propose that the virtual source radius $r_V \approx R - R_c$, where R

is the CNT radius and *R_c* is the CNT thickness. Finally, for a CNTs with an open cap, as illustrated in Figure 2.3c, the virtual source radius r_v can be assumed to be the radius *R* of the CNT.

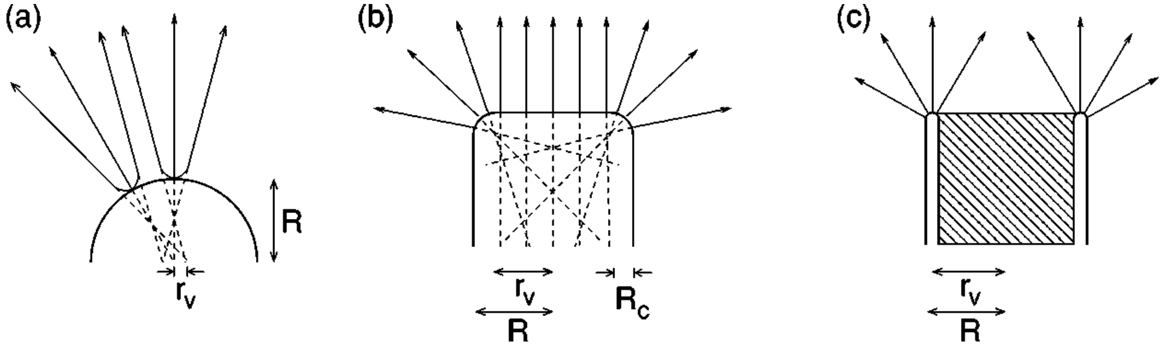

Figure 2.3: Models of virtual source for carbon nanotube emitters. (a) virtual source r_v for a CNT with hemispherical cup, (b) with flat cup, and (c) with open cup. Reprinted from N. de Jonge [2.5]

The radius of the virtual source R_v is used to compute the reduced brightness B_r, the most important performance parameter for field emission. The reduced brightness B_r measures the amount of current that can be focused into a spot of a certain size from a certain solid angle and can be computed as:

$$B_r = \frac{I}{d\Omega\, \pi\, R_v^2\, V} = \frac{I_r'}{\pi\, R_v^2}\left(\frac{A}{m^2\ sr\ V}\right) \qquad \text{(Eq. 2.9)}$$

where *I* is the emission current (A), *dΩ* is the solid angle of the electron beam spread (steradians), I_r' is the reduced angular current density (A sr^{-1} V^{-1}), R_v is the radius of the virtual source (m), and *V* is the applied extraction voltage to the emitter (V).

The solid angle of the electron beam spread *dΩ* (steradians) can be computed from the radius of the phosphor spot R_p on the surface of the ITO-Phosphor anode and the anode-cathode distance *d*:

$$d\Omega = 2\tan^{-1}\left(\frac{R_p}{d}\right)\frac{180°}{\pi}\,(°),\ \text{and} \qquad \text{(Eq. 2.10a)}$$

$$d\Omega = 2\pi\left\{1 - \cos\left[\tan^{-1}\left(\frac{R_p}{d}\right)\right]\right\}\ (sr) \qquad \text{(Eq. 2.10b)}$$

The angular current density *I'* and the reduced angular current density *I_r'* of the emitter can be computed as:

$$I' = \frac{I}{d\Omega}\left(\frac{A}{sr}\right), \text{ and} \qquad \text{(Eq. 2.11a)}$$

$$I_r' = \frac{I}{d\Omega\,\mathrm{V}}\left(\frac{A}{sr\ V}\right) \qquad \text{(Eq. 2.11b)}$$

2.3 MODEL VERIFICATION WITH EXPERIMENTAL RESULTS

We will now demonstrate the use of the CNT field emission model to derive the emitter parameters from experimental data. We have conducted field emission from three types of nanotips, CNT emitter tip (end-radius of ~5 nm), cylindrical Pt nanotips (cylinder with cone end, 33 nm diameter, 1.1 μm high, ~14 nm end-radius) and Si tips (cone, 15 μm high, ~10 nm end-radius). The Pt and Si nanotips were used for comparison to the CNT tip. All three samples were tested in the same anode-cathode holder and vacuum chamber. The data acquisition procedures were also the same. Multiple runs were conducted and the *I-V* characteristics of the average numbers are shown in Figure 2.4.

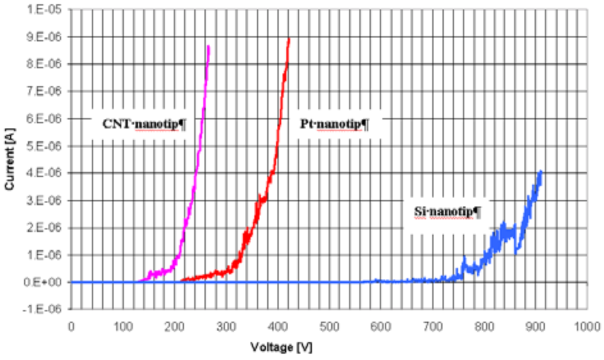

Figure 2.4: I-V plots of three nanotip field emitters, CNT, Pt, and Si. The anode-cathode gap was 60 μm.

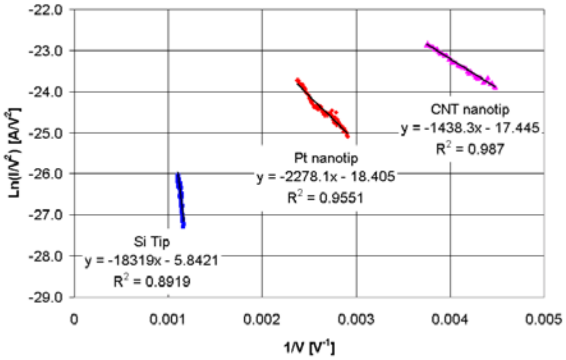

Figure 2.5: Fowler-Nordheim plot and a linear fit for CNT nanotip, Pt nanotip, and Si tip.

The recorded average threshold voltages were 1.9 V/μm for CNT, 2.9 V/μm for Pt, 8.6 V/μm for Si tips. CNT and Pt nanotips were tested at emission currents of 10 μA.

The corresponding Fowler-Nordheim plot is presented in Figure 2.5. The linearity of the results, expressed through linear fit parameters, was good, meaning that we are observing true field emission from the nanotips. From the liner fit we can measure the Slope and the Intercept for each tip, as presented in Table 2.1:

Table 2.1: Experimental parameters extracted from the Fowler-Nordheim plot for three different nanotips

	CNT	**Pt**	**Si**
Intercept	-17.445	-18.405	-5.8421
A=exp(Intercept)	2.6×10^{-8}	1.0×10^{-8}	2.9×10^{-3}
B = Slope	1438.3	2278.1	18319
Linear Fit	0.987	0.9551	0.8919
Tip Radius (nm)	5	7	10

With experimental data from Table 2.1 and using Eq. 2.5c the correction factor k can be computed. With experimental data from Table 2.1 and using Eq. 2.8c the field enhancement factor β can be computed. With experimental data from Table 2.1 and using Eq. 2.8e the emitter area S can be computed. For an emitter with a circular cross section, the virtual source R_V can be computed from the apparent emitter area S using Eq. 2.8f. Table 2.2 shows the results of these computations:

Table 2.2: Computed field emitter parameters for three different nanotips

	Equation	**CNT**	**Pt**	**Si**
Correction factor k	2.7c	3.8	4.0	27.2
Field enhancement factor β	2.10c	3186	2168	221
Emitter Area S (nm^2)	2.7e, 2.10e	30.5	26.5	6×10^{8}
Virtual Tip R_v (nm)	2.7f, 2.10f	3.1	2.9	14,275
Physical Tip Radius (nm)		5	7	10

The results show that for CNT and Pt the virtual source radius is smaller than the physical radius indicating that it is real. For real nanotips, such as CNT and Pt, which resemble a spherical emitter on a cylindrical shank, the Fowler–Nordheim approximation (Eq. 2.2) works well as shown by the results for the nanotips. For nanotips that deviate from the model, such as the case with the Si tip that has large conical shank, the Fowler–Nordheim approximation fails and the resulting virtual radius is computed to be much larger than the physical radius which is not possible.

Chapters 4 and 5 of this work will use the above derived equations to demonstrate and analyze field emission from a CNT emitter.

Chapter 3: Instrumentation and Components

In this Chapter we briefly describe the equipment and the components that were used for the experiment to familiarize the reader with the experimental setup. The instruments used for this work include a Scanning Electron Microscope, a Nanomanipulator, a Gas Injection System, and a Field Emission Testing Vacuum Chamber.

3.1 SCANNING ELECTRON MICROSCOPE (SEM)

The majority of the experiments presented in this work were conducted in a Hitachi S-4000 non-environmental SEM equipped with a custom built gas delivery/injection system and a custom built nanomanipulator, as shown in Figure 3.1. This SEM was located at Xidex Corp. in Austin TX. This SEM was used for fabrication of CNT emitters, evaluation of the CNT emitters, and for conducting experiments with water assisted CNT editing. A second SEM used for the conducting CNT editing experiments was a Hitachi S-4300SE/N variable pressure scanning electron microscope (VPSEM), as shown in Figure 3.2, located at The University of Tennessee at Knoxville. Also used for fabrication of CNT emitters and their evaluation was a dual-beam Focused Ion Beam (FIB) and SEM tool, FEI Strata DB235 equipped with a Zyvex S100 nanomanipulator. This tool was located at The University of Texas at Austin, in particular, at the Texas Materials Institute and Center for Nano- and Molecular Science. Finally, some of the FIB ion-milling used in the fabrication of the lateral CNT emitters was conducted with FIB tools located at SEMATECH in Austin TX (prior to their relocation out of Austin).

Figure 3.1: Hitachi S-4000 SEM used for conducting the CNT editing experiments and for fabricating CNT emitters.

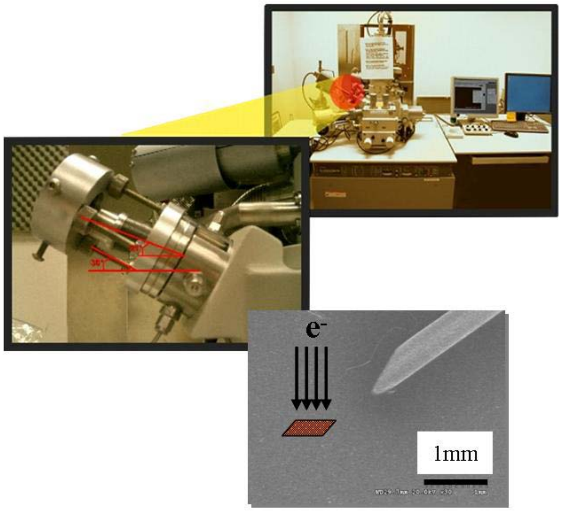

Figure 3.2: Hitachi S-4300SE/N SEM and customized gas injection system.

SEMs are primarily used as imaging tools that allow viewing of nanometer sized objects and materials, such as carbon nanotubes, Pt and W nanowires, gold nanoparticles, and other nanostructures and nanomaterials. There is a new trend in nanotechnology to use the SEM instrument as nanofabrication tool. For example with the help of nanomanipulators, such as the NanoBot® nanomanipulator [3.1], we can fabricate CNT based Scanning Probe Microscope (SPM) tips and CNT based emitters, which is the subject of this work. With the help of gas injection systems, such as the Parallel Gas Injection System (PGIS) [3.2], we can conduct electron beam induced etching and deposition (EBIE/EBID) of materials inside the SEM, equivalent to a “nano-welding” process. For example EBIE/EBID can be used to fabricate (attach and cut to length as an example) the CNT emitters we report in this work.

The basic principle of a SEM is to eject a stream of electrons originating from an emitter (cold, thermionic, or Schottky), accelerate these electrons towards a sample, and focus them along the way, so that the electrons interact with the sample, and then detect the secondary electrons (SE) and/or back-scattered electrons (BSE) resulting from the electron-sample interaction. Secondary electrons result from inelastic scattering of the electrons from the sample atoms. This is the most common mode of SEM imaging. Back scattered electrons result by elastic scattering of the electrons from the sample atoms.

The SEM controls include its beam energy, beam current, and scan rates. We used all three parameters to control the editing of CNTs as described in more detail in one of the Chapters of this work. Beam energy can be varied by changing the accelerating voltage. Typical SEM acceleration voltages are in the range of 1 to 30 keV, where lower acceleration voltage produces lower beam energy. Lower beam energy does not charge the sample but also produces lesser quality of image and vice versa for the higher energy. The beam current is proportional to the flux of electrons. The incident beam current is measured by a Faraday cup connected to a digital picoammeter. Typical beam currents are in the range of pA to nA. The beam current can be modified by adjusting the condenser lens settings, as well as by use of variable, current-limiting apertures. The condenser lens concentrates (or demagnifies) the beam of electrons into a spot. The size of the beam can therefore be adjusted. Typical analog condenser lens settings are from 1 to 10 where a higher number means smaller beam size and therefore lower beam current. Typical computer controlled beam sizes are 1 to 5 where lower beam size means lower beam current. Other types of control are: beam scanning rates, pixel dwell time, and refresh rates. These parameters are unique to the SEM tool and the application. The above parameters play an important role in the EBIE/EBID processes, including the CNT editing that is subject to our work. For example we found that conditions for CNT editing are 10 microsecond dwell time, 1 ms frame refresh rate, and 30 loops per second in a line scan mode. The SEM operates in high vacuum mode with typical pressure ranges from $5.0\text{x}10^{-4}$ Pa to $2.0\text{x}10^{-2}$ Pa.

3.2 IN-SITU NANOMANIPULATOR

For the needs and requirements of our research work we have built a custom 3-axis inertial slider type nanomanipulator that can operate inside the SEM chamber, as shown in Figure 3.3. Each axis of the nanomanipulator consists of a stainless steel (SS) base, a linear piezo element, a graphite bearing, and a SS slider that is clamped on the bearing. In this assembly the piezo element is epoxied to the SS base using common high vacuum epoxy, such as Varian Torr Seal. The graphite element is also epoxied to the piezo element. The SS slider is clamped to the graphite bearing with two screws and a beryllium copper spring inserted between the screw and the slider. The presence of the spring allows us to control the clamping force between the slider and the bearing. The nanomanipulator was able to move in 3 orthogonal axis, X, Y, and Z, with range of 15 mm by sliding along. At each point the piezo could operate as an ordinary piezo element with ranges of ± 2.3 µm for voltages of ± 40 V. The resolution of this slider was measured to be 1 nm and was only limited by the noise of the applied voltage.

The principle of operation of the inertial slider is as illustrated in Figure 3.4. As shown in Figure 3.4a, the piezo element expands together with the graphite bearing that is fixed to it. As shown in Figure 3.4b, the slider also moves forward along with the graphite bearing since static friction is holding the slider clamped to the bearing. After expanding with a desired amplitude the piezo element contracts quickly, exceeding the static friction limit and allowing the bearing to return back to its original position while the slider was left in the same place as the before the piezo contracted, as shown in Figure 3.4c. If this motion is repeated consecutively the slider will advance with each step while the piezo and the bearing keep moving forward and backward. Clearly the key to the motion is to expand and contract the piezo with a sawtooth pattern. During the slow slope of the sawtooth the slider advances and during the fast slope of the sawtooth the slider is left in place while the piezo and the bearing return back to zero, as shown in Figure 3.4d.

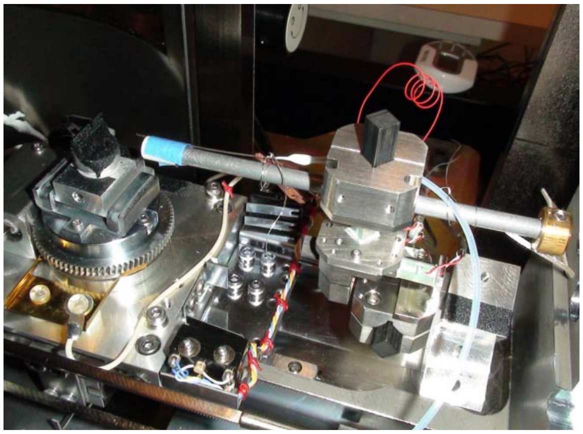

Figure 3.3a: A custom 3-axis nanomanipulator that was designed and build for the purposes of conducting the experiments presented in our research.

Figure 3.3b: A commercial NanoBot® nanomanipulator, currently manufactured by Xidex Corp. that is based on the prototype from Figure 3.3a.

The direction of the motion can be reversed by reversing the sawtooth pattern. The amplitude and frequency of the sawtooth can be used to control the speed of the slider motion. If the sawtooth is applied only once then the slider is going to move only a single step. This manner of operation allows for precise stage (slider) positioning. If the piezo element is slowly expanded or contracted that causes the slider to move along with it, remaining attached by static friction. This approach allows for fine positioning with 1 nm resolution. Our approach to driving the inertial slider was to produce the sawtooth signals with a Data Acquisition (DAQ) board that was operated with a software application. In particular the control software we used was LabView based and the sawtooth signals were produced with a National Instruments DAQ board, such as NI-6229 M series DAQ board.

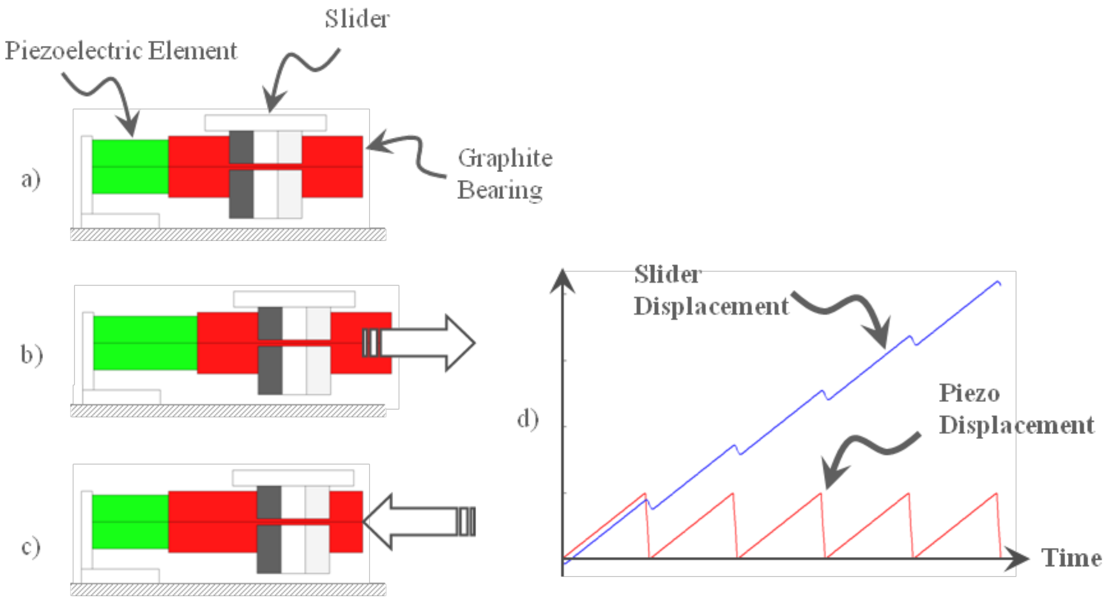

Figure 3.4: The principle of operation of an inertial linear stage

3.3 GAS INJECTION SYSTEM

Our research objectives required that we develop a custom gas injection system (GIS) that would enable selective CNT etching at reduced background pressures suitable for a non-environmental SEM instrument. Most conventional gas injection systems, like the ones found in FIB tools, are based on a simple one-dimensional design which allows the nozzle to move in only one direction, towards the center of the system, at the intersection between the beam and the stage, to bring the nozzle close to the sample. Using this conventional system the nozzle can be moved in XYZ from outside the vacuum chamber within about 0.5 mm from the sample and with low precision of 100s of microns. An example of a conventional gas injection system head with mechanical wobble stick positioning control is shown in Figure 3.5. This is the system used by our collaborators at the University of Tennessee. Our requirement was to have a GIS that can enable closer approach of the nozzle and with better positioning precision.

Our custom gas injection system solution was to fix the gas injection nozzle to a precision XYZ nanomanipulator to allow positioning of the gas delivery nozzle 10s of microns away from the sample and with equally good precision. Figure 3.6 shows the schematic of the concept. In one option of operation the gas reservoir is located outside of the SEM chamber, and in Option#2 the gas reservoir is located inside the SEM chamber.

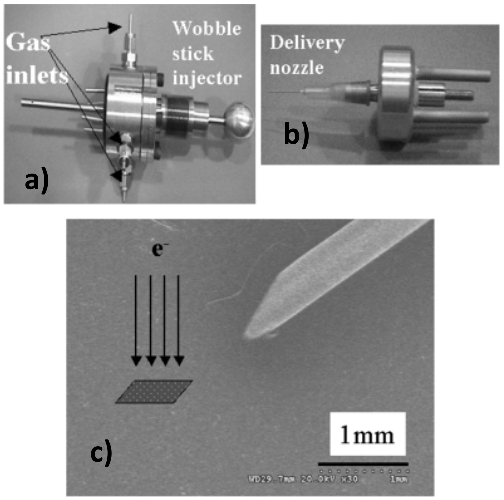

Figure 3.5: Photographs of a) the gas injection flange, b) the gas delivery needle, and c) an SEM micrograph of the delivery needle in close proximity to the substrate.

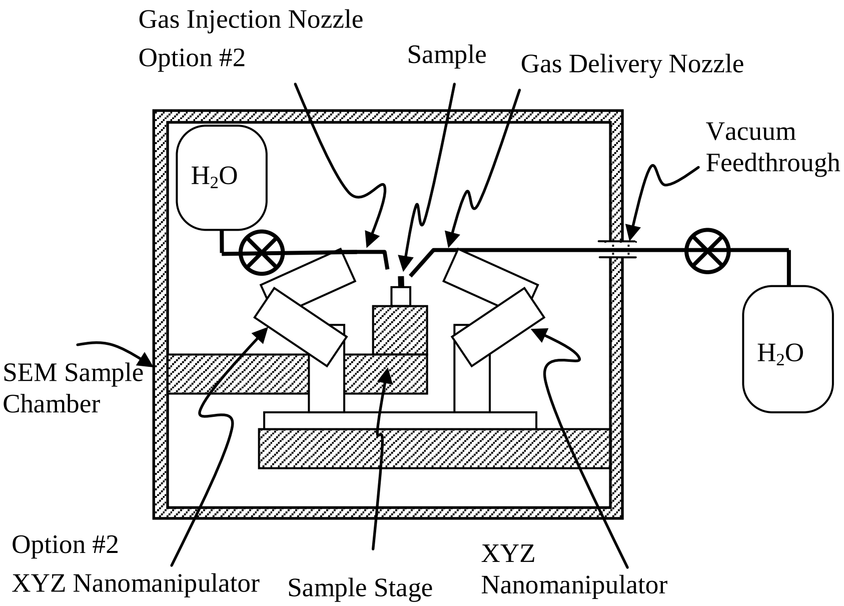

Figure 3.6: Schematic of a gas injection system with a nozzle attached to a nanomanipulator for precise nozzle positioning. Option 2# has the gas reservoir inside the chamber.

For our first prototype we conducted a proof-of-concept trial in which we temporarily modified a FIB tool by installing an in-situ gas bottle which connected to a needle attached to a nanomanipulator, as shown in Figure 3.7. This enabled us to position the end of the gas precursor nozzle within the field of view of the electron beam and also to vary the range from 78 to 466 µm from the CNTs to be edited. The chamber pressure varied from 2 to 9×10^{-3} Pa but was variable and constantly changing because of the selected in-situ gas delivery bottle. We were able to use this system to cut individual CNTs as well as to clean a 200 nm x 200 nm area from a web of CNTs lying on the surface but the results were inconsistent and not repeatable. However the success in the initial phase of work showed the potential of delivering a localized precursor gas. The Chapter on CNT editing describes in detail the construction of the complete custom GIS and the experiments that were conducted with it.

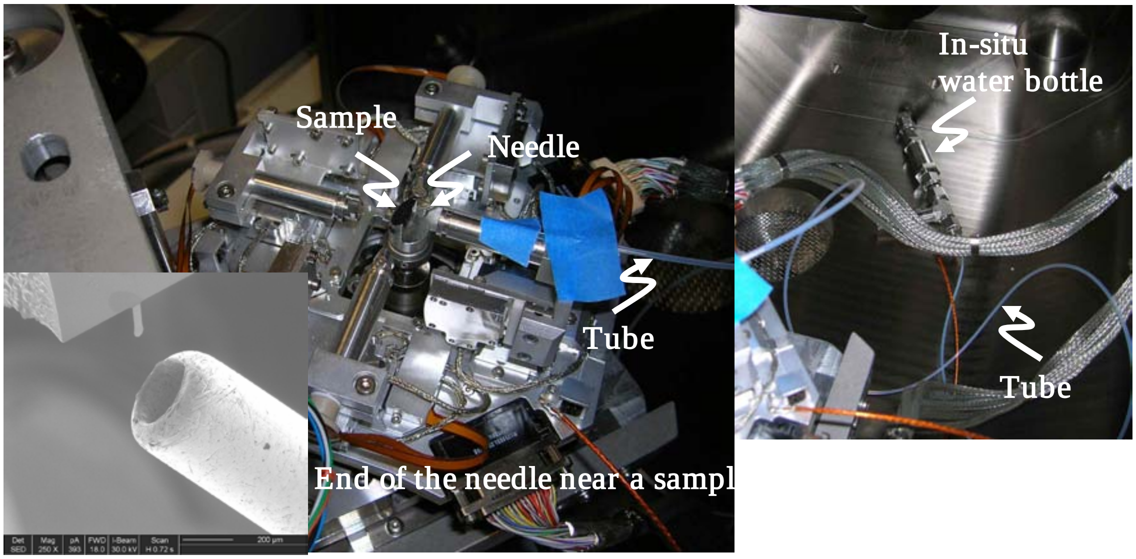

Figure 3.7: Prototype gas delivery system with a nozzle on a nanomanipulator and with in-situ gas-liquid bottle. Insert shows the end of the needle ~200 µm from the

3.4 FIELD EMISSION EVALUATION HARDWARE

The performance of the CNT field emitters was investigated in a vacuum test chamber specially built and dedicated for the field emission experiments. The specialized vacuum test chamber consists of a pumping station and a cylindrical vacuum chamber with a view-port, as shown in Figure 3.8. The pumping station consists of a turbo-pump backed by a mechanical pump. The best vacuum level we have been able to achieve with this station is 2×10^{-7} Torr. All the experiments were conducted at this level of vacuum so as to demonstrate the utility of our CNT emitters in a high vacuum environment. The vacuum is measured using a cold-cathode vacuum gauge that can measure vacuum down to 1×10^{-8} Torr.

We used two types of sample holders, one for CNT emitters fabricated on a silicon substrate and another for CNT emitters fabricated on a sharpened tungsten wire. The former sample holder is made of two parallel glass plates coated with gold or aluminum. The CNT emitter is fixed to the cathode plate with a carbon paste where the anode plate is positioned above the emitter. The spacing is controlled with precision machined Macor and quartz spacers. The later sample holder is made of a wire holder with a set screw and a metal coated glass plate perpendicular to the wire. The anode-cathode spacing is controlled by setting the gap under an optical microscope.

For diode type field emission measurements the electrical field was supplied with a Keithley 237 current-voltage source that can provide up to 1100 V of bias. The *I-V* tests ware run with an automated system consisting of LabView based software and National Instruments hardware.

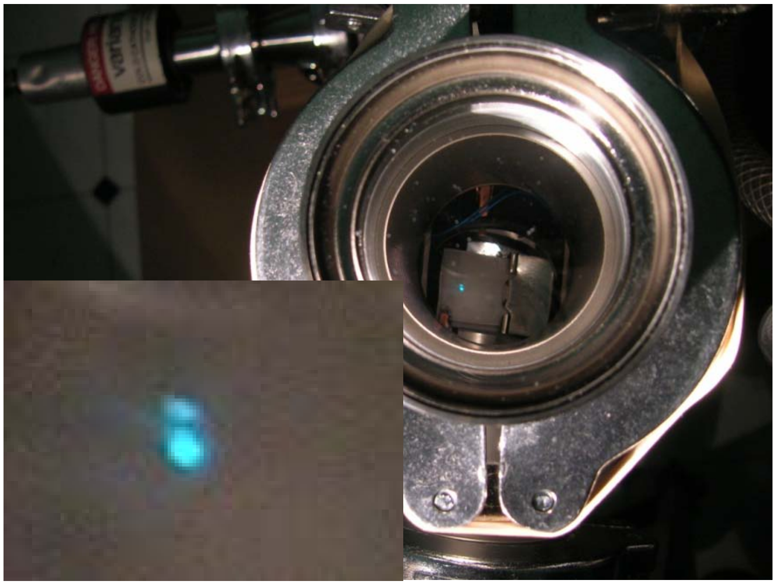

Figure 3.8: The field emission test chamber with viewport. As an example, inside the chamber is an array of CNT emitters with tip to tip spacing of about 270 µm. The bright spots are due to the electrons hitting a phosphor coated ITO glass.

Chapter 4: Carbon Nanotube Field Emitters as Sources for Scanning Electron Microscopes

4.1 INTRODUCTION

Many industries, including the semiconductor industry, as well as the emerging nanotechnology industry, depend on scanning electron beam instruments, such as field emission scanning electron microscopes (FE-SEMs), Schottky emitter based SEMs (for example, critical dimension SEMs), and transmission electron microscopes (TEMs), to develop new processes and products, control existing processes and stimulate new innovations in materials science. Currently there is a need for significant improvement in the spatial resolution, signal-to-noise ratio, and processing speed of these imaging tools. This need can be met by improving either the electron optical column or the electron source. Electron optical columns have improved significantly in the last 10-15 years [4.1], however, the field emission source itself has basically not changed. The spatial resolution of scanning electron beam instruments can be improved by a field emission source with higher brightness, lower energy spread, and smaller emitter size [4.1, 4. 2, 4.3, 4.4]. An electron source with higher brightness can focus a larger amount of current into a spot of a given size, resulting in shorter image acquisition time and faster processing speed [4.2]. Smaller source size improves the source brightness by reducing the spatial angular spread of the beam [4.4]. In addition, smaller source size lowers the energy spread (distribution width) [4.4]. In scanning electron beam instruments the source size of the emitter determines how much demagnification must be applied by the electron optics of the column to achieve the desired resolution, where less demagnification means better tool signal-to-noise ratio [4.1].

Furthermore, SEM / TEM users who utilize scanning electron microscopes for high-precision measurements, such as those in the semiconductor industry, are also concerned about emission stability. Precision is the gauge of how repeatable the measurements are. For example, for semiconductor SEM users, a loss in precision means that bad products are declared good or good products are declared bad, resulting in diminished product yield. Fluctuations, noise, spikes, and drift of the emission current all affect the short and long term stability of the electron beam and therefore the precision of the microscope. The electron emission stability of the emitter depends on the quality of the emitter, its erosion, its resilience to contamination and other environmental factors.

Finally, most SEM / TEM users care about long emitter lifetime and the availability of commercial emitters. Long emitter lifetime reduces tool downtime and lost productivity by reducing the frequency of changing the SEM / TEM filament and reducing the frequency of tool calibration. Commercial SEM / TEM users are also interested in the commercial availability of emitters as opposed to hearing and reading about another "one-time" laboratory success that cannot be replicated or produced in commercial quantities.

Therefore, the desired characteristics of an ideal emitter for scanning electron beam instruments are high brightness, low energy spread, small emitter size, high emission stability, long emitter lifetime, and commercial emitter availability. The presented research will ultimately enable better field emitters for high-performance electron beam instruments.

4.1.1 Conventional Cold Field Emitters

Conventional cold field emitters have advantages over Shottky based thermal field emitters and thermionic field emitters because they do not require power consumption for heating, they do not require evaporation of cathode material, they have slightly better brightness, lower energy spreading, and reasonable emitter lifetime if the emitter is maintained (flashed or briefly heated by applying large current pulse) frequently [4.5]. Most common conventional cold field emitters are made of tungsten and have a conical geometry with apex radius of 100 to 150 nm. Because of their advantages cold field emitters are the preferred filaments for field emission SEMs / TEMs where high imaging resolution is desired.

Disadvantages of conventional cold field emitters are their delicate environmental stability and their susceptibility to contamination, leading to bad emission stability. In particular, conventional cold field emitters, which are subject to being sputtered by ionized residual gas molecules, are inclined to undergo chemical reactions with molecules or ions of residual gases, and can change their work function and electron affinity in the presence of ions or molecules on the emitter surface. The result of the above interactions is emitter noise, field current reduction, and ultimately a destructive shortening. As a result of their disadvantages the conventional cold field emitters require high vacuum operation and need frequent flashing to eliminate any contaminants from their surface.

One approach to circumvent the disadvantages of the cold field emitters and keep the advantages of the Shottky based thermal field emitters is to use nanotip field emitters. Qian et al. [4.6] and Purcell et al. [4.4] have demonstrated that nanotips offer higher brightness and lower energy spread because of their small tip radius.

4.1.2 Nanotip Emitters

Nanotip emitters, by comparison to all conventional cold, thermally assisted, and Schottky field emitters, offer a significant increase in brightness (10 to 100 times) and large reduction (5 to 10 times) in source size. Use of nanotips is also expected to reduce the Boersch effect as a result of a reduction in the total emitted current from the source and the possibility of removing focal crossovers in the beam path.

We will shown that the best candidates for nano-sized high-aspect-ratio cylindrical nanotips are carbon nanotube (CNT) nanotips. We next overview the advantages of carbon nanotubes as promising field emitters through literature review.

The existing state-of-the art emitter sources are ZrO/W Schottky emitters with high reduced brightness B_r (2×10^8 A m^{-2} sr^{-1} V^{-1}), low energy spread (0.8 eV), a good emission stability (less than 0.5%) and long lifetime (years) [4.2, 4.7]. Existing cold field emitter sources are W emitters that have compatible (slightly better) reduced brightness and lower energy spread (0.3 eV), but they have inferior emission stability (5%) [4.2] and shorter lifetime (few months) than Schottky emitters.

4.1.3 Emitter Brightness

The reduced brightness B_r measures the amount of current that can be focused into a spot of a certain size from a certain solid angle:

$$B_r = I / (d\Omega\, \pi\, r_V^2\ V) = I' / (\pi\, r_V^2\ V) \qquad \text{(Eq. 4.1)}$$

where I is the emission current (A), $d\Omega$ is the solid angle of the electron beam spread (steradians), I' is the angular current density (A sr^{-1}), r_V is the radius of the virtual source (m), and V is the extraction voltage applied to the emitter. For nanotips with small radius, a conservative estimate of the radius of the virtual source can be assumed to be the radius of the nanotip, $r_V = R_{NT}$. Therefore, the brightness of an electron source is better for smaller diameter nanotip and for higher emission currents at given extraction voltage.

Several groups have directly or indirectly demonstrated that CNT nanotip emitters have much better brightness then state-of-the art Schottky emitters or W cold field emitter sources. de Jonge et al. [4.2, 4.8, 4.9, 4.10] have conducted comprehensive experiments to directly determine the brightness of carbon nanotube field emitters. Using a set of carbon nanotubes with lengths of about 1 µm and radius of less then 10 nm, de Jonge has demonstrated an average value of the reduced angular current density of the carbon nanotubes of 30 nA sr^{-1} V^{-1}. The reduced-brightness for an individual carbon nanotube emitter was between 1.3 and 2.5×10^9 A m^{-2} sr^{-1} V^{-1}, and order of magnitude better than the values of state-of-the-art commercial emitters. Hata et al. [4.11] have also demonstrated very high reduced-brightness for carbon nanotube emitters, 5.6×10^9 A m^{-2} sr^{-1} V^{-1}. These are the best brightness results from a nanotip emitter archived to date. The nanotubes used in this experiment were 20 nm in diameter and were typically mounted manually on a conductive wire for the purposes of their evaluation.

Guillorn et al. [4.12] indirectly show that good brightness can be achieved from a nanotip. They demonstrated that less than 1% of the current emitted from carbon nanofibers was collected by the gate, therefore indicating an excellent electron beam collimation (small beam spreading). The size of the beam spread was not measured directly. The advantage of this demonstration was that the nanotips were grown directly on the substrate instead being manually mounted. The disadvantage of this demonstration is that the nanotips were not cylindrical and were large. The nanotubes used in this experiment were grown directly on a substrate using Plasma Enhanced CVD. Their typical base diameter was 200 nm, with tip diameter of 15 nm, and height of 1 μm.

4.1.4 Emitter Stability and Lifetime

One of the great advantages of carbon nanotube emitters is their demonstrated emission stability and long lifetime. Carbon nanotubes are far more resistant to sputtering from ionized residual gas molecules than conventional field emission cathodes composed of refractory metals [4.9, 4.13]. Carbon nanotube emitters also experience negligible surface diffusion in the presence of large electric fields. Nanotube emitters also are inert with respect to many residual gasses [4.9].

Dean et al. [4.14] have demonstrated excellent long-term (over 350 hours) field emission stability from single wall carbon nanotube emitters with diameter of 0.7 to 1.2 nm. They tested the stability of the carbon nanotube emitter under influence of purified H_2O, Ar, H_2, and O_2. The carbon nanotube emitters only showed susceptibility to damage by oxygen. Metal field emitters that were subjected to the same environmental tests self-destructed after 10 hours. The conclusion of the finding was that carbon nanotube emitters are more stable in poor vacuum then metal emitters. The advantage of the carbon nanotube emitters was attributed to the emitter geometry, strong carbon bonding, and lack of unwanted protrusion growths. Hsu et al. [4.15] have discovered that treating the carbon nanotube emitters in a hydrogen environment produced an enhancement of the carbon nanotube based field emission. Furthermore, carbon nanotube emitters that have been degraded in oxygen can increase their emission current 340-fold after being exposed to hydrogen.

Bonard et al. [4.5] have investigated the current stability of individual carbon nanotube emitters at a vacuum level of 10^{-7} mbar and found switching type current fluctuations at lower currents. The emission was more stable at higher currents and at deeper vacuum levels. An individual nanotube emitter was found to be stable for more than 100 hours at 2 µA current. In another investigation Bonard et al. [4.3] have demonstrated a field emission of more than 1400 hours at 0.5 µA at 4×10^{-7} mbar. Hsu et al. [4.16] demonstrated that short term stability of carbon nanotube emitters was 5% from the emission current but that there was general drift of the current. Fransen et al. [4.17] have demonstrated a short-term stability of 1.2% in a continuous run that took 54 days. The emission stability of any emitter may be regulated to some extent with a simple feedback loop that keeps the emission current constant. de Jonge et al. [4.9] have reported short-term current fluctuations of less than 0.5 % with the help of feedback loop.

4.1.5 Other Field Emitter Figures of Merit

Utsumi [4.18] demonstrates that an ideal shape for a field emitter is a sphere but that a “rounded whisker” (a cylindrical emitter where the radius of the hemispherical end of the tip is half its diameter) geometry is the closest to the ideal sphere geometry. Therefore, a very effective means of achieving large enhancement factors is to use high aspect-ratio cylindrical tips as we propose here.

Another figure of merit for nanotip emitters is the maximum current density. The carbon nanofibers fabricated by Melechko et al. and Guillorn et al. [4.19, 4.20] exhibited maximum emission current of 5 μA, corresponding to a current density of 500 kA/cm^2 (5×10^9 A/m^2). de Jonge et al. [4.2] have demonstrated catastrophic failure of the carbon nanotube emitter at currents of 200 μA for a carbon nanotube with diameter of 20 nm, corresponding to a current density of 6×10^{10} A/m^2. Bonard et al. [4.5] have demonstrated catastrophic failure of the carbon nanotube emitter at currents of 200 μA for a carbon nanotube with diameter of 8 nm, corresponding to a current density of 4×10^{12} A/m^2.

Summary of the competing state-of-the-art emitter technologies to our CNT emitters is presented in Table 4.1.

Table 4.1: Summary of the competing state-of-the-art emitter technologies

	ZrO/W Schottky Emitters	**Sharp W Emitters**	**CNT Emitters (Expected)**
Brightness [A / (m^2 sr V)]	2×10^8	3×10^8	2.5×10^9
Energy Spread [eV]	0.8	0.3	0.2 – 0.3
Stability [%]	< 0.5 %	< 5 %	0.5 - 5 %
Lifetime	years	months	months to years

4.2 FABRICATION

4.2.1 Fabrication of Carbon Nanotube Field Emitters

The CNT emitters used in this research were fabricated using two alternative methods: manual mounting of carbon nanotubes and direct carbon nanotube growth. The method of direct carbon nanotube growth was demonstrated only for a silicon substrate (Figure 4.1a). The method of manual mounting was demonstrated for sharp silicon tip substrate (Figure 4.1b) and sharpened tungsten substrate (Figure 4.1c). During this work we made and tested more than 40 different CNT emitters, either grown or mounted, and analyzed 27 CNT emitters.

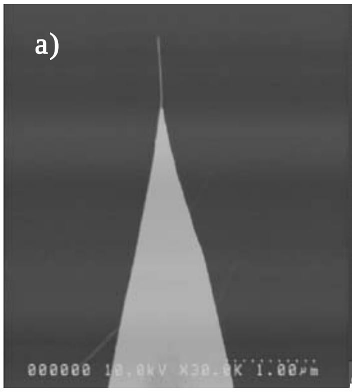

Figure 4.1a: CNT emitter grown directly on Si tip

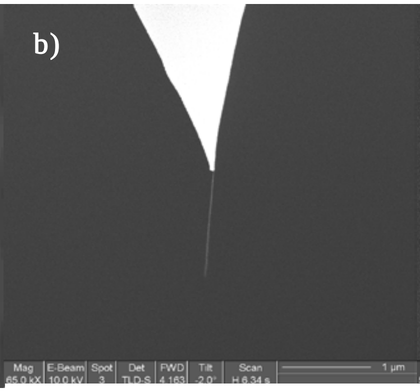

Figure 4.1b: CNT emitter manually mounted on a Si tip

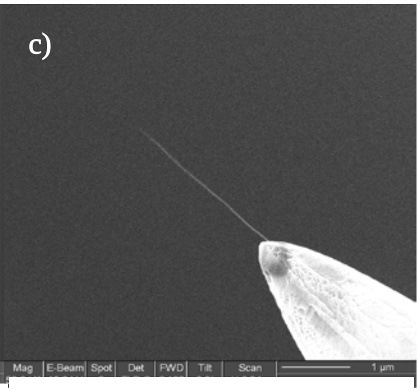

Figure 4.1c: CNT emitter manually mounted on a sharpened W tip

4.2.2 Manual Mounting

Manual mounting of CNTs is the most common approach for fabricating CNT tips and emitters. The following issues arise when one attempts to fabricate CNT emitters or tips.

a) Published information shows that researchers' main supply of nanotubes for mounting are nanotubes fabricated using arc-discharge or CVD growth and either dispensed in a solvent solution or collected on a carbon tape. Either approach requires additional processing or handling of the CNTs that can contaminate the CNTs.

Our approach to the supply of nanotubes was to grow straight, clean, high quality carbon nanotubes directly on the edge of a silicon substrate using thermal CVD process. Afterwards, the CNT can be directly picked up from the Si substrate without any intermediate preparation process. The tips fabricated in this research used this method.

b) Typically, manual CNT mounting procedures take place inside an SEM chamber and with the help of a nanomanipulator. It is common procedure to first contact the CNT to a sharp W tip, and then attach the CNT to the W tip by applying glue to the CNT-W junction or by depositing carbon from hydrocarbon contamination to the CNT-W junction. Alternatively one can also deposit metal from a metal precursor source instead carbon. Afterwards the CNT is pulled out from the bundle by retracting the tip. With this approach there is no control over the length of the CNTs and after one failed attempt the W probe (with the failed CNT) have to be replaced.

Our method of attaching the CNT to the tip (Si or W) was to first contact the CNT with the tip. The presence of Van der Waals force will snap any small diameter CNT to the tip where it would stay in contact unless the tip is pulled away from the CNT. In practice any CNT with diameter of 40 nm or less would readily snap to a W or Si tip. Applying a current pulse, producing current induced Joule heating, would cut the CNT away from the substrate and will attach it to the W tip. Although the length of the CNT is not precisely controlled, there is some control over the length of the CNT. The added benefit of this approach is that for each mounted CNT we know the current limits that would cause its cutting and destruction. This information was used to estimate the maximum current that can be applied to each CNT emitter. More detailed description of the manual CNT mounting procedure is presented in Appendix A (also reference [4.21]) and recorded on a YouTube video [4.22]. For a more controlled fabrication of a CNT emitter tip we have used a water vapor induced CNT etching/cutting approach that is described in detail in Chapter 6 of this work.

c) Most CNT tips are fabricated with lack of control over the alignment of the CNT with respect to the substrate. However, it is desired to have an aligned CNT emitter with respect to the mounting substrate. The alignment assures that the CNT apex is the closest point to the anode and the source of the electron emission.

There is very limited research and published information that describes a method of aligning a CNT emitter after it has mounted on a W wire. Park et al. [4.23] has described use of Focused Ion Beam (FIB) to align a carbon nanotube on a silicon substrate and use it as a scanning probe tip.

Our method of aligning the CNT emitter was to use a FIB beam for an alignment, after the CNT has been mounted on the W wire. The results of this approach are shown in Figure 4.2.

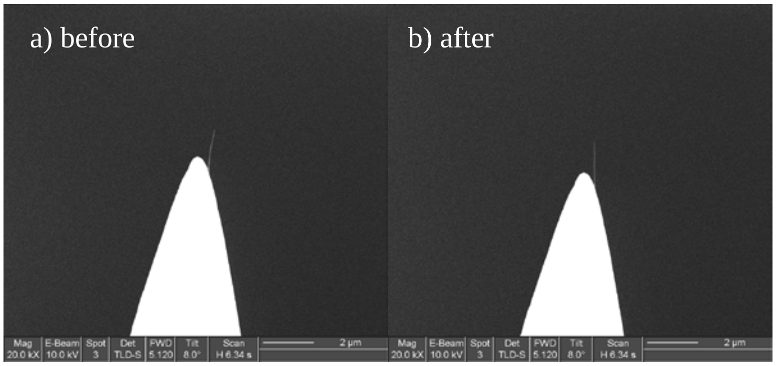

Figure 4.2: Illustration of focused ion beam assisted carbon nanotube alignment. a) CNT before alignment, b) CNT after alignment

A CNT that was irradiated with a low dose of Ga^+ ions (for example by operating the ion beam with low 10 pA beam current) tended to align itself in the direction of the ion beam. The conductivity of the CNT after the Ga^+ irradiation had increased. The mechanism of the increase is not well understood but it could be the removal of defects in the CNT lattice, the removal of contaminants from the CNTs, or a deposition of Ga atoms on the CNT. In general, the FIB aligned CNT emitters performed better then non-aligned CNT emitters.

d) Another variation in the fabrication of CNT emitters on sharp W tips was to change the sharpness of the W tip. We produced electrochemically sharpened W tips with average end radius of 25 - 50 nm, as shown in Figure 4.3a. Well known methods and apparatuses were utilized for tip etching/sharpening. We also tested the use of focused ion beam (FIB) sharpening of W wires which were previously electrochemically sharpened, to produce W tips with 5 - 10 nm end radius that proved to be the best base for the CNT emitters, as shown in Figure 4.3b. The results show that CNT emitters made on sharper W tips performed better then the CNT emitters made on blunter W tips. This indicates that the end radius of the W tips plays a greater role in defining the electrostatic screening effect (the shield effect) than we had anticipated.

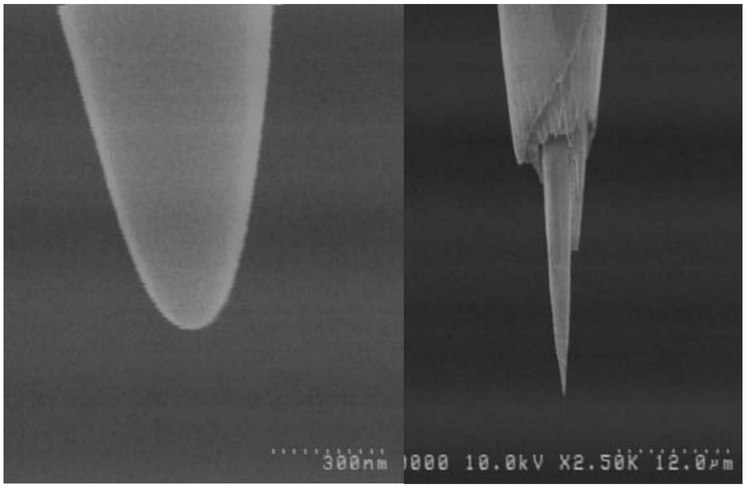

Figure 4.3: Examples of a) electrochemically sharpened W tip, and b) focused ion beam sharpened W tip

4.2.3 Direct CNT Growth

The method of direct carbon nanotube growth was demonstrated only for a silicon SPM substrate. The procedure was as follows. Standard silicon based SPM tips, such as

Budget Tap 300 [4.24], were first cleaned with clean and dry compressed nitrogen to remove any large contaminants. Subsequently, the tips were carefully dipped into solutions containing catalytic material. The SPM tips were then placed in a CVD oven and the CNTs were grown using thermal CVD process. Typical CVD recipes were conducted with a flow rate of Ar/H_2 1000-2000 sccm to 1 sccm of ethylene at growth temperature of 750°C for 10 minutes. The flow of the carrier gas and the precursor gas into the CVD oven were slowed down until a single CNT would statistically grow on 1 out of 5 CNT tips. Most tips would have multiple CNTs or single not well positioned or aligned CNT tip. A CNT tip successfully fabricated by this method of directly growing a single nanotube at the apex of a sharp silicon tip is shown in Figure 4.4. CNT emitters grown on silicon SPM substrates cannot easily be mounted on standard scanning electron beam instruments but are great test samples used to study the mechanism of CNT emission.

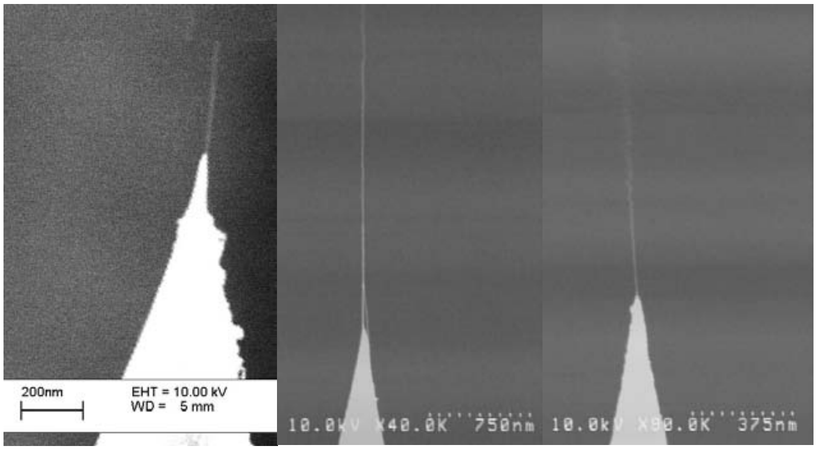

Figure 4.4: Gallery of carbon nanotube tips grown directly on silicon SPM tips. Average CNT diameter is ~ 10 nm.

4.2.4 Competing Nanotube Tip Fabrication Processes

In contrast to our thermal CVD process is the Plasma Enhanced CVD process for growing aligned carbon nanofibers directly on a substrate. This method of carbon nanotube fabrication is for example practiced by the Meyyappan group from NASA Ames Research Center and the Molecular-Scale Engineering and Nanoscale Technology Research Group at Oak Ridge National Laboratory (ORNL). The ORNL group was also very involved in fabricating “vertically aligned carbon nanofibers” (VACNFs) as field emitters for the flat panel display applications. The disadvantages of the Plasma Enhanced CVD process is that small diameter (less than 50 nm) multiwalled CNT are hard to produce. In addition, the carbon nanotubes grown with the plasma enhanced CVD method are relatively contaminated with graphite and other oxide and nitride contaminants. Typical carbon nanofibers fabricated by Melechko et al. and Guillorn et al. [4.19, 4.20] are quite large and conical, with base diameter of 200 nm, tip diameter of 25 nm, and height of 2 µm. Therefore, we believe that VACNFs are not suitable as field emitters for scanning electron beam instruments.

Other research groups have fabricated carbon nanotube based emitters directly on the substrate but they have not been able to achieve the quality and the rate of production that we have. For example, Minh et al. [4.25] demonstrated a fabrication process for growing carbon nanotube emitters with diameter from 4 to 200 nm on top of sharp Si tips and have demonstrated a field emission from an individual nanotube. Zhang et al. [4.26] have demonstrated a fabrication process for depositing carbon nanotube emitters on W tips via dielectrophoresis. The disadvantage of this fabrication method is that most of the time the nanotip is comprised of bundles of nanotubes staggered on top of each other until one protrudes further than the others. We do not know if there are unwanted effects of this staggered tip on field emission. Nevertheless, Zhang et al. [4.26] have demonstrated field emission from an individual carbon nanotube emitter, deposited on the W tip via dielectrophoresis, with 50 nm diameter exhibiting maximum emission current of 5 µA and a modest current density of 2.5×10^5 A/m^2. The beam divergence of this field emitter was unusually large, 50°.

4.2.5 Emitter Fabrication Improvements

The baseline CNT emitter was fabricated on W or Si tip and was tested. The electrical tests of the CNT emitters as they were fabricated showed that the electrical connection between the CNT and the substrate varied and was not consistent. Therefore, we improved the CNT emitter fabrication process by depositing carbon and platinum on the CNT-substrate junction with a goal to improve the electrical connection. The C and the Pt were deposited using electron beam induced metal deposition techniques with the help of a Gas Injection System. More detailed study of the electrical properties of a CNT tip is presented in Appendix B. The results of the improved CNT emitter fabrication on the performance of the CNT emitter are discussed in the results section below.

4.2.6 Field Emission Testing Hardware

The field emission test rig that used in this research is shown in Figure 4.5. The electrical field for emission measurements was supplied with Keithley 237 current-voltage source that can provide up to 1100 V of bias. The data collection was done with an automated system consisting of LabView based software and National Instruments hardware that are already available on one computer.

We used two types of sample holders, one for CNT emitters fabricated on a silicon substrate and another for CNT emitters fabricated on a sharpened tungsten wire. The wire sample holder is shown in Figure 4.6. The phosphor plate is not shown in this Figure.

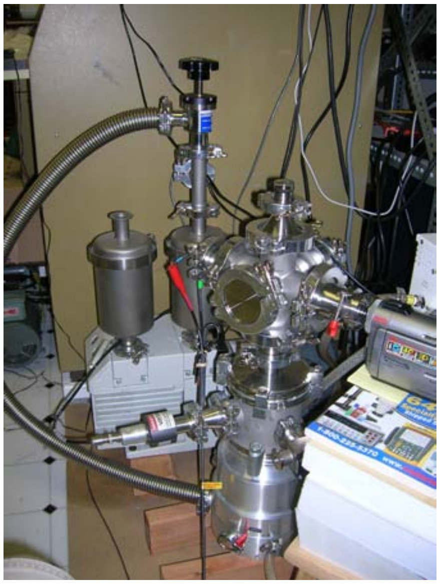

Figure 4.5: Field emission testing rig.

Figure 4.6: Holder for testing CNT emitters on W wire

4.3 EXPERIMENTAL RESULTS

4.3.1 Measurement and Evaluation of CNT Emitters

The field emission figures-of-merit measured during this research were: high reduced brightness, high reduced angular current density, small virtual source size, small emitter size, low noise, stability, and long lifetime.

The most important figure-of-merit about the performance of the CNT emitter is the reduced brightness. The reduced brightness B_r measures the amount of current that can be focused into a spot of a certain size from a certain solid angle and was computed according to:

$$B_r = I / (d\Omega \, \pi \, R_v^2 \; V) = I_r' / (\pi \, R_v^2) \qquad \text{(copy of Eq. 1)}$$

where I is the emission current (A), $d\Omega$ is the solid angle of the electron beam spread (steradians), I_r' is the reduced angular current density (A sr^{-1} V^{-1}), R_v is the radius of the virtual source (m), and V is the applied extraction voltage to the emitter (V).

The independent parameters measured were: the I-V curves, the emission current I, the applied extraction voltage V, the radius of the field emission pattern, and the radius of the CNT emitter R_{CNT}. We also had to measure the tip-to-anode distance d, and we had to assume the work-function for a carbon nanotube ϕ. From these known parameters we computed: the solid angle of the electron beam spread $d\Omega$, the angular current density I', the reduced angular current density I_r', the field enhancement factor β, the virtual source size R_v, and the reduced brightness B_r.

The spread of the electron beam $d\Omega$ was measured indirectly by measuring the radius of the emission pattern on a phosphor screen located distance d away from the emission source. The image of the field emission pattern was digitally recorded with a camera and its radius was determined with intensity analysis (see Figure 4.7). To assure that the spread of the electron beam $d\Omega$ was measured from a stable emitter we measured the emission current for the duration of recording the image of the field emission pattern.

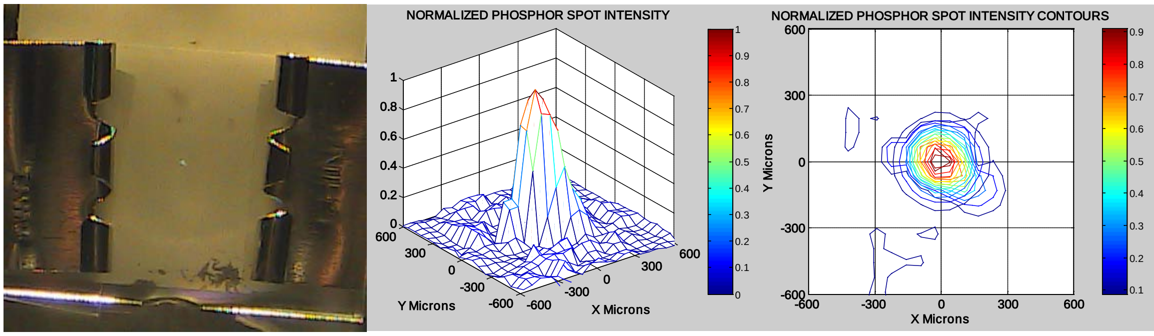

Figure 4.7: a) The image of the field emission pattern digitally recorded with a camera, where its radius was determined with intensity analysis (in this example R was 87 µm for a gap of 408 µm), b) normalized intensity plot, c) normalized contour plot.

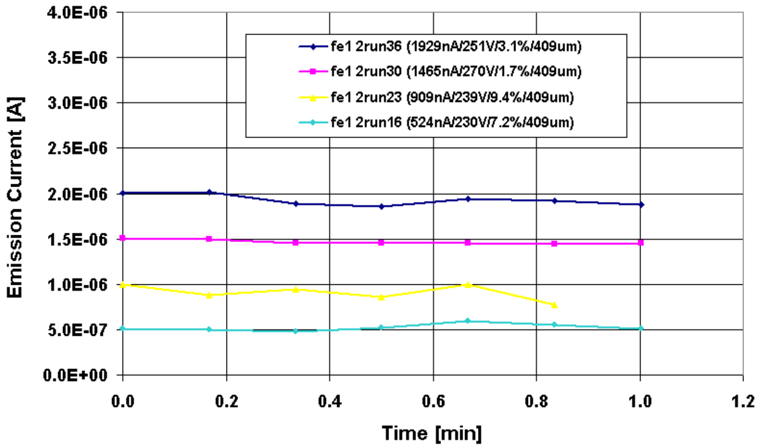

Figure 4.8: Field emission as recorded during brightness measurements for Emitter #1. Legend: (average current/extraction voltage/current noise/gap)

Figures 4.8 and 4.9 show the average emission current and the current noise for Emitter #1 and Emitter #2 respectively. The images of the field emission pattern for Emitter #1 were measured at four different current levels, as shown in Figure 4.8. The images of the field emission pattern for Emitter #2 were measured at three different tip-to-anode distances, as shown in Figure 4.9. From the radius of the bright spot and the tip-to-anode distance d we computed the solid angle of the electron beam spread $d\Omega$ (steradians). The typical tip-to-anode distance was in the range of 50 µm up to 800 µm which resulted in typical solid-angle beam spread in the range of 0.067 steradians to 0.482 steradians (full cone angle of 16.8° to 45.2°). Due to the small tip-to-anode distance the field emission pattern was not magnified enough to observe the emission from the individual atoms at the end of the nanotube but it was enough to measure the spread of the electron beam.

The ratio between the emission current I and the beam spread solid-angle $d\Omega$ gives us the angular current density I', and the angular current density I normalized with respect to the extraction voltage V gives as the reduced angular current density I_r'.

Typical angular current density ranges measured were 2-22 (μA sr^{-1}) and the reduced angular current density 11-81 (nA sr^{-1} V^{-1}).

The radius of the virtual source R_V was derived from the measured I-V curves, as described in Chapter 2. First, it is assumed that the I-V curves from the nanotube field emission follow the Fowler-Nordheim approximation for field emission. A linearity of the data in a Fowler-Nordheim plot, expressed through linear fit parameters, indicates an evidence of a field emission. Therefore, from the slope and the ordinate intercept line of the best linear fit one can determine the parameters of the field emission curve (see Figure 4.10). Fitting the I-V curve into a Fowler-Nordheim plot we can extract the enhancement factors β, the apparent emitting area S, and the virtual source R_V. The results of testing two CNT emitters at different currents (Emitter #1) and at different tip-to-anode distances (Emitter #2) showed virtual source radius ~2.2 nm, a realistic result for CNTs with known radius of 5 nm.

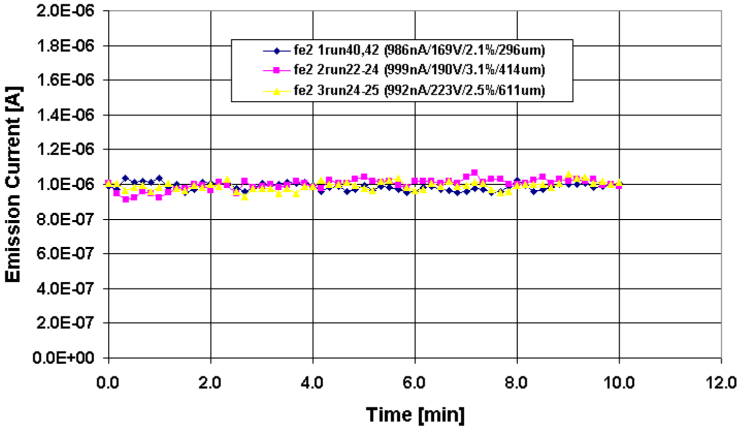

Figure 4.9: Field emission (average of 2 or 3 runs) as recorded during brightness measurements for Emitter #2. Legend: (average current/extraction voltage/current noise/gap)

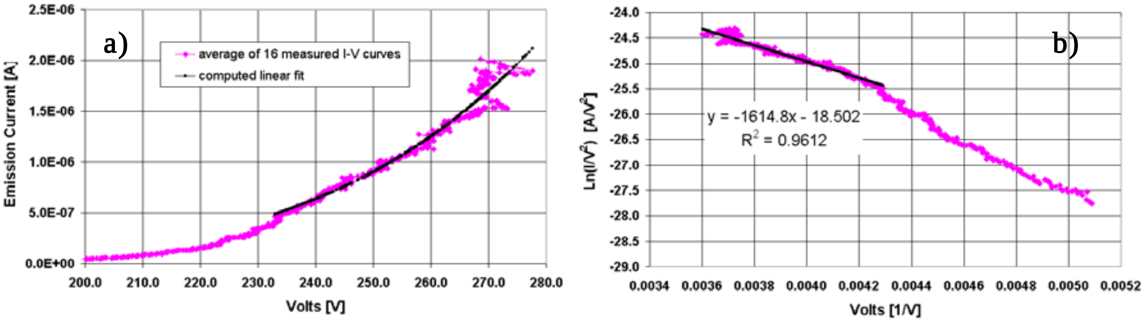

Figure 4.10: Data for Emitter #1 tests, a) average of 16 measured I-V curves and the computed fit for the high current regime, b) corresponding Fowler-Nordheim plot and the computed linear fit for the high current regime.

From the computed reduced angular current density I_r' and the radius of the virtual source R_v we computed the reduced brightness B_r of the CNT emitters. The best reduced brightness B_r achieved was 6.1×10^9 and 2.1×10^9 A m^{-2} sr^{-1} V^{-1} for Emitter #1 and Emitter #2 respectively. Tables 4.2 and 4.3 show a summary of the best experimentally determined figures-of-merit related to the reduced brightness. Table 4.2 shows the summary of the figures-of-merit for Emitter #1 which was tested at varying currents levels and Table 4.3 shows the summary for Emitter #2 which was tested at varying tip-to-anode distances. Computation of the virtual source radius R_v for the Emitter #1 was obtained by averaging of 16 measured I-V curves and from the computed linear fit for the high current regime in the Fowler-Nordheim plot, as shown in Figure 4.10. Computation of the virtual source radius R_v for the Emitter #2 was obtained by averaging of 26 to 40 measured I-V curves and from the computed linear fit for the high current regime in the Fowler-Nordheim plot, as shown in Figure 4.11. The reduced brightness for Emitter #2, Gap#2 had unrealistically high value due to the unusually small virtual source radius (0.2 nm) as compared to the other experimental data. Therefore we do not report this data point as real and verified.

Table 4.2: Summary of the figures-of-merit for Emitter #1 which for varying currents levels

Emitter #1 Gap=409µm	Max Emission Current I_{max} (nA)	Emission Current Noise (%)	E-Beam Spread $d\Omega$ (sr)	Reduc. Angular I Density I_r' (nA sr^{-1} V^{-1})	Virtual Source Radius *Rv* (nm)	Reduced Brightness B_r *(Rv)* (A m^{-2} sr^{-1} V^{-1})
Current #1	1974	$3.1^{\dagger}$	0.104	74.0	2.1*	5.5×10^{9}
Current #2	1465	$1.7^{\dagger}$	0.067	81.0	2.1*	6.1×10^{9}
Current #3	909	$9.4^{\dagger}$	0.121	31.4	2.1*	2.3×10^{9}
Current #4	524	$7.2^{\dagger}$	0.154	14.8	2.1*	1.1×10^{9}

(*) – The virtual source radius was computed from the average of 16 measured Fowler-Nordheim curves

(†) – Measured over 1 minute time period

Table 4.3: Summary of the figures-of-merit for Emitter #2 which was tested at varying tip-to-anode distances

Emitter #2 I_{max} = 1 µA	Anode Cathode Gap (µm)	Emission Current Noise (%)	E-Beam Spread $d\Omega$ (sr)	Reduc. Angular I Density I_r' (nA sr^{-1} V^{-1})	Virtual Source Radius *Rv* (nm)	Reduced Brightness B_r *(Rv)* (A m^{-2} sr^{-1} V^{-1})
Gap #1	296	$2.1^{\ddagger}$	0.219	26.7	2.0	2.1×10^{9}
Gap #2	414	$3.1^{\ddagger}$	0.482	11.2	0.2**	7.3×10^{10}
Gap #3	611	$2.5^{\ddagger}$	0.306	15.0	2.2	1.0×10^{9}

(**) – The virtual source radius was unusually small as compared to the other experimental data

(‡) – Measured over 10 minutes time period

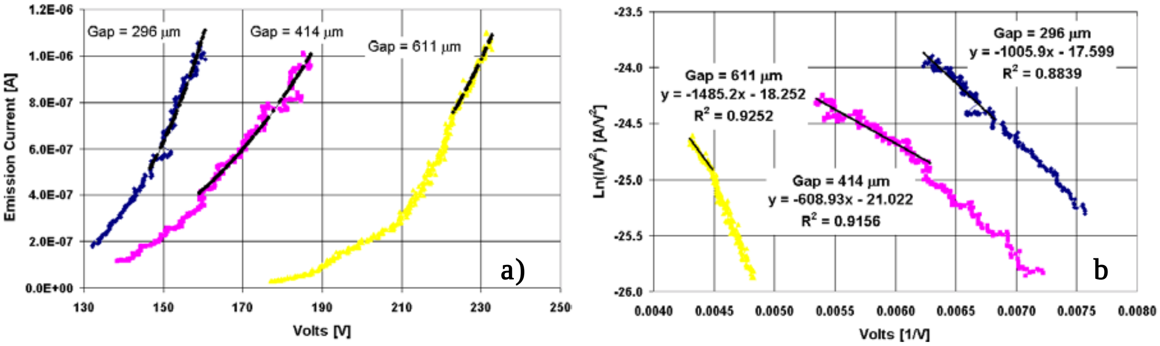

Figure 4.11: Data for Emitter #2 tests, a) average of N measured I-V curves (N = 40 for Gap = 296 µm, N = 26 for Gap = 414 µm, N = 26 for Gap = 611 µm) and the computed fits for the high current regime, b) Fowler-Nordheim plots and the computed linear fits for the high current regime.

The brightness results were comparable to the best brightness results from a nanotip emitter achieved to date. Our results were about 10% better than the best brightness results from a nanotip emitter archived to date as reported by Jonge et al. [4.28, 4.29, 4.30] and Hata et. al [4.31]. A conservative estimate of the reduced brightness can be computed assuming that the radius of the virtual source R_v was equal to the radius R_{CNT} of the carbon nanotube emitter. With this assumption ($R_v = R_{CNT}$), the conservative estimate of the reduced brightness was 1.0×10^9 A m^{-2} sr^{-1} V^{-1} for our best CNT emitter. This conservative estimate establishes that the lower bound of the reduced brightness measured with our CNT field emitters.

Measuring the energy spread of the nanotip emitter was not conducted due to the high cost and the complexity of the experimental setup. Instead we use an average values found in the literature. For carbon nanotube emitters the reported energy spread was 0.2 to 0.3 eV.

The other field emission figures-of-merit measured were CNT emitter noise and lifetime. We observed that the I-V curves of the CNT emitters had very high slope that made them unstable for small changes in the voltage. To provide stability to the system we decided to test each CNT emitter with a ballast resistor R_b added in series to the emitter. The consequence of adding the ballast resistor is that the I-V curves become flattened and the therefore more stable. We tested different values of added R_b between 100 kΩ and 100 MΩ and decided to bias each test with 100 MΩ ballast resistor. The consequence of adding the ballast resistor was that before any I-V analysis we had to correct the I-V curve and remove the effects of the added serial resistance. The values for I were unchanged and the values for the extraction voltage were corrected as:

$$V_{corrected} = V_{measured} - I_{measured} \times R_{100M\Omega}$$

We verified the validity of the above correction by generating an I-V curve for a CNT emitter array with a R_b of 500 kΩ and correcting the I-V curve to show that when it corrected it matches an *I-V* curve generated without use of ballast resistor, as shown in Figure 4.12.

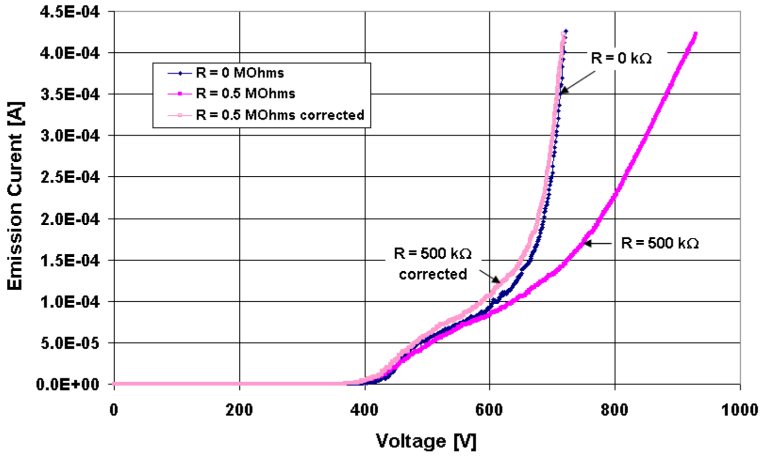

Figure 4.12: Correction of an I-V curve with a 500 kΩ ballast resistor in series with the CNT emitter array to match an I-V curve with 0 kΩ ballast resistor. The CNT emitter array in this example had I_{max} = 420 μA.

The noise and lifetime test were always recorded for all CNT emitters. During this research we tested more than 40 different CNT emitters and analyzed 27 CNT emitters. From the 27 CNT emitters we considered 21 CNT emitters that could reach stable emission. The duration of the tests was from 1 min to 600 min with average test lasting about 235 min. The average noise level of the entire set of 21 CNT emitters was 6.0%. The best CNT emitter that was grown on a Si base had a noise of 50 nA for an average current of 2878 nA, or 1.7% for 10 hour time test (Figure 4.13a). The best CNT emitter that was mounted on W base had a noise of 47 nA for an average current of 956 nA, or 4.9% for 10 hour time test (Figure 4.13b). If we compare the noise level in percentages, then the best CNT emitter on W had a noise 2.3% (66 nA for an average current of 2831 nA) for 300 minute time test. All the tests were conducted in open loop.

In future work we plan to build a feedback controller to better stabilize the emission current, especially emission drift.

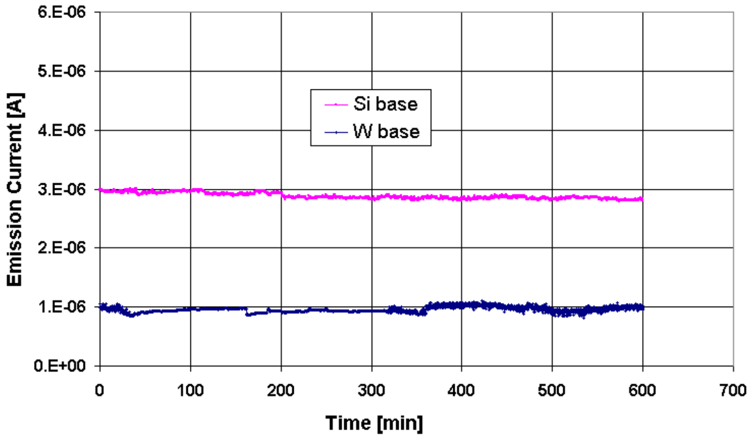

Figure 4.13: 10 hours time test for two CNT emitters: a) CNT grown on Si, I = 3 µm, I_{noise} = 50 nA or 1.7% b) CNT mounted on W, I = 1 µm, I_{noise} = 47 nA or 4.9%

Since we only had one field emission test rig, the duration of the tests was limited to no more than 600 minutes (10 hours) so that we could evaluate a larger number of tips and be able to compare their performance.

4.3.2 Testing of the CNT emitter in an SEM instrument

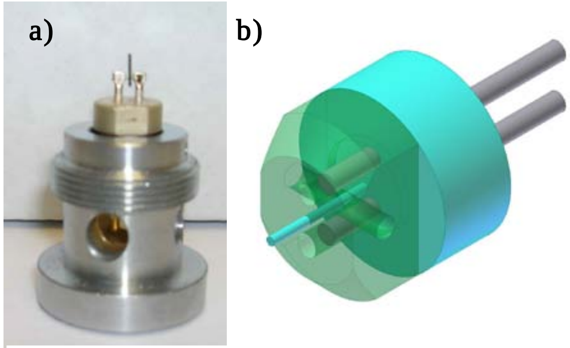

Figure 4.14: SEM filament holder for CNT emitter, a) holder used in initial trials, b) CAD model of the new holder design.

In a first of its kind, we also demonstrated that the CNT emitters can be used with commercial SEM instruments. The first task in evaluating the CNT emitters in a commercial SEM was to build an SEM filament holders on which a CNT emitter can easily be mounted and un-mounted for evaluation purposes. Previously, we obtained a couple of Hitachi type SEM filaments from ScanService Corp. that we used for holder evaluation and re-design. A practical solution was to remove the existing W filament and replace it with a hollow stainless steel tube that was used to insert a 10 to 20 mm long W wire with a CNT emitter on it (Figure 4.14a). Unfortunately, the SS tube was spot welded in place. The spot-welding provided poor control over the tube alignment. We have subsequently designed a SEM filament holder that slips on the existing Hitachi type SEM filament base (Figure 4.14b) but did not get chance to build it. Due to its bulkiness, this design does not allow for controllable heating of the emitter, but can be used for CNT emitter evaluation in a commercial Hitachi SEM tool. In future, we plan to improve the holder design to allow for controllable heating of the CNT emitter that may be needed to remove contaminants before the emitter is evaluated.

Our team and ScanService Corp. evaluated two CNT emitters and briefly operated the SEM to image a sample. It has to be noted that the CNT emitters were severely misaligned at nearly 45° and were not optimal. The SEM testing required that we use our special SEM filament holder and required that we modify a commercial scanning electron microscope (SEM) tool to allow CNT emitter testing. The main SEM modification was the change of the amplifier gains to the extraction voltages of the tool. Due to the lower turn-on voltages CNT emitters need an order of magnitude less extraction voltage for their operation. A special LabView data acquisition system was connected to the SEM to control it emission and to collect data. In future we plan to work on modifying a dedicated SEM in the manner we did on the pre-trials and improve the control of the SEM experiments.

Figure 4.15 shows the I-V curves of the CNT emitters as operated in the SEM and Figure 4.16 shows the time and stability test during brief SEM operation. The initial SEM tests of the CNT emitters showed that CNT emission in a commercial tool is feasible and exposed the problems we need to solve to improve the SEM evaluation. For example, we need a better holder design to allow for heating of the CNT emitter and the CNT emitters need to be nearly aligned to the vertical axis of the W tip.

The instrument figures-of-merit that we need to evaluate in future tests of CNT emitters in SEM instruments are: high imaging resolution, low signal-to-noise ratio, fast imaging speed, stability of the image, long emitter lifetime.

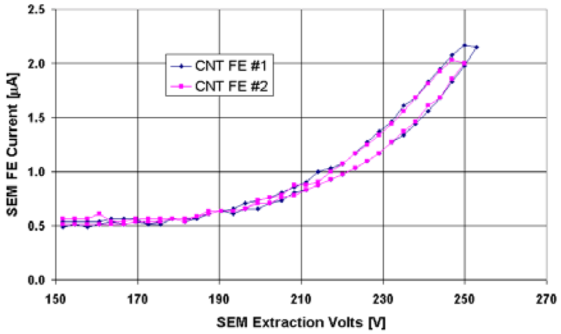

Figure 4.15: I-V curves of 2 CNT emitters as operated in the SEM

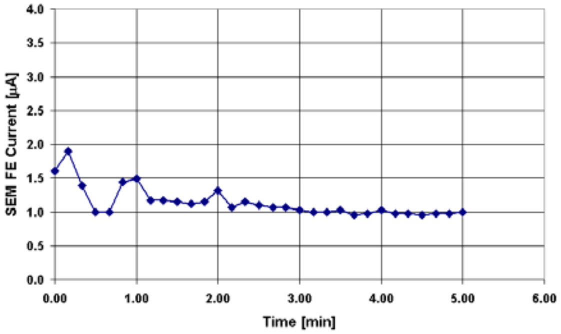

Figure 4.16: Time and stability test of CNT emitter #1 during brief SEM operation. Noise level is 4.4% for the last 2.5 min and 19.4% for the entire range.

4.4 CONCLUSIONS

4.4.1 Emitter Design

We experimentally measured, analyzed, and evaluated figures-of-merit of carbon nanotube field emitters. Evaluation of the CNT emitters revealed that there were differences between CNT emitters depending on the way they were manufactured. To compare the CNT emitters we can take, for example, the average current noise as a basis of comparison. Table 4.4 shows the breakdown of the average current noise per type of CNT emitter in major categories of fabrication. The statistics on the different combinations are not shown. If stability and lifetime of the CNT emitters were taken as a basis of comparison, the performance breakdown as described in Table 4.4 would still match.

Table 4.4: Evaluation of set of 21 CNT emitters

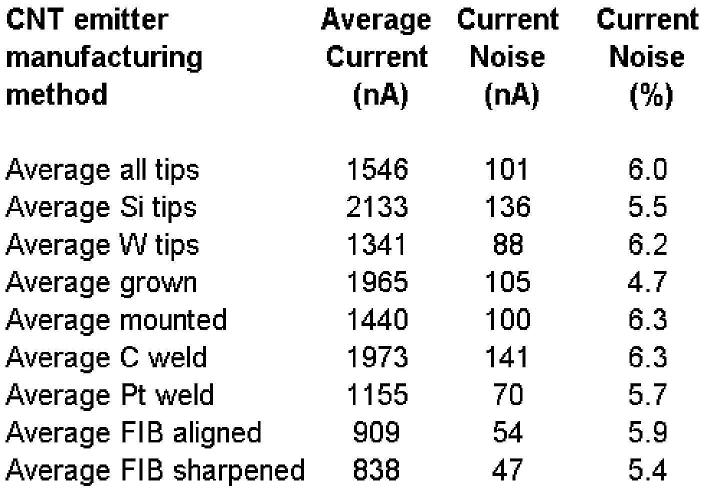

CNT emitter manufacturing method	Average Current (nA)	Current Noise (nA)	Current Noise (%)
Average all tips	1546	101	6.0
Average Si tips	2133	136	5.5
Average W tips	1341	88	6.2
Average grown	1965	105	4.7
Average mounted	1440	100	6.3
Average C weld	1973	141	6.3
Average Pt weld	1155	70	5.7
Average FIB aligned	909	54	5.9
Average FIB sharpened	838	47	5.4

4.4.2 CNT Emitter Fabrication

By testing numerous CNT emitters that we fabricated during this research, we have shown that in average they have suitable high brightness, small size, high stability, and long lifetime. The results and findings are summarized as follows:

i) On average, CNT emitters on Si substrates performed better then CNT emitters on W substrates. These were the main two types of CNT emitters we evaluated. Our explanation is that the contact resistance between the CNT and the W is greater than the contact resistance between the CNT and the Si, and as a result the CNTs on Si were more stable.

ii) Since we did not have CNTs grown on W we compared CNT emitters grown on Si vs. CNT emitters mounted on Si. On average, CNT emitters grown directly on silicon substrates performed better then CNT emitters mounted on Si substrates. Our explanation is that the contact resistance between the CNT and the bare Si is greater than the contact resistance between the CNT and the Si covered with catalyst and CNTs laying on the surface. Confirming this finding is the observation that the mounted CNT emitters were unstable with jumpy emission current. Nevertheless, CNTs on Si, wherever grown or mounted, performed better then CNTs on W.

iii) To improve the contact resistance between the CNT emitter and the W base we started welding the base of the CNT to the W with carbon and Pt depositions. This approach significantly improved the performance of the W based CNT emitters. There was however a difference between using only carbon welds and only Pt welds. CNTs with Pt welds performed better. Our explanation is that oxidation of the W base contributed to poorer electrical contact between the CNT and the W, whereas the Pt deposition protected the W better from oxidation. We concluded that a tungsten based CNT emitter design has to have a process step to protect the contact from oxidation.

iv) The alignment of the CNT emitter did not play a role in the noise and lifetime of the emitter as long as the nanotube was within 45° from the base, which we consider to be a large misalignment. We do not know how misalignment affects the beam spread and the brightness.

v) After we solved the problems with the contact resistance between the CNT and the substrate and addressed the CNT failures at the base of the emitter we started observing CNT emitter failures along their length. In particular, most CNT emitter failures were caused by gradual or sudden shortenings of the nanotube, as shown in Figure 4.17, until it was all removed. The failure was a function of the maximum emission current to which the emitter was exposed. For CNT emitters on W most failures occurred at currents of more than 2 µA and for CNT emitters on Si most failures occurred at currents of more than 4 µA. Our explanation is that defects and contamination along the length of the CNTs started to play role in the CNT emitter failure. It is also possible that the open ends of the CNTs were the contributing failure mechanism.

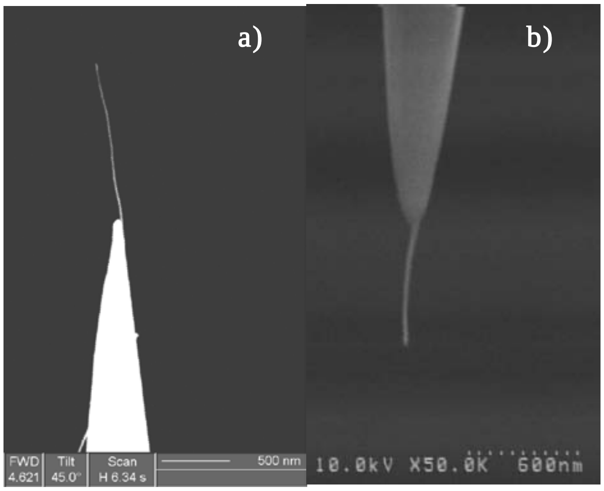

Figure 4.17: a) CNT emitter that was mounted to a W tip and was Pt welded at the base, L ~ 1100 nm, b) the same CNT emitter was shortened after some emission tests, L ~ 400 nm.

4.4.3 Summary

We have demonstrated that once the CNT emitter failure modes are better understood and resolved, such CNT emitters can easily reach reduced brightness on the order of 10^9 A m^{-2} sr^{-1} V^{-1} and noise levels of about 1%. Our analytical models of field emission matched our experimental results well.

We demonstrated reduced brightness B_r of 6.1×10^9 and 2.1×10^9 A m^{-2} sr^{-1} V^{-1}, for two different emitters (Table 4.5). The results are comparable to the best brightness results from a nanotip emitter archived to date, 1.3 to 2.5×10^9 A m^{-2} sr^{-1} V^{-1} as demonstrated by Jonge et al. and 5.6×10^9 A m^{-2} sr^{-1} V^{-1} as demonstrated by Hata et. al. Our CNT emitters have an order of magnitude better reduced brightness than state-of-the-art commercial Schottky emitters (B_r for ZrO/W is 2×10^8 A m^{-2} sr^{-1} V^{-1}).

Table 4.5: Summary of the best two CNT emitters

Best results	Max Emission Current I_{max} (nA)	Emission Current Noise (%)	E-Beam Spread $d\Omega$ (sr)	Reduc. Angul. I Density I_r' (nA sr^{-1} V^{-1})	Virtual Source Radius Rv (nm)	Reduced Brightness $B_r\,(Rv)$ (A m^{-2} sr^{-1} V^{-1})
Emitter #1	1465	1.7†	0.067	81.0	2.1	6.1×10^{9}
Emitter #2	986	2.1‡	0.219	26.7	2.0	2.1×10^{9}

(†) – Measured over 1 minute time period
(‡) – Measured over 10 minutes time period

We also demonstrated CNT emitters with excellent emission stability and low noise of less than 5 % and a tip life of 10 hours without any degradation at all. The best CNT emitter that was grown on Si base had a noise of 50 nA for an average current of 2878 nA, or 1.7% for 10 hour time test. The best CNT emitter that was mounted on W base had a noise of 47 nA for an average current of 956 nA, or 4.9% for 10 hour time test. If we compare the noise level in percentages, then the best CNT emitter on W had a noise 2.3% (66 nA for an average current of 2831 nA) for 300 minutes time test. All the tests were conducted in open loop, without any feedback. With a feedback loop we may be able to reach a noise level of less than 1 %. Using the data from the 10 hour test we predict that emissions lasting 6 months are possible.

Figure 4.18: A camera photo of an SEM screen, demonstrating a proof-of-concept of operating an SEM instrument with a CNT emitter.

We had an opportunity to evaluate our CNT emitters in a modified commercial scanning electron microscope (SEM) tool and briefly operated the SEM to image a sample, as shown in Figure 4.18. Therefore, we demonstrated a proof-of-concept of operating an SEM instrument with a CNT emitter.

4.5 FUTURE RESEARCH

4.5.1 Emitter Energy Spread Measurement

One important parameter in improving the resolution of scanning electron beam instruments is to use an electron source that has low energy spread. Energy spreads lead to chromatic aberration of the electron optical system, reducing the resolution of the instrument. An energy spread of an electron source is defined as the full width at half maximum of the energy spectrum and it is determined by the temperature T and the tunneling parameter d. The tunneling parameter on the other hand is determined by the electrical field from the emitter E and the emitter work function ϕ.

It has been demonstrated that CNT nanotip emitters have much lower energy spread than state-of-the art Schottky emitters and either lower than or the same as W cold field emitters. Bonard et al. [4.3] and de Jonge et al. [4.9] have measured and demonstrated that carbon nanotube emitters have very low energy spread in the ranges of 0.2 to 0.3 eV. Fransen et al. [4.17] have measured energy spreads from carbon nanotubes down to 0.11 eV.

Because the emission current depends on the work-function as $\phi^{3/2} / V$, where V is the applied electric field, lowering of the work-function can have dramatic effects. Morin et al. [4.31] have shown that Cs adsorption on a sharp W tip decreased the work-function from 4.5 eV to 1.6 eV while at the same time the energy spread decreased by a factor of 3.

In future research we plan to experimentally measure the CNT emitter energy spread. At this time, we plan to also explore new ways to lower the energy spread of the nanotips by lowering the work-function of our tip [4.31, 4.32]. One way to achieve this goal is to coat the nanotips with a low work-function material such as Cs, ZrC, HfC, or the like. The width of the energy spread should also scale down with the work function.

4.5.2 Virtual Source Measurements

In the future we also plan to improve the resolution of the measured radius of the virtual source. One approach will be to use a Field Ion Microscope (FIM) to get a clean field emission pattern magnified enough to observe the emission from the individual atoms. Optionally, one can build a point projection microscope to measure the virtual source of the CNT emitters. The point projection microscope can be build in accordance with the descriptions of de Jonge [4.8]. In this technique the emitter is positioned with a help of a XYZ nanomanipulator above a sharp edge inside a FIM. The presence of the sharp edge on front of the ion flow produces diffraction pattern representative of the emission source, thus enabling the measurement of the virtual source.

Chapter 5: Lateral Carbon Nanotube Field Emitters

5.1 INTRODUCTION

The need of modern vacuum electronic devices requiring high current densities and high total current, and fast and simple operation without the use of an external energy source (such as a heater, or intense light source), has motivated the pursuit of a new field emission current sources. This requirement eliminates the use of hot thermionic cathodes which have slow response and require an external heating source.

There has been significant effort to build microwave vacuum electron devices using cold cathodes to replace the existing hot thermionic cathodes. The most common approach has been the use of Spindt type field emission array (FEA) cathodes [5.21]. However this approach has failed to produce practical, useful devices to date.

Field emission arrays based on cold cathode carbon nanotubes have caught the attention of the research community as an attractive solution for achieving practical vacuum electron devices, such as microwave vacuum amplifiers and X-ray sources. Milne et al. [5.1] provides a comprehensive chart of the competing vertically aligned carbon nanotube technologies.

Today's field emitters can achieve more than 10 µA of current from a single emitter tip. In addition, such field emitters can be packaged into arrays with anywhere from 1 million to 100 million tips/cm^2. Thus far, however, emission non-uniformity has prevented such field emission arrays from achieving large total currents (> 1 A). Field emission currents of 1 A and greater and current densities of 10 A/cm^2 and greater can enable a new generation of microwave devices suitable for radar and communications, high power microwave devices for directed energy applications, medical x-ray sources, ionization/neutralization sources for spacecraft propulsion, and flat-panel field emission displays.

The goal of this research was to demonstrate a novel emitter device in order to reduce the variation in the current from emitter to emitter, thereby allowing high current density operation with high total current.

CNTs have been identified as ideal field emission sources because of their nanometer-scale dimensions, high aspect ratio, chemical inertness, excellent electrical properties, and mechanical strength. CNTs are far more resistant to sputtering from ionized residual gas molecules than conventional field emission cathodes composed of refractory metals, and they are inert with respect to many residual gasses. Previous research has also shown that CNTs in any form factor (individual, bundles, film, forest) have field emission properties that are better then their sharp metal emitter counterparts.

Prior research has shown that individual, vertically aligned CNTs, as opposed to CNT bundles and films, exhibit low turn-on voltage (1 V/µm), high emission current (0.2 mA), and corresponding high emission current density (4×10^8 A/cm^2). However, as a result of electrostatic screening effects, the high emission currents from an individual emitter may not translate directly to an equivalent emission current from a large sample containing many such emitters. This is true whether the emitter is CNT based or metal based. This is also true for any array elements comprising individual, bundle, or film form-factors. Previous research has shown that an optimal CNT based field emission array is one where the emitter-to-emitter distance is balanced with respect to its length. Therefore, for achieving large emission currents with a field emission array, it is desirable to fabricate an array consisting of strategically distributed nanotube elements, with elimination/reduction of the screening effect in mind.

Previous research has shown that, as a result of any length non-uniformities among vertically aligned CNTs in the array, it is expected that the emission from the field emitter array may also be non-uniform, leading to hot-spots and possible overheating and self destruction.

5.1.1 Related Work

There has been an unprecedented amount of work in the area of carbon nanotubes over the past decade. Among all the amazing properties of CNTs, their field emission characteristics have been extensively studied and analyzed. We will briefly overview some the research work in the field of CNT based high emission current sources and describe our advantages over these approaches.

Bonard et al. [5.2] have reported the highest current density to date from an individual manually mounted CNT, 4×10^{8} A/cm^2. Chen et al. [5.3] have reported the highest current density from an array to date. They claim a stable field emission current density of more than 6 A/cm^2 for an electric field of 7.7 V/µm and a total current of > 1.2 mA. Their result was achieved with a bundle of CNTs packed in a 70 µm diameter and patterned as 4 dots spaced 2 mm apart. The apparent record for the highest current density from an array appears to have been set by Bower et al. [5.4]. Bower et al. have reported a current density of 16 A/cm^2 from an array of 9 patterns of a CNT forest, each with dimensions of 10×10 µm. However, they normalize the current density by the emission area of the nanotubes and not the total area of the array. Their total current was 150 µA or 16 µA per CNT bundle. Manohara et al. [5.5] have reported field emission current density of more than 6 A/cm^2 for an electric field of 20 V/µm and 1.8 A/cm^2 for an electric field of 4 V/µm from a 100 µm diameter area separated in patterns of CNT bundles with 2 µm bundle and 5 µm spacing. The CNTs were grown using thermal CVD and with sample patterning. The authors have investigated the optimal emitter bundle size and spacing for maximum field emission. Their approach is to break up the CNT bundle into smaller bundle patterns and then optimize their spacing. Their findings about emitter (bundle) size and spacing do not match the one conducted by Nilsson et al. [5.6] and Suh et al. [7], indicating that the array spacing design highly depends on the type of CNTs (bundles, film, forest) and the packing density. Nilsson et al. [5.6] have shown through simulations and experiments that the optimum nanotube packing density occurs when the inter nanotube spacing is twice the nanotube height. Suh et al. [5.7] have shown that the optimal nanotube spacing is equal to the nanotube height. Nilsson et al. have shown that the uniformity of the field emission from patterned films (forests) of CNTs was the best when the nanotube packing was with medium density. Their poor high-density CNT film performance was explained by the electrostatic screening effects, and the poor performance of their low density CNT film was explained by the non-aligned morphology of the individual CNTs. A simulation by Nilsson et al. showed that for aligned CNT emitters with 1 μm height the ideal density is 2.5×10^7 emitters/cm^2. Milne et al. [5.1] has reported high current densities of about 1 A/cm^2 and 1.5 GHz signal modulation capability from a CNT cold cathode. Their optimized CNT array was constructed from individual CNT emitters, grown via PE CVD, with CNT heights of 5 μm, CNT diameter of 50 nm, emitter spacing of 10 μm, and a total emission area of 500×500 μm. The advantage of their array is that the emitter is a single CNT with only 4% deviation in diameter and 6% deviation in height across all CNTs in the array. The disadvantage is the large size of the CNT and probably their more amorphous then crystalline morphology, typical for plasma assisted CNT growth.

There are a pair of research works related to field emission from the CNT sidewall. Chai et al. [5.8] have demonstrated a field emission from the sidewall of a bent individual multiwall CNT loop mounted atop a metal wire. They operated the emitters in a very low current range, 1-100 nA and briefly demonstrated 5 μA, and mainly investigated the turn-on voltages. Their findings were that CNT loops have smaller turn-on voltages and higher enhancement factors β than CNT tips. Konishi et al. [5.9] have also demonstrated a field emission from the sidewall of a bent individual multiwall carbon nanotube mounted atop a W wire. Their finding is contradictory to the one of Chai et al. Konishi et al. who have reported that CNT loops have larger turn-on voltages than strait CNTs. Konishi et al. also reports sidewall emission that is 2.8 times larger than that of the emission from the tip of a CNT but they do not report the emission current. Jung et al. [5.10] have reported field emission from horizontal CNT film grown in cracks of a substrate and reported a current density of 77 mA/cm^2 but their CNT quality is poor and the CNTs are too dense. Chen et al. [5.11] have reported that highly packed CNT lying horizontally on the surface have smaller turn-on voltage then nanotubes vertically oriented on the substrate.

In this work we present a solution for the non-uniformity of emission problem with a novel lateral CNT emitter design that incorporates horizontally aligned CNTs suspended on silicon posts wherein the electron emission occurs from the sidewall of the carbon nanotube as opposed to the end of the nanotube as is commonly done. The main advantage of emission from horizontal nanotubes is that the entire carbon nanotube network lies in the same plane, without any protrusions, therefore eliminating non-uniformities among the nanotube emitters. Our approach to designing an optimal CNT array is to fabricate the CNTs suspended on an array of conical or cylindrical silicon posts, where the spacing of the posts, the lengths of the CNTs, and the nanotube-to-nanotube emitter spacing are all controlled. The preferred lateral CNT emitter element design incorporates single horizontally aligned carbon nanotube, which is nanometers in diameter, suspended on two microns-tall silicon posts spaced microns apart. An array of lateral CNT emitter elements would incorporate many such elements spaced microns apart, as illustrated in Figure 5.1. Although horizontally suspended CNTs have been manufactured in the past and have been used for many applications (mainly sensors, resonators, and prototype transistors) we have not encountered other research which has investigated their use as field emitters. We report here an observation of field emission from a lateral CNT emitter element.

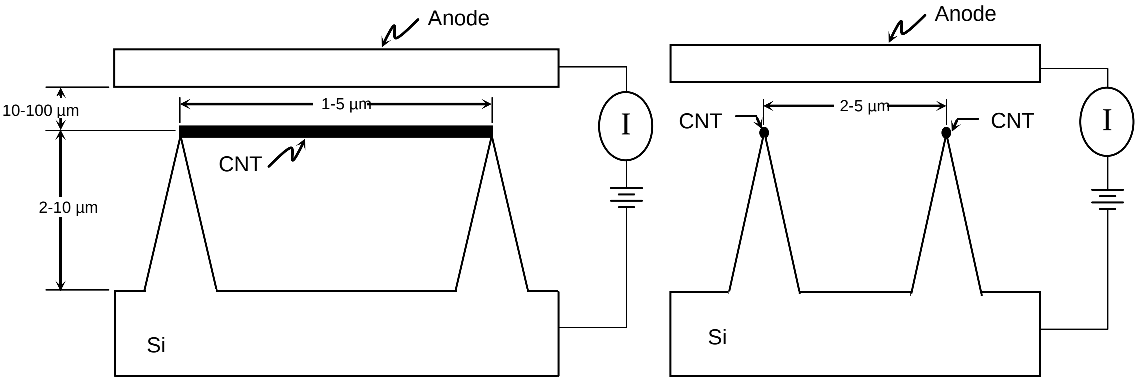

Figure 5.1: Schematic drawing of lateral CNT emitter design and ranges of the key dimensions.

5.2 EXPERIMENTAL RESULTS

5.2.1 CNT Lateral Emitter Substrate Fabrication

Fabrication of the substrate for the lateral field emitter is the first task that needs to be resolved before fabricating the emitter device. The preferred substrate for our design is a pair of high aspect ratio posts that serve as a template from which the suspended CNT emitters are fabricated. Besides acting as a fabrication template, the presence of high aspect ratio posts will help elevate the CNT emitters from the surface, effectively reducing the electrostatic screening effect with respect to the surface. We anticipate that posts with heights between 2 to 10 µm are sufficient to significantly reduce the screening effect.

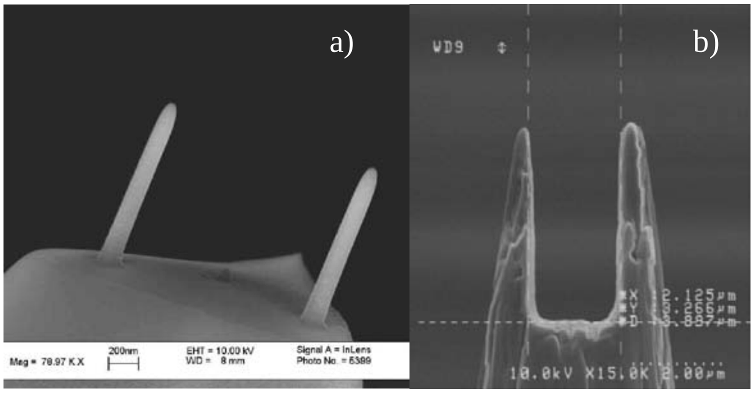

Figure 5.2: (a) Pt pillars on the apex of a sharp Si tip, fabricated using e-beam induced deposition technique. (b) Ion-milled W to produce knife-edge pillars for growing or mounting CNT emitters.

The simplest substrate for the simplest lateral-emission element with a single suspended carbon nanotube is high aspect ratio Pt or W pillars that can be fabricated using e-beam induced deposition (EBID), as shown in Figure 5.2a, or W or Si knife-edges that can be ion-milled from a sharp W or Si tip, as shown in Figure 5.2b. For this work we used dual-beam FIB tool capable of Pt and W deposition and ion-milling. The ion-milling is less precise and produces knife-edge pillars as opposed to the more precise deposited pillars which can have diameters between 35-100 nm, lengths between 1-5 µm, and spacing between 1-10 µm. This technique is also suitable for fabricating an emitter array with Pt/W/Si pillars with different heights and separation, but practically limited to an array of no more than 2×2 or 3×3 pillars. Emitter arrays requiring more than 9 pillars need to be done using silicon micro-fabrication technology.

5.2.2 Manual CNT Lateral Emitter Fabrication

The simplest lateral-emission element with a single suspended carbon nanotube was fabricated manually as shown in Figure 5.3. A dual-beam FIB/SEM tool equipped with nanomanipulator was used to manually suspend an individual carbon nanotube over two posts. In this procedure the free end of a cantilevered CNT (from a sample rich with

CNTs) was first contacted to a sharp W probe. Using Van der Waals forces the CNT was pulled from its source substrate. Alternatively, the CNT can be cut free from the source substrate by applying a current pulse. Detailed procedure on making CNT tips is described in Appendix A (see also reference [5.12]). The new free end of the CNT tip was then positioned to one of the pillars were it was electrically connected to the first post using electron assisted deposition (EBID) technique [5.13] of Pt. The second end (connected to the W tip) was then brought in contact to the second post, where the EBID procedure was repeated. This CNT emitter had length of 1804 nm and diameter of 18.2 nm. Figure 5.3 shows a micrograph of the CNT lateral emitter after it was utilized in extensive field emission tests ranging up to 5 μA of current, showing no signs of degradation or contamination.

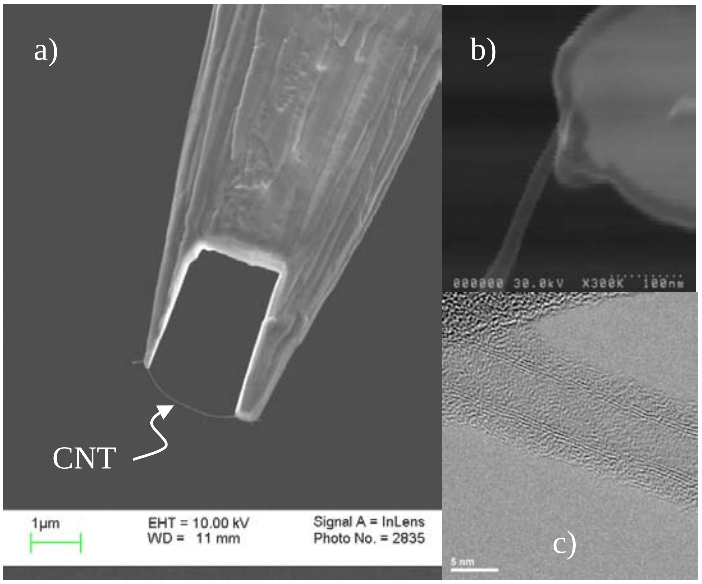

Figure 5.3: (a) Manually attached CNT emitter on an ion-milled W tip. (b) The CNT was welded with W using e-beam deposition. Close-up view of the attachment between the CNT and the W edge. (c) TEM image of typical CNT as the one attached in (a).

5.2.3 CNT Lateral Emitter Fabrication with Direct CNT Growth

Alternatively we fabricated a lateral CNT emitter by directly growing the CNT on the ion-milled Si posts. In this procedure the Si posts were ion-milled on top of a standard scanning probe microscopy (SPM) tip. The SPM tip with ion-milled posts was first cleaned with clean and dry compressed nitrogen to remove any large contaminants. Subsequently, the tip was carefully dipped into solutions containing catalytic material. The SPM tips were then placed in a CVD oven in such manner that the flow of the carrier and precursor gas during the CVD process is perpendicular to the posts. The CNT emitter was grown using thermal CVD process. Typical CVD recipes were conducted with a flow rate of Ar/H_2 1000-2000 sccm to 1 sccm of ethylene at growth temperature of 750°C for 1 min. The CVD process produces horizontally suspended CNTs from sharp knife-edge Si posts, as shown in Figure 5.4. Due to the larger width of the knife-edge Si posts there were more than one CNT spanning the gap (Figure 5.4a and 5.4b) but we have shown that a single CNT can also be grown (Figure 5.4c). We believe that the yield of making single CNT emitters will improve once we reduce the size of the posts. The process for growing horizontal CNTs is repeatable and shows promises that will work on large array of posts.

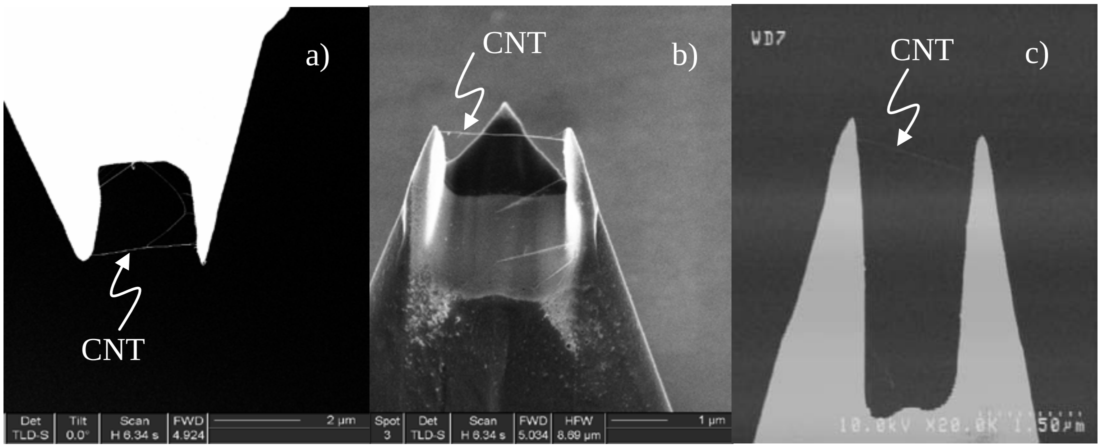

Figure 5.4: Examples of three lateral-emission CNT emitters. The Si substrate was ion-milled to fabricate a gap. The CNTs were grown directly using CVD process. Few extra CNTs in the gap were removed for sample (a) and (b). Sample (c) grew only a single CNT.

5.2.4 Evaluation of the CNT Lateral Emitter

We report a successful emission from a lateral CNT emitter element having a single suspended CNT. We report a field emission from the manually made lateral field emitter from Figure 5.3, the grown lateral field emitters from Figure 5.4 and several other grown emitters. There was no significant difference in performance based on the way the CNT emitter was fabricated.

The tests were conducted in a custom vacuum chamber, equipped with a view-port suitable for taking images of the field emission. The average vacuum level for the tests was ~ 1×10^{-6} Torr. We had two types of sample holders, one for CNT emitters fabricated on a SPM tip substrate and another for CNT emitters fabricated on a sharpened tungsten wire. The former sample holder is made of two parallel glass plates coated with gold or aluminum. The CNT emitter is fixed to the cathode plate with a carbon paste where the anode plate is positioned above the emitter. The spacing is controlled with precision machined Macor and quartz spacers. The latter sample holder is made of a wire holder with a set screw and a metal coated glass plate perpendicular to the wire. The anode-cathode spacing is controlled by setting the gap under an optical microscope. For diode type field emission measurements the electrical field is supplied with Keithley 237 current-voltage source that can provide up to 1100 V of bias. The I-V tests were run with an automated system consisting of LabView based software and National Instruments hardware.

The independent parameters we can measure are: the emission current I, the applied extraction voltage V, the size of the field emission pattern, and the radius of the CNT emitter R_{CNT}. We also had to measure the tip-to-anode distance d, and we had to assume the work-function for a carbon nanotube ϕ. From these parameters we computed: the solid angle of the electron beam spread $d\Omega$, the angular current density I', the reduced angular current density I_r', the field enhancement factor β, the virtual source area S_v, and the reduced brightness B_r. The spread of the emission pattern was measured by placing a transparent glass coated with ITO and phosphorus as the anode. The result of the measurement was a bright spot or spots on the screen as a result of the electron bombardments. From the radius of the bright spot and the source to screen distance we can compute the solid angle of the electron beam spread $d\Omega$ (steradians). The ratio between the emission current I (A) and the beam spread solid-angle $d\Omega$ (sr) will give us the required angular current density I' (A sr^{-1}).

The virtual source of an electron emitter is the area $S = \pi\, r_V^2$ from which the electrons appear to originate from when they are traced back along their trajectories. For nanotips with small radius, a conservative estimate of the radius of the virtual source r_V (m) can be assumed to be the radius of the nanotip, $r_V = R_{NT}$. For our carbon-nanotube emitters this approximation holds well because the typical diameter of our carbon-nanotube nanotips is 10 nm and less.

Table 5.1 lists the summary of the most relevant figures-of-merit for field emitters and compares the performances between the vertical field emitter to the manually fabricated lateral field emitter. The results show that field emission from a lateral CNT emitter element is comparable to emission from the end of a vertical carbon nanotube. As expected, because of their larger cross section (18 nm x 1800 nm), the lateral emitters have smaller current density J, and larger electron beam spread $d\Omega$. Therefore the resulting reduced angular current density I_r’ and the reduced brightness B_r are smaller for a lateral field emitter. However, the lateral emitter could reach higher maximum emission current then the vertical emitters.

Table 5.1: Comparison between a vertical field emitter and a lateral field emitter.

Emission Comparison	Max Emission Current I_{max} nA	Emission Current Noise %	E-Beam Spread $d\Omega$ sr	Reduced Angular Current Density I_r’ nA sr^{-1} V^{-1}	Current Density J A cm^{-2}	Reduced Brightness B_r (Rv) A m^{-2} sr^{-1} V^{-1}
Vertical Tip	1218	5.4	0.112	50.3	1.6×10^{6}	2.7×10^{9}
Lateral Tip	3893	4.5	0.810	11.9	2.4×10^{4}	1.2×10^{8}

We know that an emission pattern from a lateral emitter is round as expected for a nanotube end. However, from the analyses of Figure 5.5 it can be noticed that the emission pattern from a lateral emitter is slightly oval but not quite elongated as we have expected for a ~18×1800mn nanotube emitter.

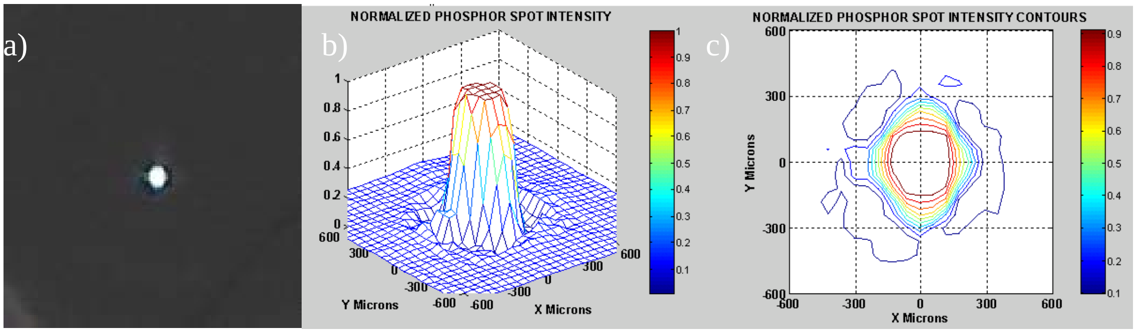

Figure 5.5: a) The image of the field emission pattern from a lateral emitter, digitally recorded with a camera, where its radius was determined with intensity analysis (in this example the semi-axes of the spot were 193 µm for X and 254 µm for Y for a gap of 596 µm), b) normalized intensity plot, c) normalized contour plot.

We also measured the noise and stability of the field emission over time of 30 min to up to 720 min. We tested the grown-CNT lateral field emitter for 12 hour at 8.6 µA, as shown in Figure 5.6b, without any CNT failure. The maximum emission current we could demonstrate was actually limited by the maximum voltage possible with the power supply and the tip-anode gap we have selected. The emission noises were compatible to the vertically aligned CNT emitters, as shown in Figure 5.6a, but the lateral CNT emitter could be used at almost double the maximum current then the vertical CNT emitter.

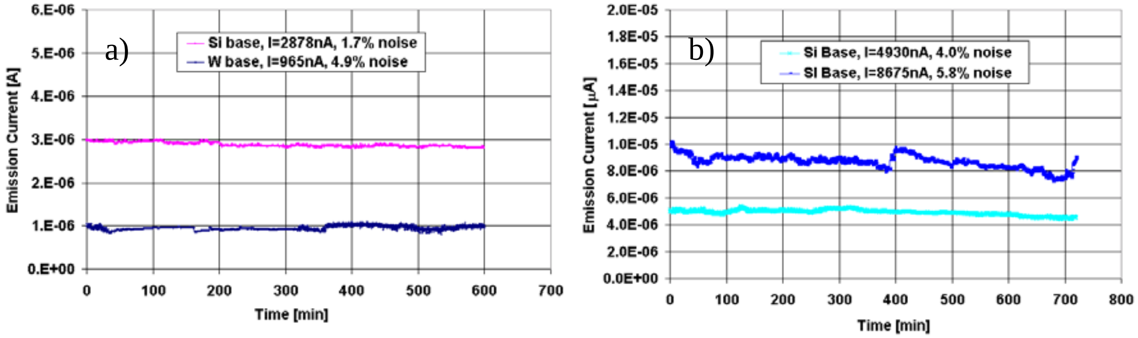

Figure 5.6: Long time stability and noise test for (a) Si and W based vertical CNT emitters and (b) Si based lateral field emitter.

5.3 LATERAL ARRAYS

Since we have demonstrated the operation of a single element of a lateral CNT emitter, we next plan to demonstrate the feasibility of a lateral-emission CNT device having multiple carbon nanotube elements arranged in an array.

To demonstrate the feasibility of a large array of lateral CNT emitters with density of 10^6-10^7 nanotubes/cm^2 where most nanotubes are suspended horizontally on tall Si posts we need to fabricate an array of silicon posts with 3 µm post spacing and active area of 2×2 mm where the post density would be 10^7 tips/cm^2. Assuming that each horizontally aligned CNT emitters produces emission current of 5 µA when screening effects of the neighboring CNT element are accounted for, then the array current density could be computed as follows. For a sample with tip density of 10^7 emitters/cm^2 (3 µm tip spacing) we would get a current density of 56 A/cm^2 for a 100% yield in field emitter fabrication and 28 A/cm^2 for a 50% yield in field emitter fabrication. Realistically we can expect 50%-80% yield in field emitter fabrication. For a field emitter array area of 2 mm on a side the total field emission current would be 1 A per field emitter array device. This level of current density would be very useful for many applications including an X-ray source and a source for microwave vacuum electronics. Depending on the fabrication yield, the screening effects, and the emission current per single emitter, we can compromise by decreasing the emitter spacing thus increasing the emitter density, at the expense of an unwanted increase in the screening effect that would lead to a reduction of the emission current.

5.3.1 Scaleable Fabrication of Lateral CNT Emitters

We report a CNT growth process that produces laterally suspended CNTs from an array of sharp silicon posts (Figure 5.7). We used a commercially available silicon grating sample typically used for calibrating scanning probe tools, such as AFMs. The TGT1 sample has 2×2 mm^2 active area with an ordered array of about 444,000 pyramidal tips with 10 nm end radius, 0.5 µm height, 3 µm tip spacing (~2 µm diagonal tip spacing), and tip density of 10^7 tips/cm^2.

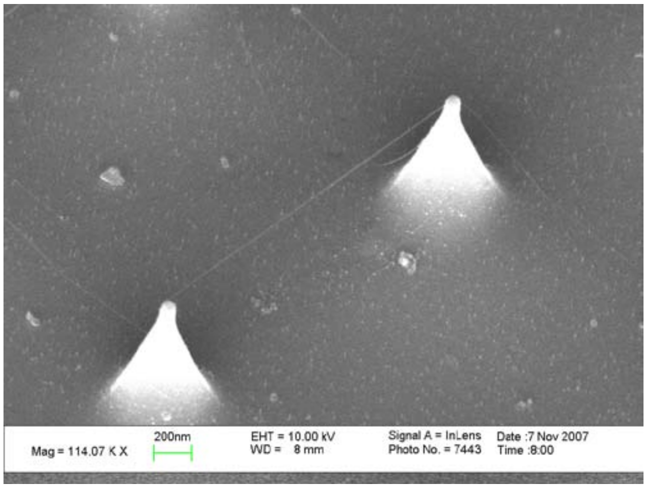

Figure 5.7: Lateral CNTs grown directly with a thermal CVD process on Si posts. The CNT had 10 nm diameter and the same length as the post spacing, ~2 µm.

The substrate, and the Si tips, were coated with catalyst by dipping the sample into solutions containing catalytic material. The array of Si tips was then placed in a CVD oven in such manner that the flow of the carrier and precursor gas during the CVD process is perpendicular to the posts. The CNT emitter was grown using thermal CVD process. At the time of this experiment we did not have a thermal evaporator available. The preferred methods of catalyst deposition includes thermal evaporation and sputtering, which can deposit thin metal films with angstroms precision over the size of a wafer.

The lateral CNT growth process was standard thermal CVD process that is known to produce high quality carbon nanotubes. A mixture of ethylene (C_2H_4) and hydrogen (H_2) are used as the precursor gasses and argon (Ar) or nitrogen (N_2) is used as the carrier gas. Typical CVD temperature is 750ºC for 10 minutes. During the growth process the CNTs nucleate from the catalytic particle on the Si tip and span across the substrate to reach another catalytic particle in its vicinity. In our experience one key parameter to adjust in this process is the total gas flow rate as function of the post spacing.

We have fabricated some number of CNTs that were spanning from one tip to another. Some fraction of carbon nanotubes grew from tip to tip. We believe that our results would have been even better if the tips had been sharper and if the catalyst were to be deposited only on the apexes. SEM images revealed that the array tips were significantly blunter (100-200 nm diameter) then the expected 10 nm radius. However, these results show a process that is feasible to produce an array with laterally aligned and suspended CNTs. We also show small arrays (2×2 and 3×3) of suspended CNT, as shown in Figure 5.8. The instances where we have multiple CNTs suspended between two posts is small. From the initial array of 87 posts we estimate that 70% of the Si posts have a CNT starting or terminating there, about 40% of the CNTs bridge from post to post (anywhere on the post), even smaller percentage of CNTs are suspended from the tips of both posts. The growth of CNTs that do not contact any post is minimal.

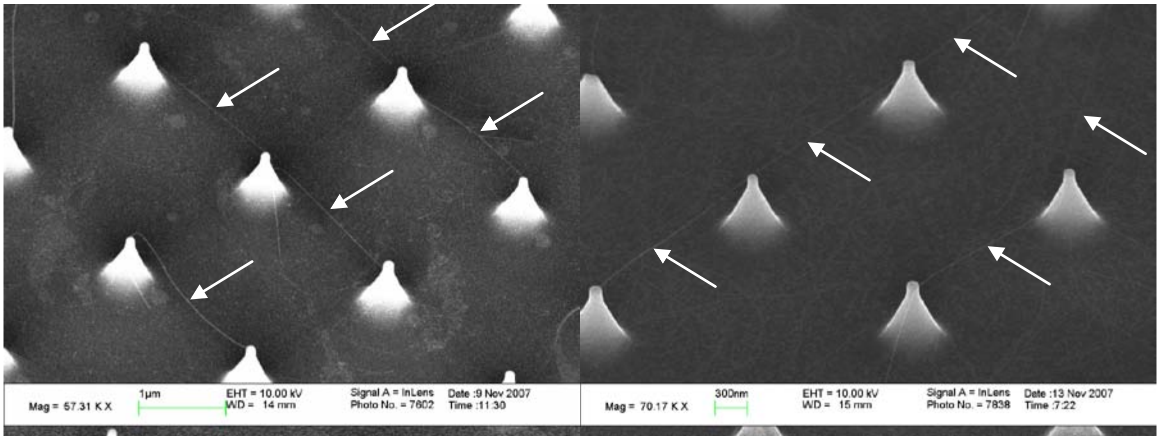

Figure 5.8: Lateral CNTs grown directly on an array of sharp Si posts, suspended from the tops of the Si posts. The white arrows were added to point to the suspended CNTs.

Our yield statistics were not as good as Yang et al. [5.14] but we have more directionality than that study. Yang et al. have demonstrated growth of suspended CNTs from Si nanocrystals that are about 90 nm high and 100–150 nm wide, with 200 nm base-to-base spacing. Among 177 nanotubes 87% are attached to at least two Si islands but the CNTs were connected to the pillars in a disorderly manner.

The suspended SWCNTs produced by Jung et al. [5.15] cover most of the sample and grow from post top to post top but the directionality of the CNTs was not as great. Also, multiple CNTs grew from the posts. The described posts are cylindrical (200 nm diameter) and are not flat but have a large radius of curvature. The post height was 300 nm and the pitch of the array was 250 nm. They also use a methane based CVD process. Jung et al. have demonstrated that use of ion-beam can straighten suspended CNTs and thus improve the yield and the quality of the suspended CNT network.

Cassell et al. [5.16] and Franklin et al. [5.17] have reported controlled growth of suspended single wall carbon nanotubes (SWCNTs) grown on flat-top towers with catalyst printed on top of the silicon towers. The height of the Si towers was ~10 µm with pitch of about 10 µm and diameter of ~2 µm. Their network of CNT growth spans on the top of the towers. They also observed that most CNTs were grown either in the direction of the flow or perpendicular to it. Franklin et al. show a great yield of suspended CNTs but only for a small array of 9 pillars. These results show modest control of the directionality of growing lateral CNTs. The growth temperature is at 900°C and the growth gas is methane.

Peng et al. [5.18] have investigated the spacing of patterned stripes on the density of suspended CNT. The finding was that for spacing of 300 nm the carbon nanotube density was the largest and for gaps of 3 µm the CNT was sparse but more aligned. They also have demonstrated the use of electrical fields to direct the CNT orientation. They also use methane based CVD process.

Jeong et al. [5.19, 5.20] also produced suspended SWCNTs from two-dimensional pillar-structured Si substrates (height 360 nm; pitch 500-800 nm). Thermal CVD with methane was used. Suspending yield was more than 90% but the CNTs were disorderly connecting to the pillars. They achieved an average tube diameter of 1.17±0.27 nm as established by Raman measurements.

Based on our initial research findings and prior literature we have concluded that the main challenges of scaleable and controllable nanomanufacturing of lateral CNTs are: (a) the need to increase the yield of growing individual CNTs that are suspended from the tops of at least two posts and (b) the need to establish control over the directionality and orientation of the lateral CNT.

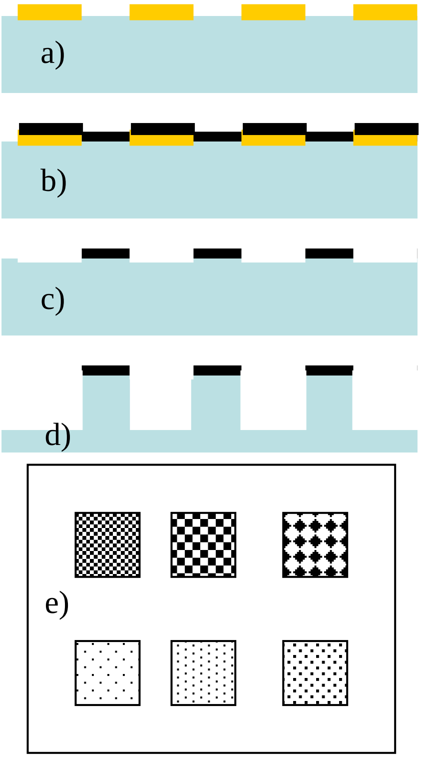

Figure 5.9: Example of micro-fabrication of an array of Si posts

For this large-scale emitter fabrication we plan to demonstrate the use of micro-fabrication technology to build the patterned substrate. The micro-fabricated substrate will provide the best control over the silicon post spacing, height, and cross-section size. The Si post arrays for the CNT emitters can be fabricated using a typical lift-off procedure using iron or nickel CNT catalyst as an etch mask. Figure 5.9 illustrates the process flow for the post array which will be lithographically patterned using both electron beam (for <500 nm diameter posts) and optical lithography (>500 nm diameter posts). From Figure 5.9a, initially an electron or photon beam resist will be spun onto the silicon substrate, exposed and developed which will yield an array of circles on the silicon wafer. A matrix of various size posts (50 nm–1 µm) and various pitches (1-10 µm) will be run simultaneously to determine the optimum array dimensions. After the resist processing, thin iron or nickel catalysts will be evaporated onto the substrates (Figure 5.9b) and subsequently “lifted off” which will result in an array of circular catalyst dots (Figure 5.9c). Subsequent to the lift off process, the catalyst arrays will be reactively ion etched using either a Bosch or cryo deep silicon etch process to produce the silicon posts (Figure 5.9d). Figure 5.9e schematically illustrates a top down view of 6 different post arrays.

Chapter 6: Site Selective Carbon Nanotube Editing

6.1 INTRODUCTION

The ability to edit materials at the nanoscale level is critical for the ongoing nanotechnology revolution. While standard and emerging lithographic techniques will continue to play a critical role in nano-fabrication processes, nano-fabrication also requires site-selective materials editing techniques. As geometries shrink and wafer cost-of-ownership increases, nanoscale re-manufacturing and repair techniques will be increasingly more important. Current techniques to selectively deposit or etch micro and nano size features utilize ion beam deposition and etching, laser ablative etching using far field and near field optics, and mechanical abrasion using a fine microtip. Of these techniques, selective focused ion beam (FIB) processing is probably the most mature technology that has been extended into the nanoscale. While suitable for many applications, focused ion beam processing has several drawbacks that make it difficult to extend to many nanoscale applications. The most severe drawback when using a gallium focused ion beam is gallium implantation into the substrate or material, which can deleteriously change the properties (optical, electrical, mechanical, and biological) of the material [6.1]. Additionally, charging inherent to the ion-solid interaction causes proximity effects and can also lead to so-called "riverbed effects" which erode nearby features when the heavy ion beam is scattered and induces sputtering. Consequently, while focused ion beam processing is a very effective technique in many nanoscale applications [6.2-6.8], an alternative damage-free site-selective nanomaterials editing technique is needed for the fabrication and repair of emerging carbon nanotube (CNT) applications.

Some of the applications that motivated this work include: assistance with the fabrication and repair of carbon nanotube based scanning probe microscope tips and carbon nanotube based electron emitters. This fundamental research will also enable the development of other carbon nanotube based devices.

6.1.1 Motivation for Carbon Nanotube Editing

We have identified several practical applications where carbon nanotubes (CNTs) cannot be fabricated nor edited with conventional process (ion milling, e-beam lithography, etc.) and where the electron-beam-induced editing is the only process available for repairing or modifying the devices: fabrication and repair of carbon nanotube based scanning probe microscope tips and carbon nanotube based electron emitters.

The carbon nanotubes devices (tip and emitters) made by the author are fabricated using a thermal CVD (Chemical Vapor Deposition) process that can produce high quality carbon nanotubes with diameters between 3 nm to 20 nm and microns in length. However, in many cases during the fabrication of CNT tips and emitters there are individual and few CNT samples on or near the apex of a sharp Si tip that make them not as useful. Figure 6.1 shows examples of manufacturing situations where there is a need to repair a CNT tip to make it useful. In Figure 6.1a a single cantilevered CNT needs to be removed without destroying or contaminating the nearby CNT tip. In Figure 6.1b a curved CNT need to be cut under the bend to result in shorter but strait CNT tip. In Figure 6.1c long CNT needs to be cut just before it starts to curve and furthermore the sides of the tip need to be cleaned to remove excess carbon nanotube growth.

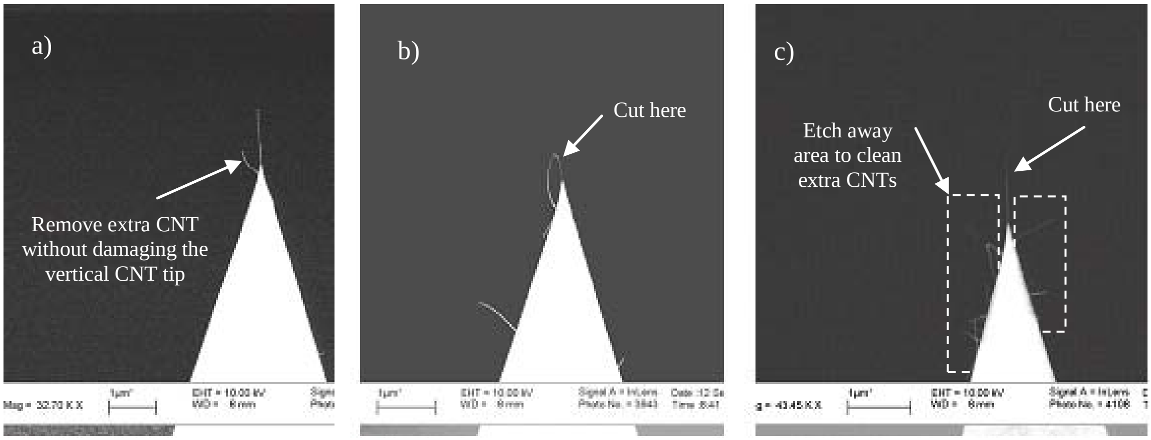

Figure 6.1: Manufacturing situations where repair is needed to make a useful CNT AFM tip

Although the above examples show one particular application, CNT SPM tips and CNT emitters, we are not limited to this application only. For example, we have also developed a network of horizontally aligned CNTs suspended on sharp conical posts as shown in Figure 6.2a. The CNT editing method could be used to eliminate unwanted or fallen down CNTs. Figure 6.2b represents a network of suspended single-walled CNTs (SWCNTs) published by Franklin et al. [6.10]. We could envision that such devices could have excess CNTs removed in the boxed area to produce a better network of interconnects.

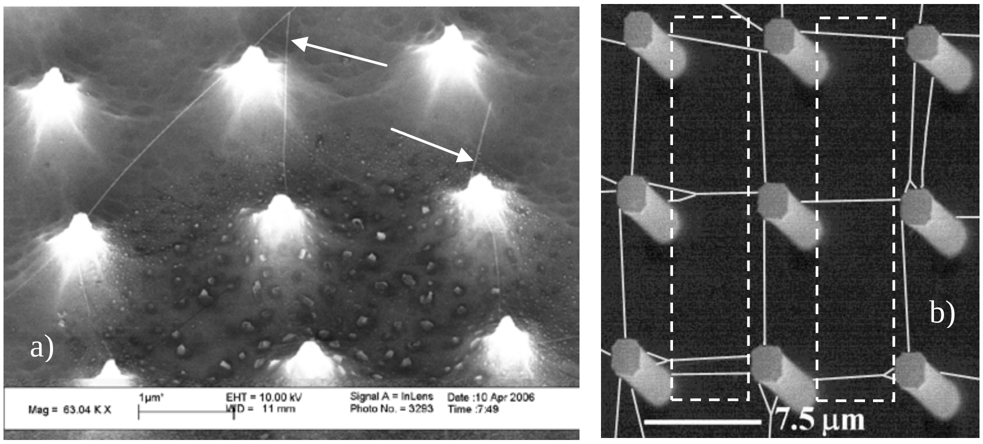

Figure 6.2: Examples of manufacturing of CNT interconnects in need of repair. Arrows indicate CNTs that need to be removed. Boxes indicate potential area that could be cleaned to produce better interconnects. Sample a) was fabricated by the author and sample b) is a network of suspended SWCNTs published by Franklin et al. [6.10]

6.1.2 Summary of Previous Carbon Nanotube Editing Techniques

The uniquely tunable electrical, mechanical, and structural properties of carbon nanotubes have made them a focal point of several nanoscience initiatives. A number of groups have investigated post-growth processing techniques for single CNT modification by a variety of methods, but mainly ion and electron beams.

Focused ion beams (FIB) provide a nanoscale energy source, which can be used to modify single CNTs. For instance, Raghuveer et al. demonstrated cutting and welding of a multiwalled CNT using a focused gallium ion beam [6.5]. Raghuveer et al. demonstrated the use of an ion beam but on larger size carbon nanotubes, in the 40 to 120 nm range, and only for nanotubes that have been suspended at both ends. It has been our own experience that larger carbon nanotubes are easier to cut with an ion beam without deforming them while smaller carbon nanotubes, in the 3-10 nm range, easily curl and deform under the influence of the ion beam. Free standing carbon nanotubes are even more susceptible to deformation. Therefore, it is not surprising that the ion milling method used by Raghuveer et al. only worked for well supported and larger nanotubes. Another disadvantage of using an ion beam, as described by Raghuveer et al., is the destruction of the CNT crystallinity. While FIB can be used to successfully cut and modify CNTs, there exists the inherent problem of ion-induced damage, an artifact of processing that may not be desirable. Therefore, other methods of CNT modification are also necessary.

In other research, CNTs have also been cut by electron beams in the presence of an oxygen precursor, where the close proximity of the injected vapor plume was shown to be of critical importance [6.11]. Photon irradiation [6.7, 6.8] has been shown to induce damage and cutting of CNTs - but without the deleterious effects of ion bombardment, but in a non-localized manner.

In order to satisfy the nanoscopic and low damage requirements for CNT cutting, other methods, such as electron beam modification have also been investigated. Gas precursor assisted electron beam modification has shown the best promise for individual-CNT cutting. In a comprehensive study Yuzvinski et al. [6.12] have demonstrated electron beam CNT-cutting using a water vapor as a precursor. Yuzvinski et al. have also investigated the use of nitrogen, hydrogen, and oxygen as precursors for electron beam CNT-cutting but none of them were as effective as water vapor. Martinez et al. [6.13] applied the above described technique by Yuzvinski et al. and used scanning electron irradiation normal to the symmetry axis of the CNT to cut the nanotube with high precision. Yuzvinski et al. and Martinez et al. also describe the flow of current though the CNT to improve the quality of the cutting process. Yuzvinski et al. and Martinez et al. have demonstrated the CNT cutting process only on one type of CNT configuration, double-clamped suspended CNTs, where both ends of the CNT are in contact with a substrate and there was no substrate directly under the cut CNT.

6.1.3 Mechanistic and Quantitative Description

Focused electron beam stimulated deposition and etching is similar to focused ion beam approaches. The process requires the delivery of a precursor gas to the substrate and a subsequent electron stimulated reaction to dissociate the gas species and initiate the deposition or etch process. The total reaction rate can be limited either by the gas delivery (mass transport limited) or by the electron beam dissociation (reaction rate limited). Figure 6.3a shows the neutral condition of the substrate and precursor gas without the presence of the electron beam. Figure 6.3b illustrates the selective electron deposition process in which precursor gas is dissociated under the electron beam leaving behind a condensed material. Figure 6.3c illustrates selective electron beam stimulated etching process in which dissociated species react with the substrate material and form volatile species which desorb from the substrate surface.

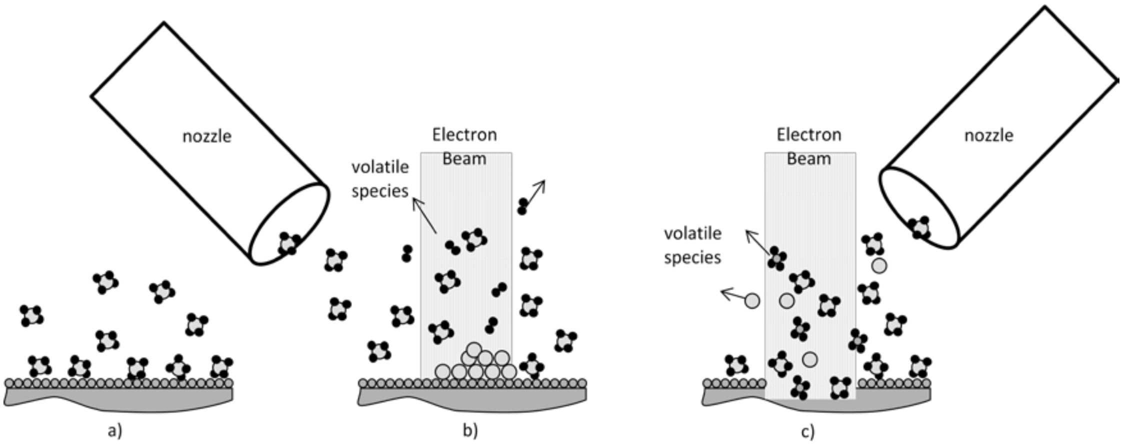

Figure 6.3: Schematic showing a) the substrate and precursor gas without an electron beam, b) a focused electron beam stimulated deposition process, and c) a focused electron beam stimulated etch process.

To control the focused electron beam stimulated process it is important to understand the variables that control the mass transport and the reaction rate. When a precursor gas (deposition or etch gas) is injected into the chamber it induces a flux of gaseous species onto the substrate. The molecular flux given by the kinetic theory of gases is given by:

$$\Gamma_{mol} = \frac{P}{\sqrt{2\,\pi\,m\,k\,T}} \left(\frac{\text{molecules}}{\text{s}-\text{m}^2}\right) \qquad \text{(Eq. 6.1)}$$

where P is the molecular partial pressure, m is the molecular mass, k is Boltzmann's constant, and T is absolute temperature. Employing Henry's Law for adsorption [6.9], a simple mathematical description of the surface density of adsorbed species (N_a) is given by:

$$N_a = \tau_a\,\Gamma_{mol} \left(\frac{\text{molecules}}{\text{m}^2}\right) \qquad \text{(Eq. 6.2)}$$

where τ_a is the mean stay time and Γ_{mol} is the molecular flux on the surface. The functional relationship for τ_a is given by:

$$\tau_a = \frac{1}{\upsilon} exp\left(\frac{E_{des}}{k\,T}\right) \text{ (s)} \qquad \text{(Eq. 6.3)}$$

where υ is an attempt frequency (typically related to the vibrational energy of the adsorbed species) and E_{des} is the desorption energy of the adsorbed molecule on the surface. Consequently, the mass transport of the precursor species is controlled by the localized partial pressure, the temperature, and the desorption activation energy of the gaseous precursor.

The electron stimulated dissociation rate of the precursor gas by the incident electron beam can be described by:

$$k_e = A_\sigma \, \Gamma_e \, \left(\frac{\text{reactions}}{\text{s}}\right) \qquad \text{(Eq. 6.4)}$$

where A_σ is the electron beam stimulated dissociation cross-section and Γ_e is the electron flux. The electron beam stimulated dissociation cross-section is a function of the electron beam energy, and the electron flux is simply dependent on the electron beam current density. These cross-sections are characterized by low energy threshold energy, a peak maximum at tens to hundreds of electron volts (eV) and a continual decline with increasing beam energy past the peak maximum. Consequently, the reaction rate is a function of both the beam energy (A_σ) and the current density (Γ_e).

The final mechanism of the process that is important is the desorption of by-products. The desorption of volatile by-products is critical in both deposition and etching. For deposition processes, by-products not adequately desorbed can be trapped into the deposited structure thus contaminating the deposited material. An example material set to illustrate this point can be described by the ideal reaction:

$W(CO)_6$ + electron → W (solid) +6CO (volatile)↑

If the carbon monoxide (CO) does not desorb fast enough, the carbon and oxygen can be trapped into the structure forming a $W_xC_yO_z$ film (for instance [6.14]). Insufficient desorption of volatile etch products can rate limit the etch process by temporarily passivating the near surface region. An example material set to illustrate this point can be described by the ideal reaction:

$2SF_6$ + 3Si (solid) + electrons → $3SiF_4$ (volatile)↑ + 2S

If the sulfur does not desorb from the silicon surface, as has been demonstrated in reactive ion etching [6.2], sulfur can passivate the silicon (or tungsten [6.3]) surface and inhibit the subsequent SF_6 adsorption and ultimately terminate the etch process. The by-product desorption step can be described by Equation 6.3 in which the residence time is a function of temperature and the by-product desorption activation energy.

The carbon nanotube etching process consists of supplying a stable precursor gas vapor into the SEM chamber. Some of the precursor gas molecules adsorb onto the surface of the CNT. Subsequently a primary electron beam electron, a backscattered electron, or a secondary electron emitted from the surface of the CNT inelastically collides with the adsorbed precursor molecule. The dissociated atoms of the precursor molecule react with the surface and form volatile etch product species. The etch product species desorbs from the surface of the CNT by thermal desorption or electron stimulated desorption. This removes material from the CNT and provides a new adsorption site for precursor vapor molecules to adsorb. The process is selective in that it requires the electron beam to induce the process.

6.2 EXPERIMENTAL SECTION

The research was performed utilizing two scanning electron microscopes, an environmental SEM used at the University of Tennessee at Knoxville, and a conventional non-environmental SEM used at Xidex Corp. in Austin, Texas.

6.2.1 Experimental Setup I

The first part of the experiments was carried out in a Hitachi S-4300SE/N variable pressure scanning electron microscope (VPSEM), using Hitachi's proprietary software controls for adjusting these variables. Beam energy was varied by changing the accelerating voltage, and beam current was modified by adjusting the condenser lens settings, as well as the use of variable, current-limiting apertures. Incident beam current was measured using a mounted Faraday cup connected to a digital picoammeter. The beam energies were varied in the range of 3-30 keV - a known range of energies within which the microscope performs very well. The beam current was in the range of tens of picoamperes to several nanoamperes. Based on our previous experience, this range of current provides the greatest opportunity of success. The Hitachi VPSEM was equipped with an in-house designed and built precursor vapor injection system, as described in Chapter 3. The pressure range was from 1-10 mPa, the upper limit of which is the maximum allowable pressure for operating in high vacuum mode.

6.2.1.1 Samples

The CNT samples used in the experiments were grown directly on the surfaces of silicon-based atomic force microscopy (AFM) cantilever tips and flat silicon pieces. Standard silicon based SPM tips were carefully dipped into solutions containing catalytic material. The SPM tips were then placed in a CVD oven and the CNTs were grown using a thermal CVD process. Typical CVD recipes were conducted with a flow rate of Ar/H_2 1000-2000 sccm to 1 sccm of ethylene at growth temperature of 750°C for 10 minutes. Depending on the concentration of the catalyst solution, and the amount of precursor gas used in the CVD process, CNTs tend to grow in a variety of number densities, sizes, and shapes. Some are loops extending from one part of the cantilever to another, some are free standing with only one end of the tube attached to the silicon, and still others are lying down on the silicon surface. The CNT sizes ranged from 10 nm to 40 nm and their lengths ranged from 100 nm to several microns. All the CNT samples and the CNT-based devices used to test the editing process were prepared by the author.

6.2.1.2 Demonstration of the CNT cutting process

The procedure for localized CNT cutting was to first identify a CNT and zoom in enough to locate the cutting position with nanometers precision, typically somewhere between 60kx and 300kx magnification, then rotate the beam until the scan direction was perpendicular to the CNT, with the center of the scan area intercepting the desired cut location. The precondition was to have a significant water vapor pressure in the SEM chamber, in the range between 1×10^{-4} Pa to 2×10^{-2} Pa, or until the SEM sensors trip the high vacuum condition. In environmental SEMs this pressure can be higher, but too high pressure may not be practical as it limits imaging resolution. CNTs with various sizes were cut by scanning the e-beam across the CNT at a high rate (30 loops/frames per second) in a line scan mode. The secondary electron image was observed during the line scanning and the CNTs were observed to etch with an obvious endpoint where the secondary electron image becomes a flat line where the CNT was observed. Figure 6.4 illustrates a line scanning secondary electron image during etching and immediately after reaching end point.

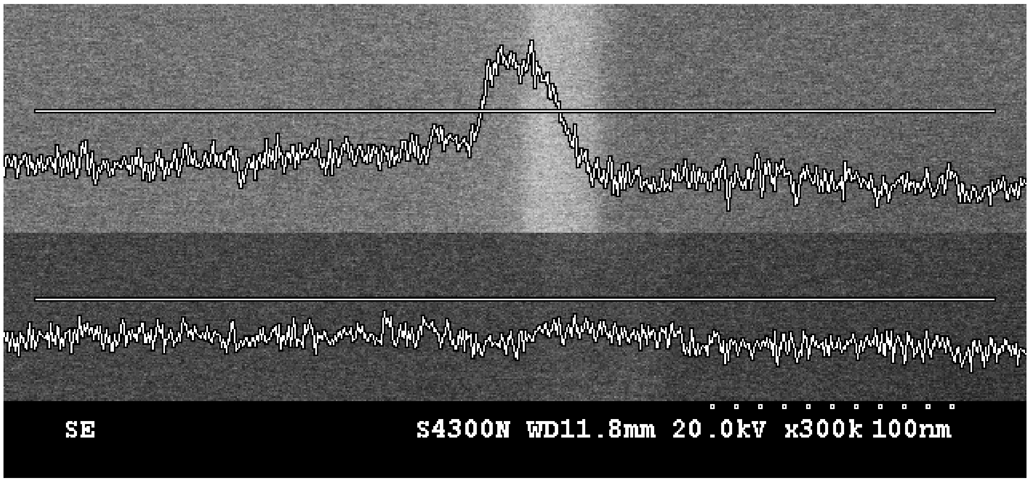

Figure 6.4: Secondary electron imaging example during line scanning across a CNT (top) and after CNT is cut (bottom)

The procedure was also demonstrated for several different CNTs cut at various locations on the AFM cantilever sample. Figures 6.5 and 6.6 show various CNTs before and after cutting. The electron beam conditions were set to 20 keV beam energy and 754 pA measured sample current, at 2×10^{-2} Pa of total SEM chamber pressure where most of it was due to water vapor. Figure 6.5 shows the use of a box scan instead of a line scan to successfully cut a CNT laying on a surface. The CNT etching was performed using full screen TV scan at 500 kx magnification. In this example the CNT was cut in 11 seconds. Figures 6.6a (before) and 6.6b (after) show the use of a line scan to cut a set of suspended CNTs with a great precision and Figures 6.6c (before) and 6.6d (after) show the use of a box scan to successfully cut a pair of free standing CNTs that may be connected in a loop at the free end.

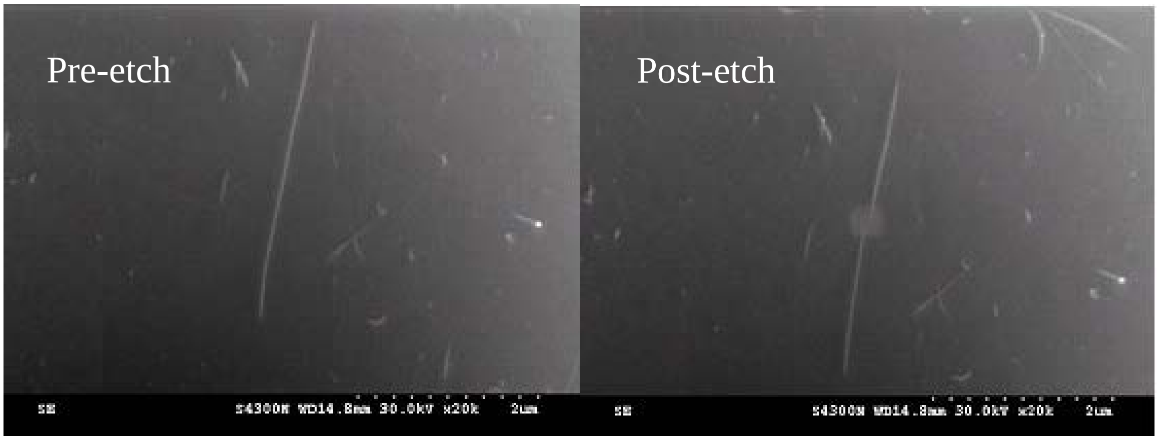

Figure 6.5: Example of carbon nanotube cutting using a box scan.

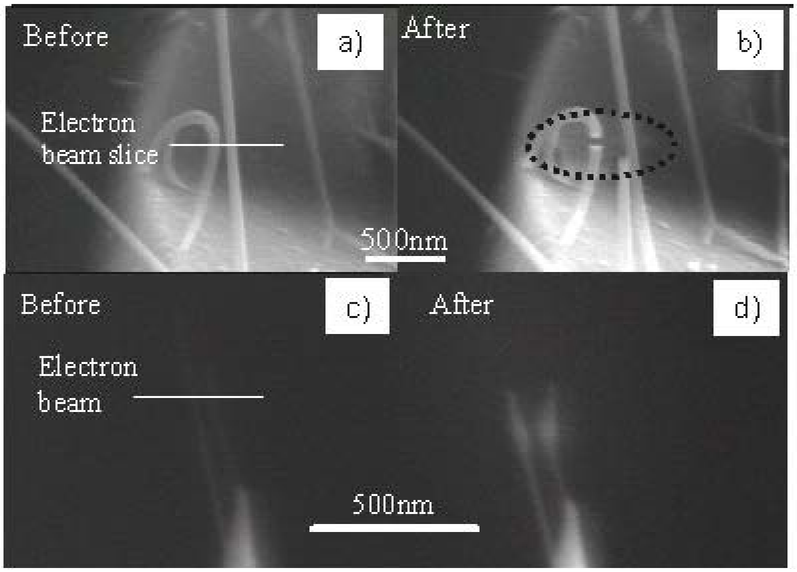

Figure 6.6: The CNTs in image a-b) were etched using a line scan, and the CNTs in image c-d) were cut in a box scan.

The time to cut each CNT varied, depending mainly upon the size of the CNT. Small diameter CNTs tend to cut faster than larger CNTs. We found that the cutting time is roughly proportional to the beginning size of the CNT, as seen in Figure 6.7. Sometimes while attempting to cut two CNTs beside each other, one would cut while the other would not (for the given time). We attribute this to the slightly different diameter of the nanotubes or possibly due to the different number of concentric walls in each nanotube. Our CNT growth process produces multiwalled CNTs with 4 or more walls.

The variability in cutting time as a function of the nanotube diameter is not a problem due to the use of the line scan profile of the nanotube as it was cut. The secondary electron image of the CNT was observed during etching with line scanning with an obvious endpoint where the secondary electron image becomes a flat line. Figure 6.8 illustrates a time series of 1 minute intervals during the cutting of a CNT showing the size of the tube shrinking and the obvious endpoint signal. Using this technique we can in practice partially cut a CNT if needed.

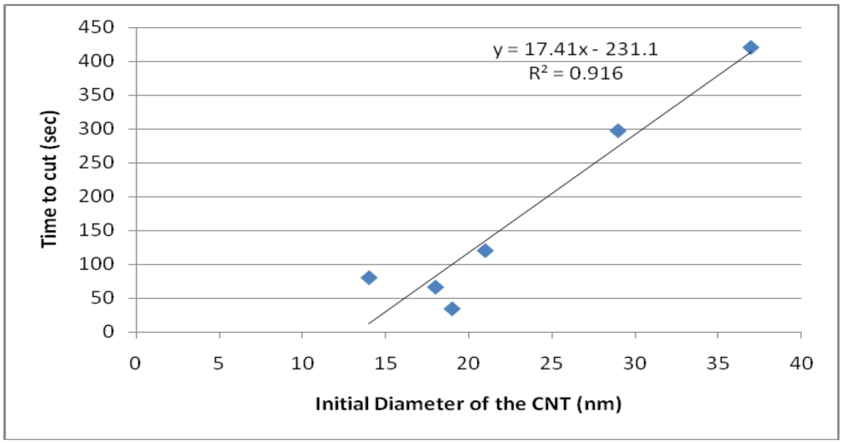

Figure 6.7: Relationship between time to cut and the initial diameter of the CNT

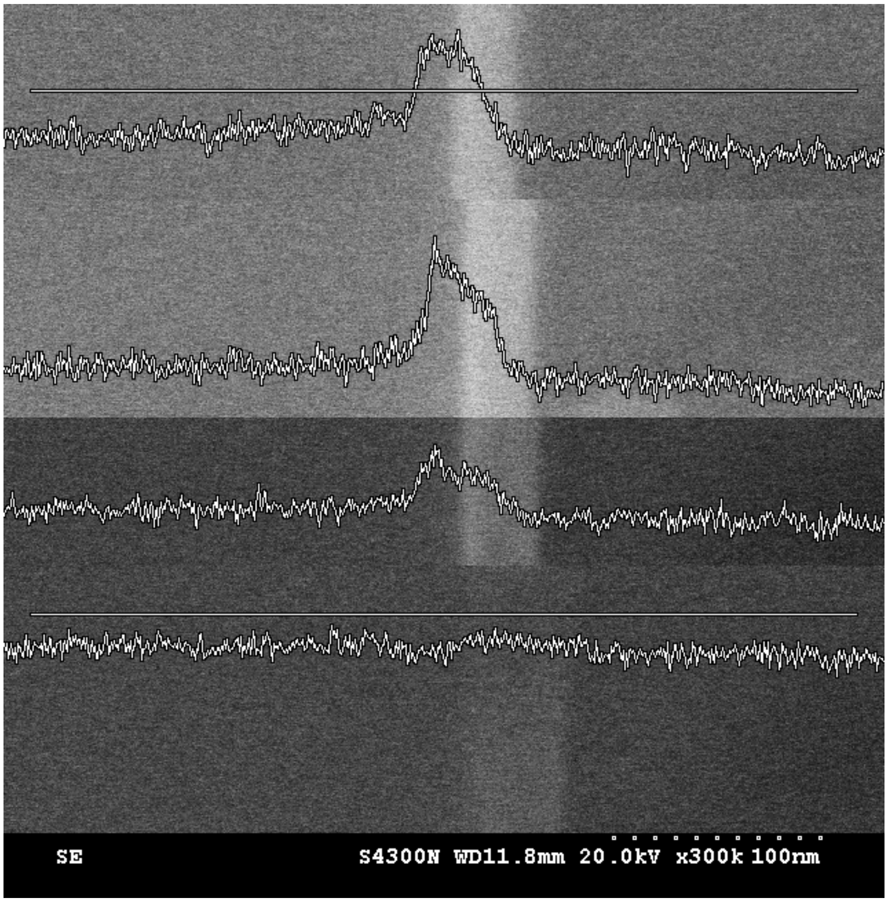

Figure 6.8: Progression of line scanning secondary electron image towards end point

We found that some CNTs did not cut even after a considerable amount of time. The cause of this was most often drifting of the beam up and down the CNT. As the beam drifts around the areas that had been etched would then be deposited on as the beam drifted away and the electron flux lowered to a range where deposition dominates over etching. Care must be used to remove any mechanical drifting in the stage and the AFM tips and the injection needle must be well grounded in order to eliminate any charging and subsequent beam drift. Once a steady beam is acquired, then CNT cutting is a fairly routine procedure.

6.2.1.3 Study of the CNT Etching Parameters

We have noted that in some cases the remaining CNT size has grown during the cutting process. We attribute this to a competitive carbon deposition process that occurs in parallel with a carbon etching process. It is common in all SEMs to have carbon pinning during exposure to the electron beam. There is a base pressure of carbon containing species in the chamber, mostly due to back streaming oil from the roughing pumps and adventitious adsorbed carbon on the sample. These back streamed carbon species adsorb on the surface in the chamber and are mobile. Electrons that impact these mobile species result in dissociation to amorphous carbon or cross-linking of chains to create immobile deposits of carbon. These processes are competitive with the etching process, and in order to result in a net etching rate, the competitive deposition must be overcome. Figure 6.9 illustrates an example of carbon deposition by the e-beam while imaging a CNT. The left image is before and the right image is after the CNT was continuously imaged for 30 minutes using a 5.0 keV beam and a beam current of 8 pA. Note that there is significant deposition on the CNT.

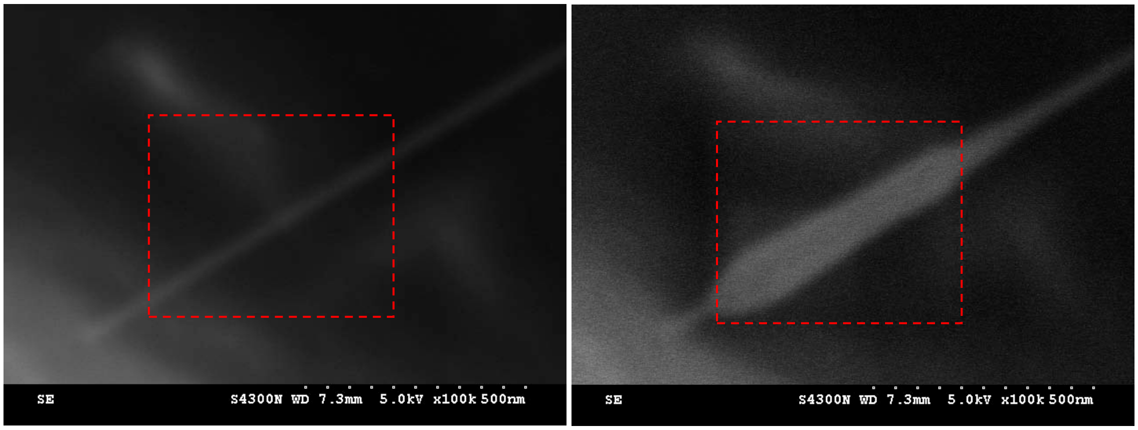

Figure 6.9: The CNT was imaged by the SEM scanning the region highlighted by the dotted red line. There was significant deposition on the CNT due to carbon contamination in the SEM chamber deposited during exposure to the electron-beam.

Toth et al. [6.15] observed that deposition versus etching switching for a generic gas species can be controlled by the electron flux. For either deposition or etching, the rate of reaction is proportional (and limited by) to the flux of electrons, at low electron flux, until the electron flux is sufficient to deplete the precursor gas coverage. Afterwards, the rate becomes limited by the mass transport of new precursor to the surface. This results in a constant rate of reaction for higher electron fluxes. In addition, at low electron fluxes, the deposition process is more efficient than the etching process due to a higher dissociation probability of the carbon deposition precursor than the dissociation probability of the water. As electron flux increases, the deposition process becomes mass transport limited by the arrival rate of deposition precursor. Provided that there is a sufficiently high pressure of etch precursor; as electron flux continues to increase, the etch process rate continues to increase in proportion to the electron flux. The etching process then becomes more efficient than the deposition and net etching results (Figure 6.10 – left). The net etching rate can be improved by removing the source of hydrocarbon contamination. This lowers the deposition rate enabling a larger net etching rate (Figure 6.10 – right). Increasing the local water pressure increases the gas coverage on the surface resulting in a higher etching rate, improving the net rate towards etching (Figure 6.11 – right). As illustrated in Figure 6.11, the etching rate can also be improved by cleaning volatile carbon containing species out of the SEM chamber (Figure 6.11 – right), increasing as much as possible the precursor pressure at the CNT surface, and increasing the electron flux as high as possible.

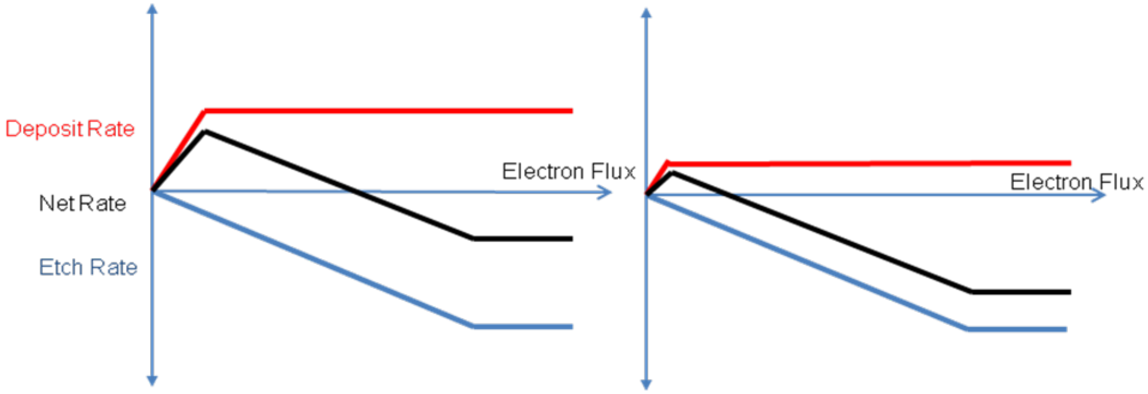

Figure 6.10: Deposition rate, etching rate, and net rate versus increasing electron flux

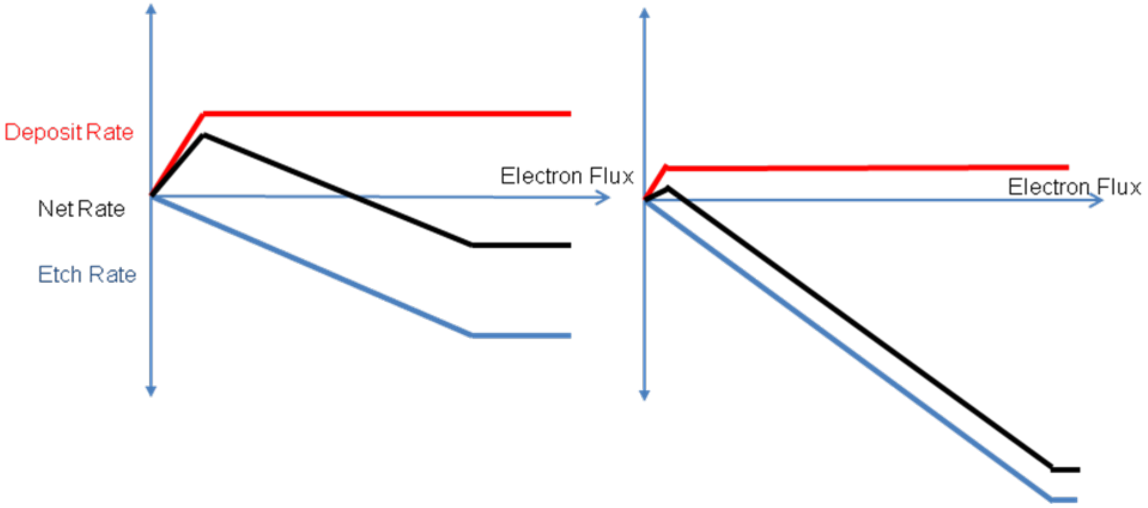

Figure 6.11: Deposition rate, etching rate, and net rate versus increasing electron flux

Carbon containing species can be removed from the SEM chamber by the use of an oxygen plasma source (in our case an EVACTRON™ cleaning system from XEI Scientific, Inc). The system supplies low power RF plasma to atmospheric gases leaked into the chamber through a metering valve. The low power plasma provides enough power to ionize and dissociate O_2 but not enough to ionize N_2. This provides a supply of oxygen radicals to the chamber. We used a power setting of 14 W forward RF power and a pressure of 0.4 Torr (~53 Pa) to maximize the creation of oxygen radicals. The oxygen radicals react with the mobile carbon-containing species in the chamber, forming carbon monoxide, carbon dioxide, water, and hydrogen molecules. These volatile gas species are subsequently pumped from the chamber by the vacuum system. The result is the removal of species from that chamber that lead to unwanted carbon deposition.

We varied the SEM chamber plasma cleaning time followed by cutting a single CNT in multiple places. The procedure was to vent the SEM chamber to atmosphere, open the chamber doors, and leave the chamber at atmosphere for 1 hour. The system was then pumped to a base pressure of 5.0×10^{-4} Pa and the beam was set to a 100 pA current at beam energy of 20 keV. The CNTs were cut at a chamber background pressure of 2.0×10^{-2} Pa of water, with the exception of the control run with zero water flow and a chamber background pressure of 5.0×10^{-4} Pa. The cutting time was 120 sec or CNT cut endpoint, whichever came first. The images of the processed CNTs are shown in Figure 6.12. For the control, a net deposit was observed due to the carbon contamination in the SEM chamber. With little or no cleaning, the competitive deposition was not overcome by the etch process, and a net deposit was observed. With sufficient cleaning time the CNT was able to be cut. For plasma cleaning of about 2 minutes or more the net reaction was etching.

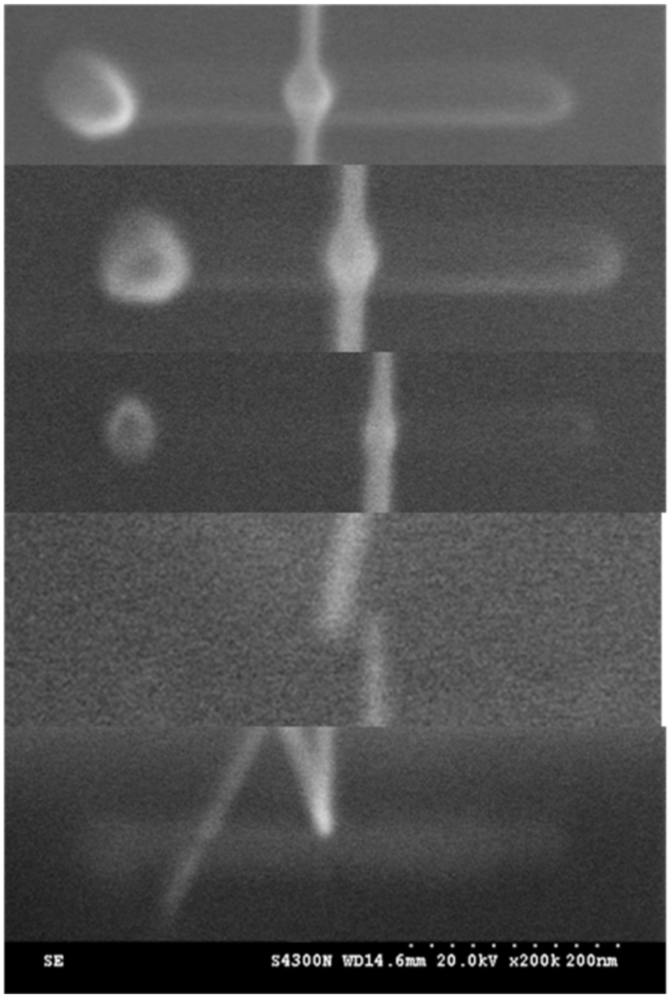

0min EVACTRON (0 flow of H_2O)
+38nm net deposit width on 17nm CNT
120sec process time

0min EVACTRON
+35nm net deposit width
120sec process time

1min EVACTRON
+15nm net deposit width
120sec process time

2min EVACTRON
-17nm net deposit width
90sec process time

4min EVACTRON
-17nm net deposit width
46sec process time

Figure 6.12: RF plasma cleaning time vs. net etching/deposition experiment

We investigated the electron flux influence on the etching rates with an experiment in which the beam current was changed by adjusting the SEM condenser lens, while the limiting aperture and working distance remained constant. The background pressure was also maintained constant at 2.0×10^{-2} Pa. The time to cut a nanotube was observed by the end point of the secondary electron image during etching and the etch rate was calculated by dividing the diameter of the CNT by the time to cut. The results from this etching are plotted in Figure 6.13 below. We observed that the etch rate improved with increasing probe current. We assume that the probe size is diffraction limited and therefore the peak electron flux is proportional to the beam current. In this assumption, it is seen that the etching is electron flux limited, that is the reaction rate increases in proportion to electron flux and does not fully reach a mass transport limited regime. That is not to say that under a fixed beam a mass transport rate limited regime would not occur, but rather that here the scanning rate is fast enough that the precursor does not deplete during the beam dwell time. Also, it should be noted that these CNTs were cut in a chamber that had been thoroughly cleaned of hydrocarbon contaminants.

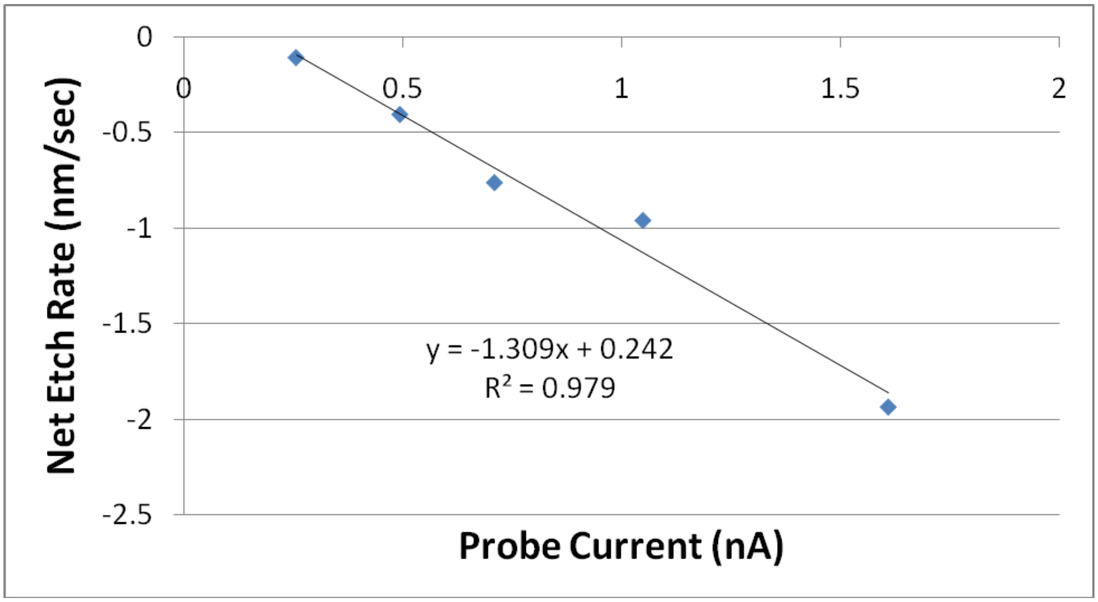

Figure 6.13: CNT etch rate versus beam current

A more complete full factorial experiment was conducted to investigate the effects of beam current, beam energy, and plasma cleaning time. The experimental parameter space was as follows:

Beam Energy – 1=5 keV, 2=12.5 keV, 3=20 keV

Beam Current – 1=10 pA, 2=45 pA, 3=80 pA

Cleaning Time – 1=4 min, 2=20 min

The main effects are plotted in Figure 6.14. The results indicate that all three parameters are statistically significant. It can be observed that the beam current and cleaning time have strong linear effects. As expected, increasing the beam current produces switching from net deposition to net etching. Increasing the cleaning time gives improved performance as the source of carbon contamination is reduced. The energy dependence shows a peak explained by the competing energy dependencies of the dissociation probabilities of the deposit and etch precursors.

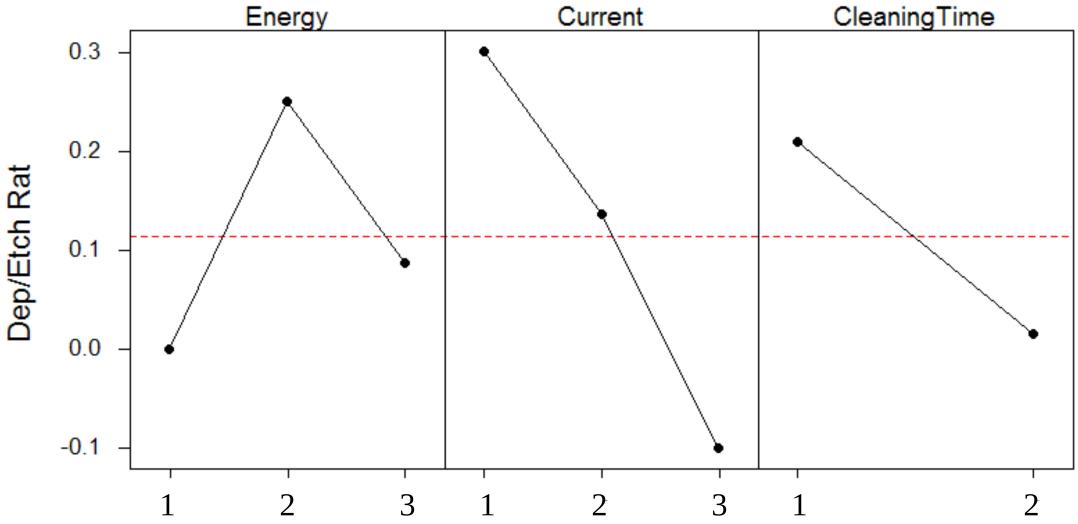

Figure 6.14: Main effect plot from full factorial DOE

6.2.1.4 CNT Area Etching

We believe ours to be the first demonstration that water vapor electron beam induced etching can also be used to clean areas of carbon debris from a silicon surface as opposed to etching/cutting individual carbon nanotubes. An area can be scanned using the same conditions as those used for CNT cutting and most of the carbon material in the field of view is cleaned within minutes. For example a 1.5 µm x 0.75 µm area with CNTs lying on the silicon surface was cleared using area CNT etching. All CNTs in the scanning region were removed after 3 minutes of etching, as shown in Figure 6.15. In this example the beam energy was 30 keV and the chamber pressure was 10 mPa. It is clear from the results in Figure 6.15 that the selective etching using water vapor cleaned an entire microns scale area of its carbon nanotubes without modifying the neighboring nanotubes. Figure 6.16 shows before and after images of an area cleaned by selective CNT etching. The area inside the red dotted lines was scanned for 10 minutes, and then the wider (after cleaning) image on the right was captured to show that the non-scanned areas are not affected. Large CNTs in the field of view remain, as they would require longer exposure times to etch under these conditions. Alternatively, larger aperture settings could be used to increase the current beyond the ~ 1.2 nA which was used in this experiment.

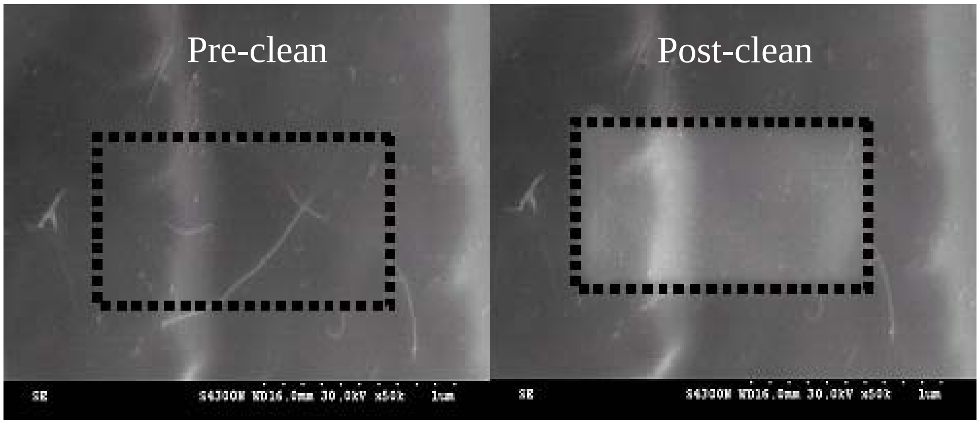

Figure 6.15: 1.5 µm x 0.75 µm area CNT etching with water vapor precursor. It is clear that the etching using water vapor cleaned an entire microns-scale area of its carbon nanotubes without modifying the neighboring nanotubes.

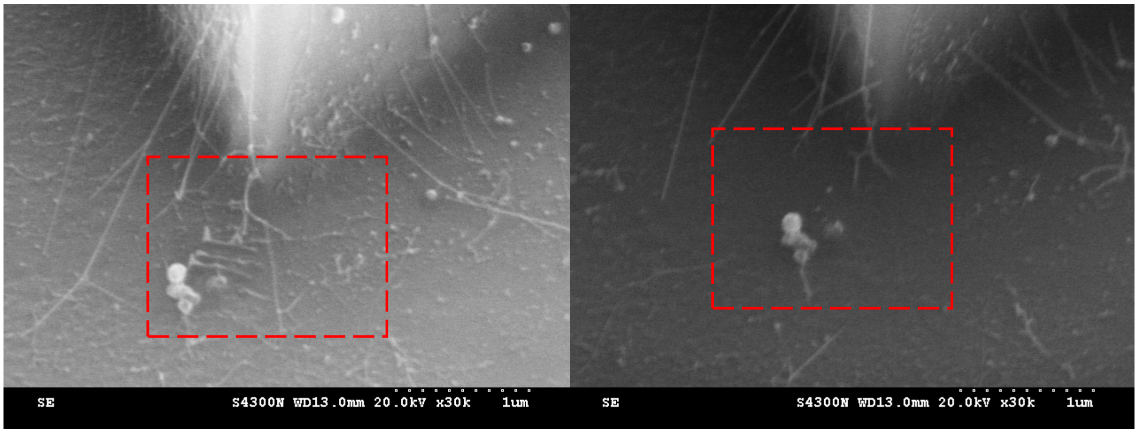

Figure 6.16: Before (left) and after (right) area cleaning

6.2.2 Experimental Setup II

6.2.2.1 Demonstration of improved CNT cutting efficiency

The CNT cutting process needs to be efficient and fast to support rapid CNT editing. The initial results have shown that for a fixed CNT etching rate the etching efficiency depended on the electron beam energy, the beam current, and the precursor pressure (the water vapor partial pressure). These findings were also reported by others [6.12]. These results show that higher precursor pressures lead to higher CNT etching efficiency. The local precursor pressure, at the sample, and not the average chamber pressure (background pressure) determines the precursor flux and therefore the CNT etching. Then the question becomes, can the optimal precursor pressure be easily achieved and adjusted? The precursor flux as given by the kinetic theory of gases is:

$$\Gamma_{\mathrm{mol}} = \frac{\mathrm{P}}{\sqrt{2\,\pi\,\mathrm{m}\,\mathrm{k}\,\mathrm{T}}} \left(\frac{\mathrm{molecules}}{\mathrm{s{-}m^2}}\right) \qquad \text{(Eq. 6.1 repeated from above)}$$

where P is the local precursor pressure, m is the molecular mass, k is Boltzmann's constant, and T is absolute temperature. We can easily measure the average chamber pressure but it is impossible to directly measure the localized precursor pressure at the sample. Localized precursor pressure however can be computed by knowing the chamber pressure and the gas nozzle geometry. We measured the optimal precursor pressure to be 1-2 $\times 10^{-2}$ Pa, very close to the upper operating limit of most SEMs. A higher precursor pressure would increase the CNT etching efficiency but it would also require the use the SEM instrument in an environmental mode, an expensive and more complicated SEM option.

Therefore, we investigated whether the CNT etching efficiency can be increased by increasing the local precursor pressure and flux but without increasing the chamber pressure. This was achieved by modifying the design of a conventional gas injection/delivery system, and in particular enabling better control of the nozzle-sample distance. We expected that when we decreased the nozzle-sample distance we would achieve higher localized precursor pressure and flux while maintaining lower chamber pressure. Because the gas flow from a nozzle spreads in a spatial cone, for a fixed gas flow the pressure (force over unit area) and the flux (flow over unit area) will increase for decreased nozzle-sample distance. Then, due to the high pressure gradient, the background pressure will be maintained low. With this approach we planned to achieve optimal localized precursor pressure and flux at chamber pressures of less than 1×10^{-2} Pa, and in the range of 10^{-3} to 10^{-4} Pa.

6.2.2.2 Experimental Setup II

The localized precursor pressure experiments were carried out in a Hitachi S-4000 non-environmental SEM with custom built gas delivery/injection system. The purpose of the gas delivery system was to leak water vapor gas to the sample inside the SEM. The gas delivery system consisted of components internal to the SEM and components external to the SEM, as shown in Figure 6.17. The liquid water precursor was stored in a special stainless steel reservoir with a shut off valve that could be detached from the rest of the system and refilled with water as needed. Form the reservoir to the vacuum chamber the gas delivery takes place through a ¼ inch stainless steel tube and has two needle valves (which can also stop the flow) connected in series. We selected two valves to better control the gas flow. The vacuum feedthrough has ¼ inch Swagelok^{TM} connections on both sides of the flange. The two valves are connected on the external side. On the inside, the ¼ inch tube is reduced to a⅛ inch size and is connected to a ⅛ inch PTFE flexible tube using Swagelok^{TM} connections. We used Gauge 20 PTFE tube with 12 inches of length for the gas delivery inside the SEM. Gauge 20 had 1.68 mm OD and 0.86 mm ID. The ID and the length of the tube were selected to allow gas conductance from the source to the needle but at the same time to be evacuated by the SEM vacuum in a short time period after the gas flow is stopped by the valves. The Swagelok^{TM} was selected to allow testing of different tube sizes and lengths.

A Gauge 26 metal needle acting as a gas nozzle was epoxied at the far end of a plastic delivery tube. The Gauge 26 needle had 460 μm OD and 254 μm ID. The plastic delivery tube and the needle were connected to the boom of a nanomanipulator with the needle extending from the end of the boom so as to be able to come in close proximity to the sample. For this investigation the nozzle angle (the angle between the sample and the centerline of the nozzle) was 0° so as to allow close positioning of the nozzle to the sample. With the help of the nanomanipulator the nozzle could be placed from 1 mm to 50 μm with respect to the sample. This capability was the essence of our design and the localized pressure experiments. The system used in these experiments was the bases for a commercial product, Parallel Gas Injection System (PGIS) [6.16], developed by Xidex Corporation.

We determined the conductance limited throughput of our gas delivery system by opening all the valves of the system all the way to the water reservoir and determining the maximum equilibrium pressure that was reached. Our SEM can routinely reach a base pressure of about 2×10^{-7} Torr with overnight pumping. During the day and with opening the main chamber the base pressure is about 2×10^{-6} Torr. The base pressure obtained for the latest gas delivery system, when the valves were fully open was 5.5×10^{-5} Torr. This pressure was stable after many hours of operating the SEM. Upon closing all the valves of the gas delivery system the chamber pressure returned to below 1×10^{-6} Torr in 20–25 minutes. Quick evacuation of the gas delivery tubes makes the system practical for everyday operation.

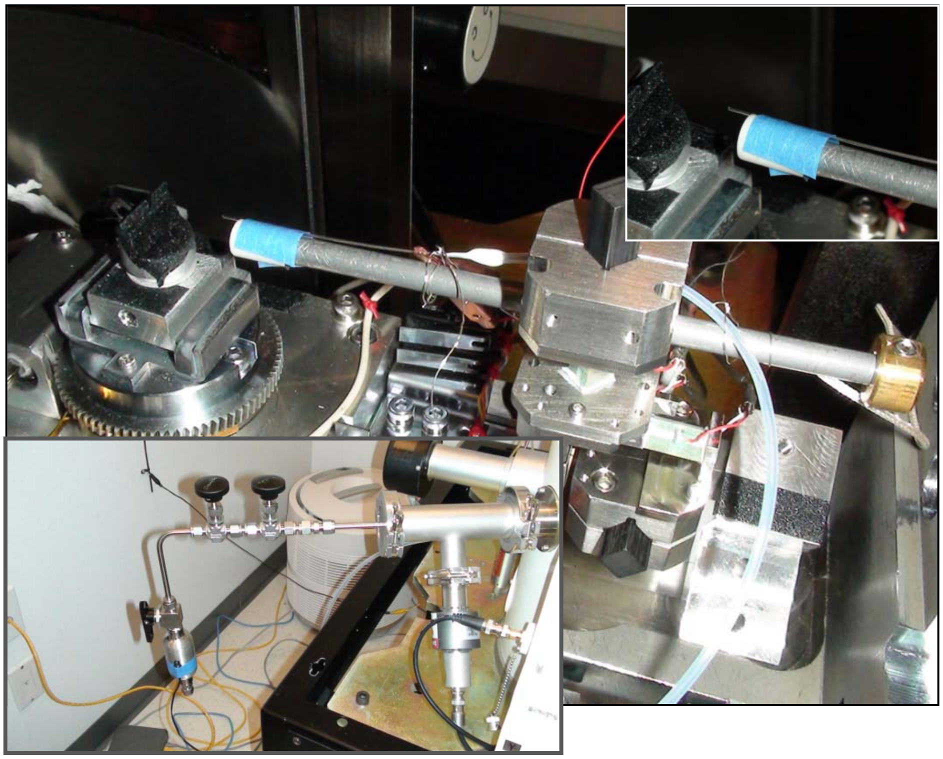

Figure 6.17: Electron beam induced etching system with novel nanomanipulator based gas delivery/injection system.

6.2.2.3 Relationship between the nozzle-sample distance and the localized precursor pressure

We demonstrated improved etching of carbon nanotubes and correlated it to the small distance between the nozzle and the sample. We therefore observed that the small distance between the nozzle and the sample results in the increase of the localized gas pressure which in turn is responsible for the improved etching of carbon nanotubes. Because it is impossible to directly measure the localized precursor pressure at the sample, the local pressure can be computed by knowing the chamber pressure and the gas nozzle geometry. Details of this computation are described by Kohlmann et al. [6.8].

We first conducted tests to check if the presence of a needle 100s of microns in size in close proximity to the sample would distort the SEM image and make it impossible to image the nanotubes, therefore making this approach infeasible. We ran initial tests by moving the needle from 1000 μm to 50 μm away from the sample and by imaging with high resolution (35 kx and above) on the very same CNT sample. These runs revealed that the gas delivery needle had to be electrically grounded for this approach to work. We discovered that the grounding had to have resistance of less than 1 kΩ to be effective. This was achieved by clipping an alligator clip to the needle and grounding it via a short length of hook-up wire to the SEM walls.

We introduced the gas into the chamber through the nozzle, with pressures in the range of $1-5\times10^{-5}$ Torr. The presence of the gas introduced a gas ionization that was observed via electron imaging. Figure 6.18 shows the visualization of the water vapor flow from the nozzle as the nozzle-sample gap was reduced. We explain the flow lines as result of the electron beam induced ionization of the water molecules. We used the flow streamlines to estimate the gas spread angle β, as defined by Kohlmann et al. [6.8]. The average spread angle was estimated to be 34°. The results of the tests show that with this SEM we could not image well the CNTs at beam energies of more than 20 keV but CNT imaging was fine for lower beam energies. The larger beam energies also introduced sample charging and drift. Effective CNT etching requires stable imaging for several minutes at high magnification.

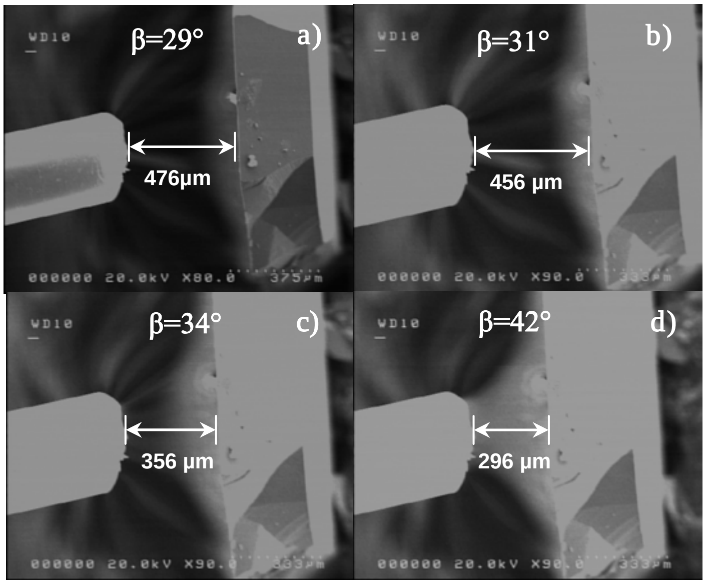

Figure 6.18: Visualization of the water vapor flow from the nozzle as the nozzle-sample gap was reduced. The gas spread angle β is estimated from the streamlines.

The next question we had to answer was at what instrument settings CNTs could be etched. We investigated beam energies of 20 keV, 10 keV, and 5 keV. The highest beam energy also produced the largest sample currents, in the range of 1–2 nA, but resulted in no CNT etching. At medium beam energy the sample currents were in the range of 120 pA but also resulted in no CNT etching. The most effective was the beam energy of 5 keV. We were able to cut CNTs with modest sample currents of 10–80 pA, as shown in Figures 6.19 and 6.20. Although the etching process is slower for low currents, one benefit of the low currents was that the etching process is more selective. For example, Figure 6.19 shows a full cut to the middle CNT but the large CNT to the left and the CNT to the right are only partially cut. Similarly, Figure 6.20 shows a full cut to the right CNT but a partial cut to the CNT on the left.

Testing the selective CNT cutting of larger nanotubes was more difficult and resulted in partial CNT cuts. Figure 6.21 shows partial cutting of a 90 nm thick CNT, at 5 keV beam energy, 120 pA sample current, and 3×10^{-5} Torr chamber pressure. After 14 minutes the CNT was still not cut but closer examination shows that there was a split (hole) made in the CNT as a result of the CNT etching. The splitting of the CNT was not expected but it may be used in future for more advanced CNT studies.

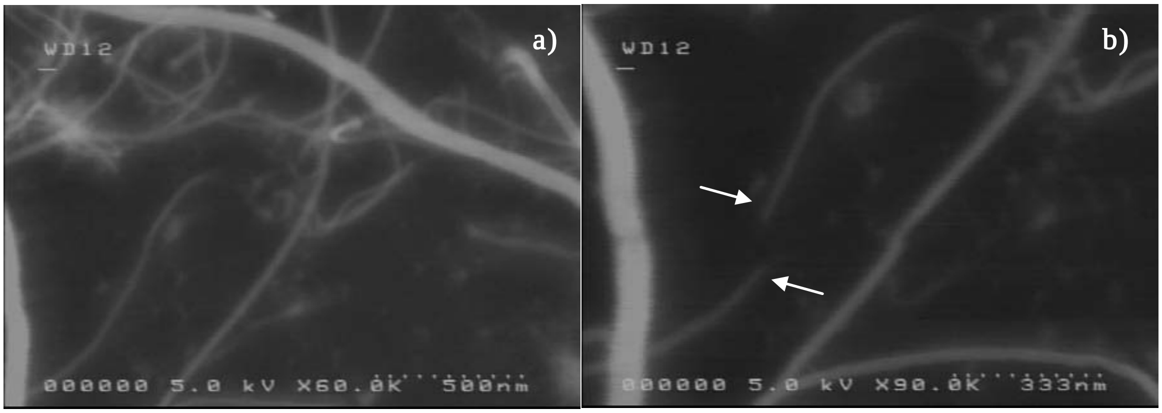

Figure 6.19: Selectively cutting a CNT at low sample currents (10–80 pA), before (a) and after (b). Note that the large CNT to the left and the CNT to the right are only partially cut.

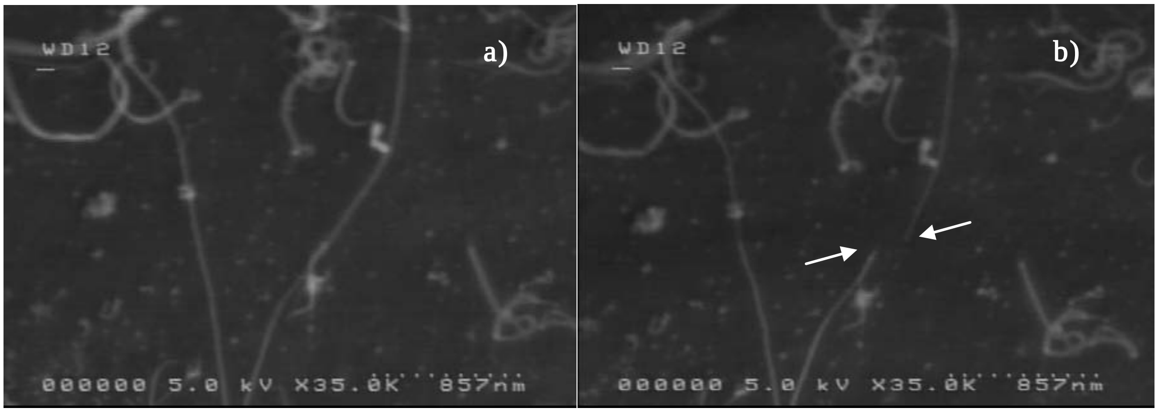

Figure 6.20: Selectively cutting a CNT at low sample currents (10–80 pA), before (a) and after (b). Note that the CNT to the left is only partially cut.

It is clear from the results in Figure 6.21 that the selective etching using water vapor cleaned entire microns size area of its carbon nanotubes without modifying the neighboring nanotubes.

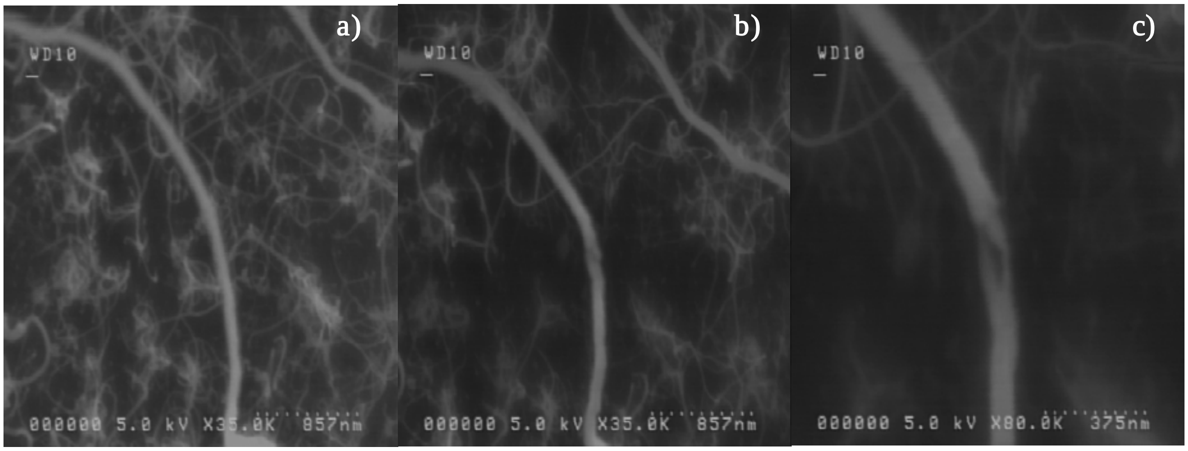

Figure 6.21: Partial (non complete) cutting of a 90 nm diameter CNT, before (a), after 14 minutes of etching (b), and a split in the CNT diameter due to the partial cutting (c).

The SEM current was controlled with the Condenser Lens and the Lower Aperture. With currents of less than 10 pA we could not etch a CNT in a reasonable time of less than 4 minutes. A summary of the beam energies, currents, and SEM settings we investigated are provided in Table 6.1.

Table 6.1: Summary of the investigated beam energies, currents, and SEM settings

Beam (keV)	Sample Current (pA)	Condenser Lens	Aperture	CNT Etching
20	1000 to 2000	3	1	did not cut any CNT
10	120	3	1	did not cut CNTs in 4 min or less
5	10 to 80	3	1	cut most CNTs
5	30	5	1	can cut CNTs
5	8	5	2	did not cut CNTs in 4 min or less
5	3	9	2	did not cut CNTs in 4 min or less

Next we investigated the relationship between the nozzle-sample distance and the etching time and rate. The tests were conducted with beam energy of 5 keV and average chamber pressure of 5.2×10^{-5} Torr. We measured the etching time t_{etch} and the sample current. The etching time was recorded as the time interval from the beginning of the electron beam scan until the CNT was completely cut, as shown in Figure 6.4 and described in the associated text. The experimental etching rate was computed by dividing the size of the etched CNT, which had an average diameter of 25 nm, with the etching time:

$$Etch\ Rate = \frac{d_{cnt}}{t_{etc\ h}} \qquad \text{(Eq. 6.5)}$$

For this experiment we changed the needle-sample distance from 87 μm to 328 μm by doubling the gap with each iteration, and then we returned back to the smallest gap we could use for that sample, 76 μm, to verify that we were not building up some bias. Figure 6.22 shows the result of this trial. To be consistent, all CNT cuts were done on the same multi microns long carbon nanotube where each cut was few microns away from the other. For a gap of 164 μm we can see that the CNT was cut in a segment. During these experiments we also kept the magnification the same for all trials, at 35 kx for imaging and 100 kx during etching. Table 6.2 lists all the parameters for this experiment.

Table 6.2: Summary of the experimental results measuring etch rate as function of the nozzle sample distance.

Gap (μm)	Sample Current (pA)	Etch Time (sec)	Etch Rate (nm/sec)
76	15	55	-0.457
87	10	110	-0.228
164	20	170	-0.148
328	30	230	-0.109

Gap (μm)	Gap Image	CNT Before Cut	CNT After Cut
76	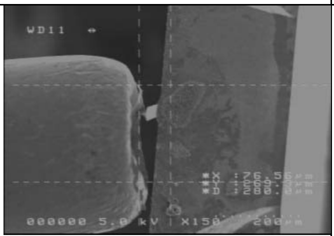		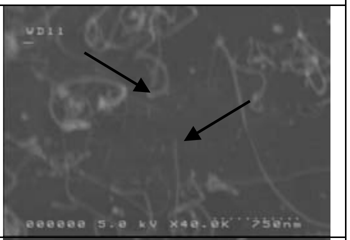
87	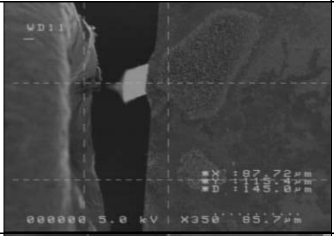	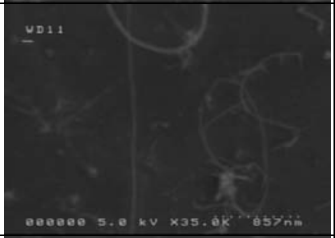	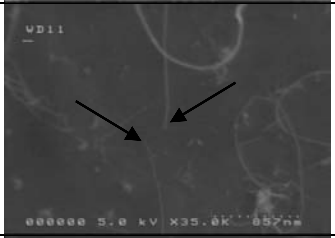
164	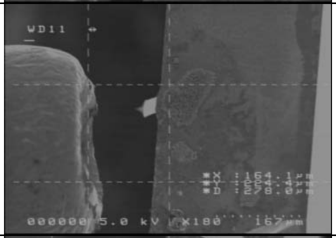		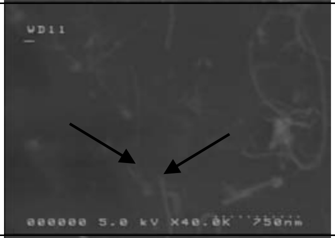
328		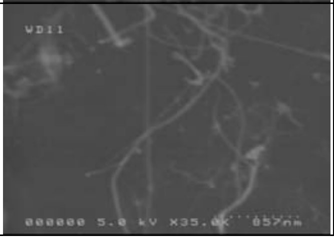	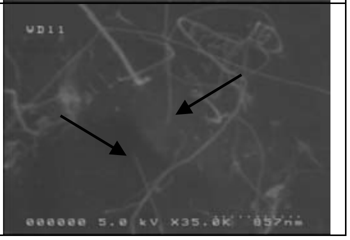

Figure 6.22: Demonstration of gas delivery system fixed to a nanomanipulator that allows precise positioning of the gas nozzle to the sample with a rage of 50 μm to 1 mm and more. The resulting nozzle proximity results in improved CNT etching capabilities.

One important conclusion for this experiment is that the etching time and rate improved for a smaller gap between the sample and the nozzle, as shown in Figure 6.23. We also observed a trend that for a smaller gap the probe current decreased, as shown in Figure 6.24. We interpret the change in the probe current as a function of distance as being due to ionization and competitive positive current flow which increases with decreasing spacing because of the enhanced local pressure. Because the smaller nozzle distance shows faster etching rates and lower sample currents, the results from Figures

6.23 and 6.24 lead to a conclusion that the local pressure is responsible for the increased etching rate.

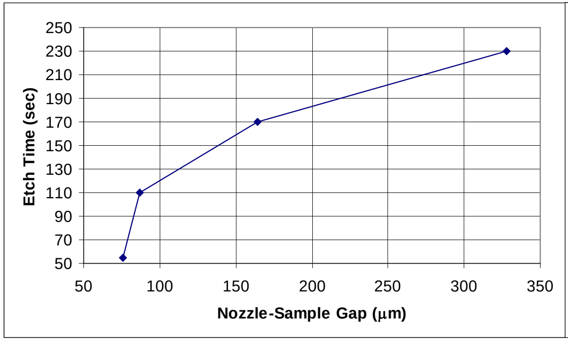

Figure 6.23: Demonstration of improved CNT etching time (etching rate) vs. nozzle-sample distance.

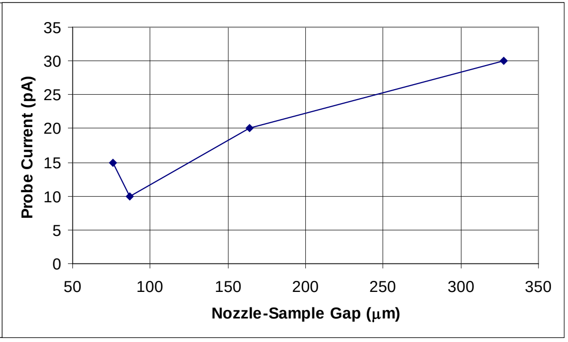

Figure 6.24: Probe current vs. nozzle-sample distance.

The benefits of achieving optimized localized precursor pressure and flux at reduced chamber pressures are multiple. First, the higher optimized localized precursor pressure will result in better CNT etching efficiency and therefore in faster etching times. Furthermore, at desired optimized localized precursor pressures the chamber pressure will be lower, increasing the lifetime of the SEM filament and decreasing the maintenance of the SEM tool, and in particular the ion pumps. The lower chamber pressure also means that the CNT etching can be practiced in simpler less-expensive non-environmental SEMs. Finally, operating the SEM at lower chamber pressures means less gas scattering and therefore less beam spread, resulting in more precise beam operation.

6.2.2.4 Cantilevered CNT Etching

We also demonstrated that the more efficient carbon nanotube etching, with optimized localized precursor pressure, works for free standing (cantilevered) carbon nanotubes. Figure 6.25 shows the process of cutting two free standing CNTs with different diameter. After an initial etching attempt the thinner CNT was completely etched away while the thicker CNT was unchanged. It is also possible that the smaller

CNT did just bend away. After some additional etching time the thicker CNT was bent and deformed but it was not cut. Figure 6.26 shows another free standing CNT that was successfully shortened using localized CNT cutting, demonstrating the utility of our method to edit even free standing CNTs. The tests were conducted with beam energy of 5 keV, sample current of 100 pA, and chamber pressure of 1×10^{-5} Torr. The nozzle-sample distance was measured to be 75 μm. The difficulty of cutting free standing CNTs without a surface in the background is associated with the lack of secondary and backscattered electrons which reduces the electron flux available for etching. This explains the need to operate at higher beam currents when cutting free standing CNTs. For equivalent conditions (beam energy of 5 keV, nozzle-sample distance of 75 μm, average chamber pressure of $1\text{-}5\times10^{-5}$ Torr) the CNT laying on the surface required only 15 pA of beam current to cut (see Table 6.2) while the required beam current for cutting a free standing CNT was 100 pA, a 7X more beam current. Another difficulty with editing free standing CNTs is the lack of tension to hold the CNT steady under the electron beam line scan. Double suspended CNTs and CNTs laying on a surface both have the required tension. Figure 6.25 shows how the CNT gets deformed and bend without the presence of CNT tension.

Figure 6.25: (a) shows two free standing CNTs with different diameter. After an initial etching attempt the thinner CNT was completely etched away while the thicker CNT was unchanged (b). After some additional etching time the thicker CNT was bent and deformed but it was not cut (c).

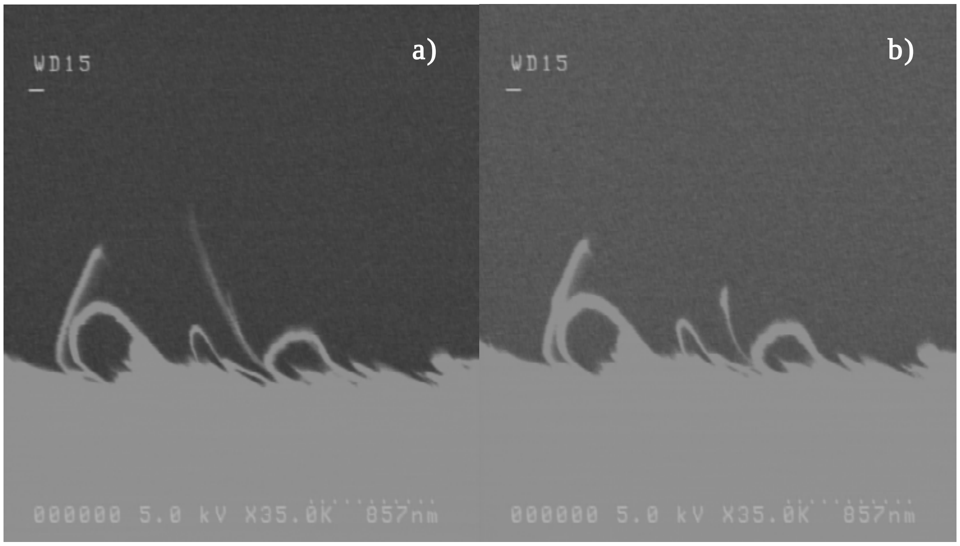

Figure 6.26: A free standing CNT, before (a) and after its length was shortened (b) using localized CNT cutting.

6.2.2.5 Application of the CNT Etching on a Field Emission Device

We demonstrated carbon nanotube etching process that works for editing of a carbon nanotube based device that we fabricated. In particular, we demonstrated utilization of the selective CNT etching process for editing a lateral (horizontal) CNT-based device like the one shown in Figure 6.27. Figure 6.28 shows the result of using selective CNT etching to remove an extra CNT extending from a silicon post to the substrate. The ability to remove excess CNTs (which are there due to the imperfections of the growth process) is critical for CNT based prototype development because such excess CNTs can result in unwanted operation or otherwise interfere with electrical or mechanical device performance.

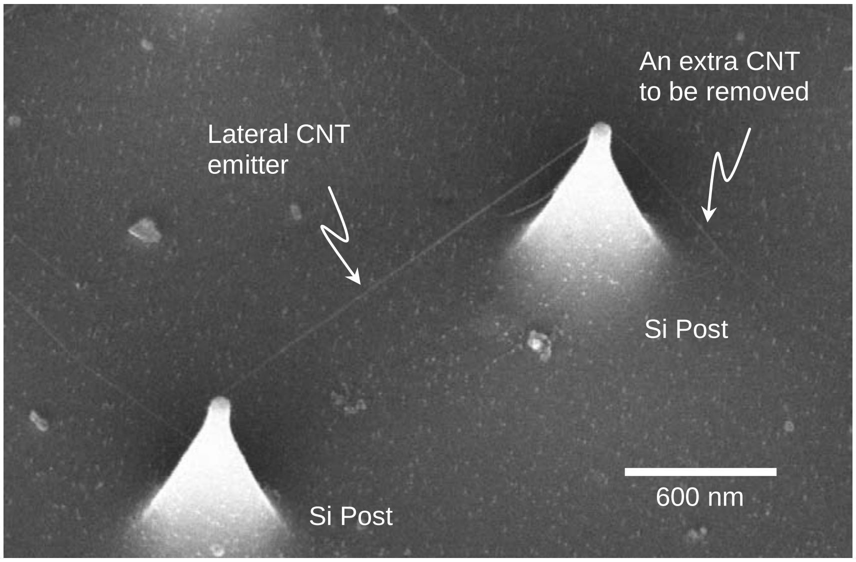

Figure 6.27: Example of a lateral (horizontal) CNT device fabricated by Xidex for use as a lateral field emitter

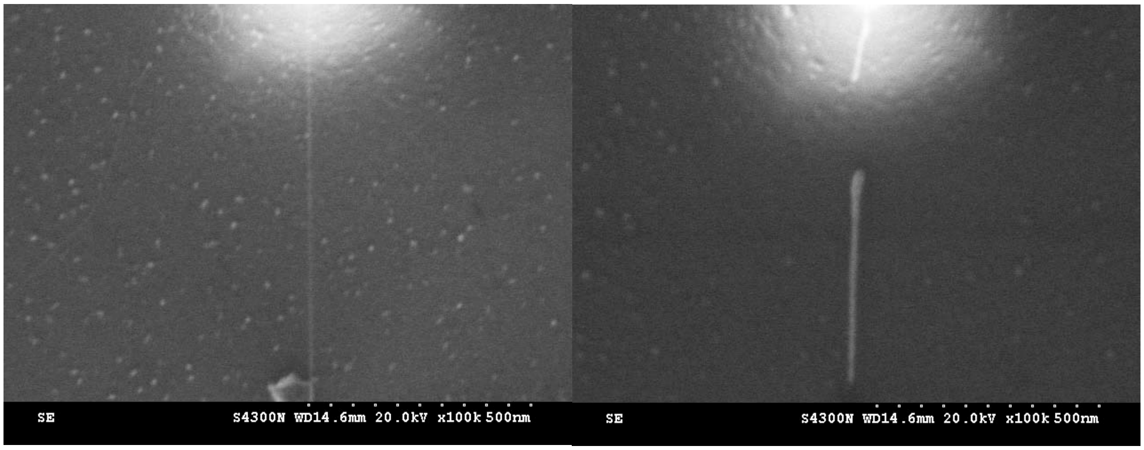

Figure 6.28: An excess CNT strung from a silicon post (viewed top down) and the surface, before (left) and after (right) it was removed using selective CNT etching.

6.2.2.6 Modeling of the CNT Cutting Process

A continuum model developed by our collaborators at The University of Tennessee, at Knoxville [6.17], is used to model the etch rate of the CNT. The rate equation for the precursor gas concentration is:

$$\frac{dN_A}{dt} = g\,\Gamma_{mol}\left(1 - \frac{N_A}{z}\right) - \frac{N_A}{\tau_A} - \frac{A_\sigma\,\Gamma_e\,N_A}{z} \qquad \text{(Eq. 6.6)}$$

Where N_A is the precursor gas concentration, g is the sticking coefficient, Γ_{mol} is the molecular flux on the surface (also the molecular impingement rate), Z is the surface adsorption site density, τ_A is the surface residence time of the precursor gas molecule, A_σ is the probability of electron induced dissociation, and Γ_e is the electron flux. The steady state solution for the etching rate is:

$$Etch\ Rate \propto \frac{\chi\,A_\sigma\,\Gamma_e\,g\,\Gamma_{mol}}{g\,\Gamma_{mol} + \frac{Z}{\tau_A} + A_\sigma\,\Gamma_e} \qquad \text{(Eq. 6.7)}$$

Where χ is the stoichiometry factor relating the number of etch product molecules generated per precursor molecules consumed. The surface residence time can be calculated from:

$$\tau_A = \frac{1}{\nu} e^{\frac{E_{ads}}{k\,T}} \qquad \text{(copy of Eq. 6.3)}$$

Where ν is the fundamental vibrational frequency on the order of 10^{13} s^{-1}. Using a published value of the energy of adsorption for water on carbon nanotubes of ~30 kJ/mol, we arrive at a surface residence time about 15 nanoseconds. If we assume a site density around 10^{15} cm^{-2}, then the middle term of the denominator in the etch equation (Z/τ_A) is around 6.4×10^{22} $cm^{-2}\ s^{-1}$. The pressure of water in the chamber is 2.0×10^{-2} Pa, this corresponds to a molecular flux (molecular impingement rate) of around 9.6×10^{16} $cm^{-2}s^{-1}$. Even using a sticking coefficient of 1.0, the first term in the denominator is very small compared to the second term, and so it can be ignored. Calculating a peak electron flux of about 8.5×10^{21} $cm^{-2}s^{-1}$ for a 1 nA beam at 20 keV, the third term ($A_\sigma\,\Gamma_e$) is about an order of magnitude or more less (depending on A_σ) than (Z/τ_A), so the etch rate equation can be simplified to:

$$Etch\ Rate \propto \frac{\chi\ A_{\sigma}\ \Gamma_e\ g\ \Gamma_{mol}}{\frac{Z}{\tau_A}} = \frac{\chi\ A_{\sigma}\ \Gamma_e\ g\ \Gamma_{mol}\ \tau_A}{Z} \qquad \text{(Eq. 6.8)}$$

Therefore, the etch rate is proportional to the electron flux, the molecular flux, and the surface lifetime of the precursor gas molecule. Increasing the beam current by passing more current through the limiting aperture with the condenser lens makes the probe shape become brightness limited, and further increases to current do not increase the peak electron flux, but rather the width of the beam. Assuming a maximum electron flux of 1×10^{23} $cm^{-2}s^{-1}$, a simulation of etch rate versus impingement rate follows. Using Eq. 6.8, simulated results of the effect of molecular flux (and with it the localized pressure via Eq. 6.1) on the etching rate are shown in Figure 6.29. As can be observed, as the molecular flux (localized pressure) increases, the etch rate increases. The simulation reveals that it would be desirable to design a system that operates at a higher localized pressure in order to increase the gas coverage of water and thus increase the etching rate. This follows the observed experimental behavior.

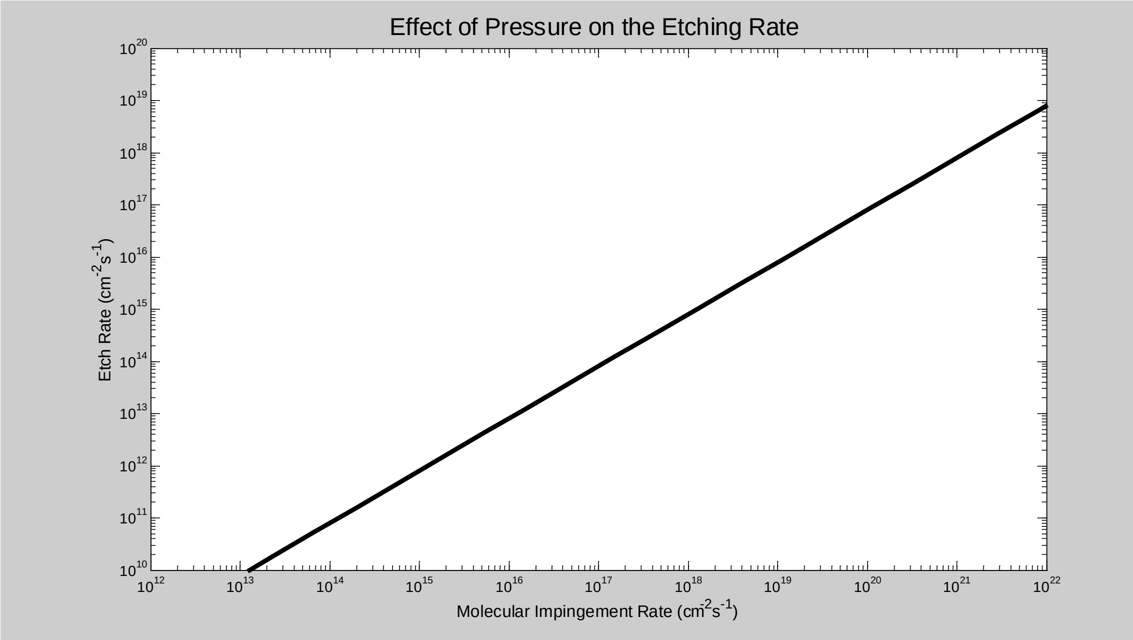

Figure 6.29: Effect of pressure on the etching rate

6.3 SUMMARY AND CONCLUSIONS

We tested the workspace of the relevant electron beam parameters by determining their role in the electron-beam-based carbon nanotube etching process. In particular, we tested the beam current and the beam energy at fixed scanning rates and fixed precursor parameters (pressure and precursor gas). The results indicated that both electron beam parameters are significant. We observed that the etch rate improves with increasing beam current. However, we found that the energy dependence shows a quadratic effect that likely is explained by the energy dependence of the dissociation probabilities of the deposition and etch precursors.

The scanning parameters were also investigated. It was found that we needed a short e-beam dwell time to keep a proper balance between the precursor molecule refresh rate and the beam current. TV scan rates, 30 loops per second in a line scan mode, were found to be nearly optimal. For the pressure range used in our experiments the precursor sticking (gas coverage on the surface) was minimal which did not allow enough sensitivity for us to perform a more detailed investigation of the scan parameters.

Therefore, the options we had available for improving the CNT etching efficiency were the electron beam energy and current. Optimized carbon nanotube etching required 20 keV beam energy or higher at beam currents of 100 pA or more and TV scan rates of imaging. Electron beam energy and current are functions of the SEM instrument and can be optimized within the available limited ranges of the tool. However the localized precursor pressure parameter can be more easily adjusted.

We observed the effects of varying the localized precursor pressure and flux. The background pressure range was from $5.0\text{x}10^{-4}$ Pa (the base pressure without any precursor gas) to $2.0\text{x}10^{-2}$ Pa. The best pressure was found to be the maximum SEM chamber pressure $2.0\text{x}10^{-2}$ Pa with the precursor injected into the chamber by a needle approximately 1 mm above the sample. Simulation of the gas flow indicates that the local pressure at the surface under the injection needle is 10-100 times the background pressure in the chamber. Higher background pressure is desired. However, it would have required operating the SEM in an environmental mode, which would have introduced imaging complications. Lower background pressures resulted in net deposition on the carbon nanotubes instead of net etching.

Our results have shown that higher local precursor pressure (the molecular partial pressure) requires less electron beam current and electron beam energy to achieve the same CNT etching efficiency. Therefore, it is desirable to increase the CNT etching efficiency by increasing the local precursor pressure and flux but without increasing the chamber pressure. This was achieved by decreasing the nozzle-sample distance to below 100 μm by using a nozzle on a nano-manipulator approach to achieve higher localized precursor pressure and flux while maintaining lower chamber pressure. Because the gas flow from a nozzle spreads in a spatial cone, for a fixed gas flow the pressure (force over unit area) and the flux (flow over unit area) increased for decreased nozzle-sample distance.

We demonstrated a versatile carbon nanotube process that works for different carbon nanotube samples. We demonstrated cutting of individual and multiple carbon nanotubes, and we demonstrated line cutting and area cutting (cleaning) of carbon nanotubes. Furthermore, we investigated the difference between CNTs lying on a surface and CNTs protruding from the surface, as well as doubly supported CNTs (as opposed to free standing cantilevered CNTs). We found that it was more efficient to etch CNTs lying on the surface and to etch doubly supported CNTs than it was to etch free standing (cantilevered) CNTs.

We investigated the cutting time as a function of carbon nanotube diameter. We found that the time to cut the tube varies roughly linearly with the beginning size of the tube. Typical cutting time ranged from 40 to 400 sec for CNTs with diameters ranging from 15 to 35 nm.

It is common in all SEMs to have carbon deposition during exposure to the electron beam and this creates immobile deposits of carbon on the CNTs (the samples). The carbon deposition process is competitive with the etching process, and in order to result in a net etching rate, the competitive deposition must be overcome. Increasing the beam current, energy, pressure and flux all contribute to increasing the etching rate and reducing the etching time. In addition, we developed a new pre-etching procedure that improves the efficiency of the CNT etching process. In this procedure the SEM chamber and the CNT samples are cleaned with oxygen plasma to remove carbon-containing species from the SEM chamber and the sample itself. A full factorial experiment was conducted to investigate the effects of the plasma cleaning time together with the beam current and energy. Increasing the cleaning time improves the etching performance as the source of carbon contamination is reduced.

We demonstrated that the etching time and rate improved for a smaller gap between the sample and the nozzle. Because the smaller nozzle distance shows faster etching rates and lower sample currents, the results lead to a conclusion that the local pressure is responsible for the increased etching rate and not the sample current.

We designed and built an enhanced gas delivery system incorporated into a nanomanipulator which enabled precise and close up gas delivery and successfully operating the system in Hitachi S-4000 non-environmental SEM. Design of the enhanced micro gas injection system was facilitated by experiments and modeling conducted using an electron beam induced deposition and etching system located at the University of Tennessee. With the help of another 3-axis nanomanipulator we anticipate doing more complex experiments where one nanomanipulator is dedicated to a gas delivery system and the other to manipulation or electrical or mechanical probing. For example, this system can be used for fabricating and testing CNT emitters in a single SEM chamber without exposing the CNT emitter to the atmosphere.

We showed a series of plots that were calculated to estimate the enhanced flux that can be realized as a function of the distance and angle that the nozzle is relative to the substrate/etching object. General trends that can be observed from the simulation output are that factors that promote higher localized pressure (or higher enhancement) are: decreased distance from nozzle to substrate, increased angle (i.e. normal to etching surface), and lower gas spread angle.

Appendices

APPENDIX A: MANUAL FABRICATION OF A CARBON NANOTUBE TIP

This Appendix describes the procedure of how to manually fabricate a carbon nanotube (CNT) tip on an atomic force microscopy (AFM) silicon (Si) based tip or on a sharpened tungsten (W) tip. We describe the fabrication procedure using a commercially available nanomanipulator from Xidex Corp., NanoBot NX-2000 (www.xidex.com), and therefore use terminology unique to this instrument. However, the outlined fabrication procedure can be accomplished using other commercial or custom made nanomanipulators.

The described procedure was also recorded with a video and was posed on YouTube (www.youtube.com/watch?v=Yefhs7vwToo).

A1 Introduction

A CNT manually attached to the end of a conventional silicon AFM tip, as shown in Figure A1, enables scanning with higher spatial resolution and less tip wear than would otherwise be possible. Use of a stable nanomanipulator, such as the NanoBot system, offers exceptional ease of use and mechanical stability to make it possible to quickly accomplish this difficult and meticulous nanofabrication task inside a scanning electron microscope (SEM).

Figure A2 shows a NanoBot nanomanipulator, Model NX-2000, which has two XYZ positioners, mounted on the door assembly of an SEM. This mounting option leaves the SEM sample stage free for use in the nanofabrication process. Only one of the XYZ positioners is required to fabricate a CNT AFM tip using the method described here.

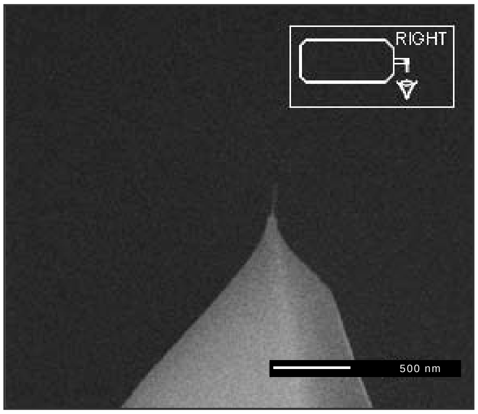

Figure A1: CNT manually attached to a Si AFM tip.

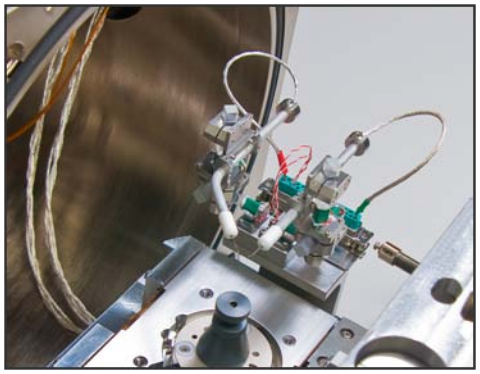

Figure A2: A NanoBot Model NX-2000 mounted on the door assembly of an SEM.

A2 Sample Preparation

A CNT source and an AFM tip are mounted on a standard SEM sample holder using SEM tape as shown in Figure A3. Multiple AFM tips can also be mounted this way for batch fabrication. The CNT source is a silicon chip on which CNTs have been grown using chemical vapor deposition (CVD). This sample was fabricated by Xidex Corp.

Alternatively, a loose bundle of CNTs can be used as a source instead of a substrate with grown CNTs. For example, the CNT source can be a razor blade with bulk CNTs dispensed on its edge by running the blade into a powder of bulk CNTs. Bulk CNTs can for example be purchased from Cheap Tubes Inc. (www.cheaptubesinc.com).

A sharp tungsten (W) tip is mounted on the NanoBot end effector, as shown in Figure A4. The SEM door is then closed and the sample chamber is pumped down.

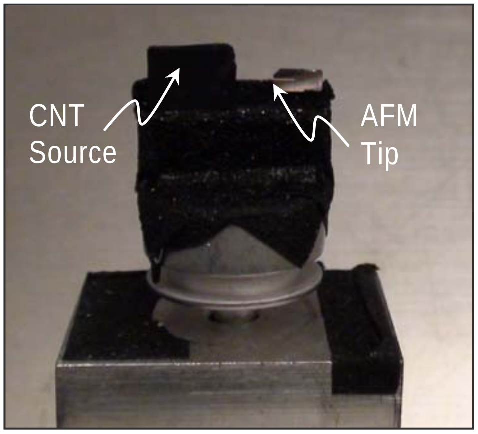

Figure A3: AFM tip and CNT source

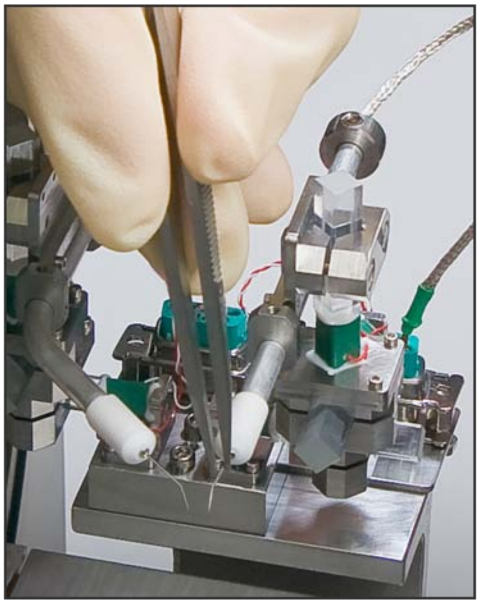

Figure A4: Mounting of a sharp W tip on the NanoBot end effector.

A3 Picking Up a CNT with the W Tip

Nanomanipulator motion control in all three axes was accomplished with a joystick interface. There are three modes of linear motion, each with a different level of speed. The NanoBot's Multi Step mode was used to rapidly maneuver the W tip in XYZ toward the CNT source as shown in Figure A5. Multi Step mode enabled up to 15 mm of XYZ travel. Both Multi Step mode and Single Step mode were used to maneuver the W tip until it is within a few µm of the source of CNTs. Single Step travel was adjustable from 100 nm to 2 µm. The CNT source was then examined by moving the SEM stage until a straight CNT is found which is extending outward so that it can be easily accessed as shown in Figure A6. This procedure typically requires only a few minutes. The NanoBot system's Fine Motion mode is then used to touch the W probe to the selected CNT, as shown in Figure A7. The required high degree of mechanical stability is enabled by the NanoBot system's extremely low drift, on the order of 10 nm per minute, in all three axes. The Fine Motion mode enables ± 3.5 µm of motion with 1 nm resolution in XYZ. It normally takes about 30 seconds to bring the W tip into well oriented contact with a selected CNT. Next, the CNT is welded to the W tip using electron beam induced deposition (EBID) of carbon. In this procedure it is assumed that the SEM chamber is somewhat contaminated with hydrocarbon. In the EBID procedure the magnification of the SEM is set to about 100 kx so that the CNT-tip junction is in full view of the SEM monitor, and the beam energy is set to 10 keV. After 30 to 60 seconds of imaging we have actually deposited carbon from the SEM contamination and covered over the CNT and W tip.

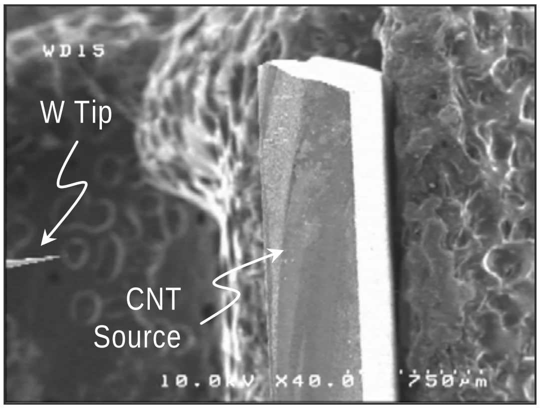

Figure A5: W tip approaching CNT source.

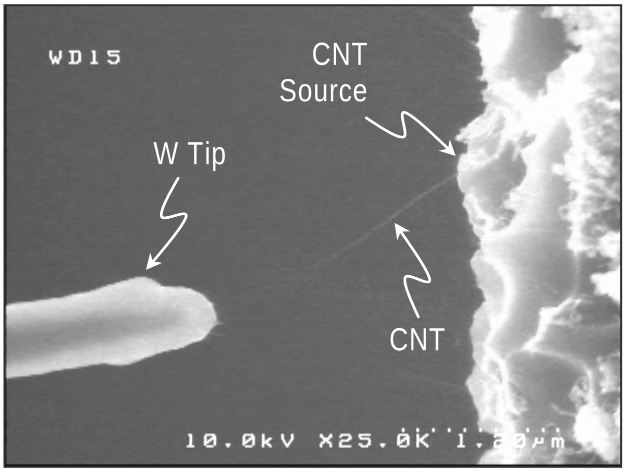

Figure A6: W tip maneuvered to within a few µm of a CNT.

A4 Separating the CNT from the CNT Source

One way to separate the CNT from the CNT source substrate (as shown in Figure A8), is to apply an electrical current pulse between the W probe and the substrate. In this procedure we connected a Keithley 237 current-voltage source to the W probe and electrically grounded the SEM holder. We then manually applied a current pulse of 1-5 µA to the W probe for 1-2 seconds, basically turning the power supply on and off immediately. More sophisticated electrical cutting can be accomplished by writing LabView based code that turns on and off the power supply with 1 ms precision.

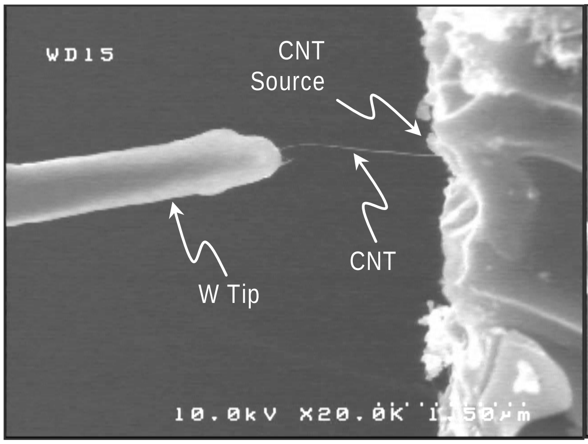

Figure A7: W tip in contact with the selected CNT.

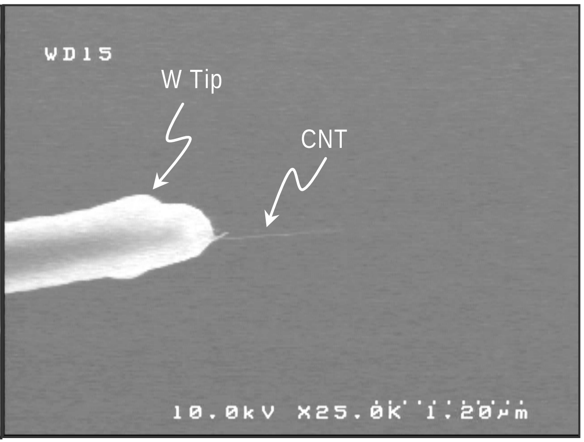

Figure A8: CNT separated from substrate using current pulse.

It has to be noted that the location of the CNT cutting using this procedure is not very accurate because the CNT probably cuts at the location along the CNT where the resistance is the highest due to possible defects in the lattice of the CNT molecule.

In the case where the CNT source consisted of loose bundle of CNTs (instead of a substrate with grown CNTs), the CNT connected to the W tip could be pulled away from the bundle without the need for electrical cutting.

This procedure completes the fabrication of a CNT tip on a sharp W probe. In this work this was the procedure we used to manually fabricate CNT emitters on a sharp W wire. The next few steps describe how to now manually mount the CNT to an AFM tip.

A5 Attaching the CNT to the AFM Tip

The W tip carrying the CNT is rapidly translated in XYZ to within a few microns of the AFM tip apex, as shown in Figure A9. The NanoBot system's Fine Motion mode, is then used to place the CNT along the side of the silicon AFM tip apex, as shown in

Figure A10. The dexterity of the NanoBot system makes it fairly easy to align the CNT with respect to the AFM tip in XYZ. A reasonably well aligned CNT AFM tip (e.g., to ± 10º) can be made this way with some amount of practice. The CNT is welded to the AFM tip using EBID of carbon. This procedure was described above.

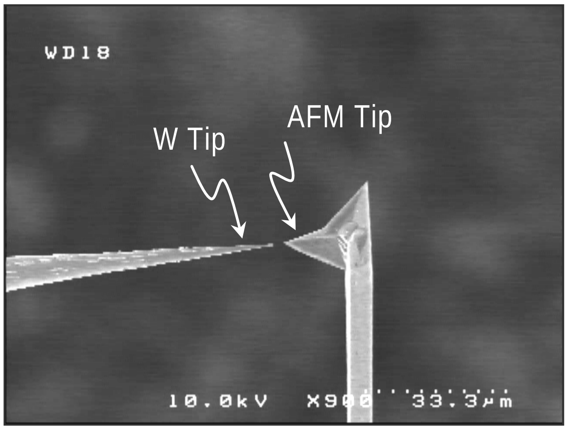

Figure A9: W tip carrying CNT translated to within a few μm of the AFM tip.

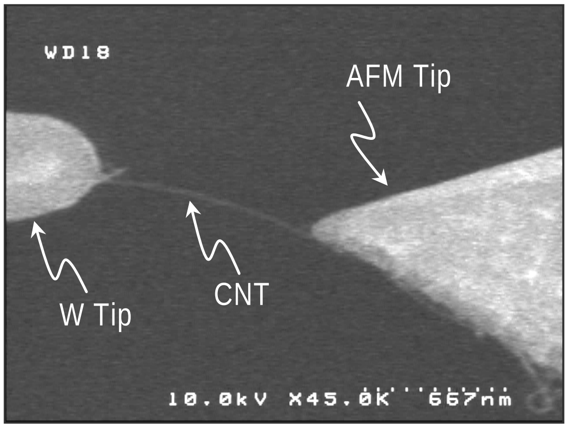

Figure A10: CNT placed along the side of the AFM tip.

A6 Cutting the CNT Away from the W tip

An electrical current pulse is then used to cut the CNT away from the tungsten tip as shown in Figure A.11. This procedure was described above. The electrical cutting procedure did not change because one of the substrates is Si, since the Si in the AFM tip is highly doped and therefore conductive.

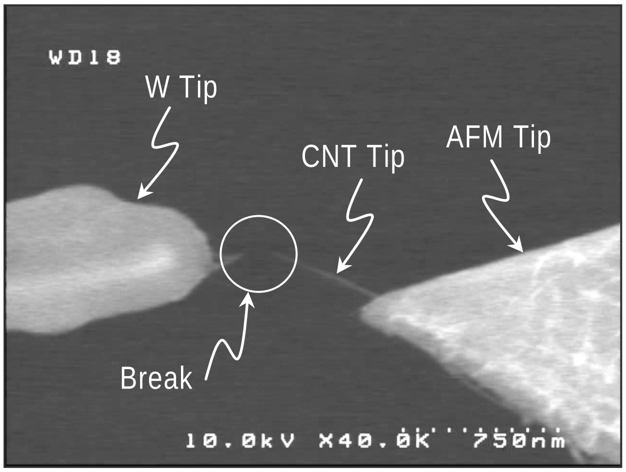

Figure A11: CNT separated from the W tip.

A7 Alternative Procedures

Use of a sharp tungsten tip as an intermediate step, as described above, facilitates selection and detachment of the CNT from its original substrate and also facilitates attachment of the CNT to the AFM tip. Alternatively, a CNT can be attached to an AFM tip in one step if the AFM chip was mounted on the end of the nanomanipulator. However, this procedure may require more operator skill and can be complicated by the presence of other CNTs in the vicinity of the CNT selected for mounting. If additional batches of CNT tips need to be fabricated, they can be mounted on the SEM sample holder by retracting and reinserting the load lock while the NanoBot carrying the W tip remains in the sample chamber. This arrangement avoids the need to pump down the chamber each time a new batch of CNT AFM tips is to be fabricated.

APPENDIX B: EVALUATING THE CONTACT RESISTANCE BETWEEN CARBON NANOTUBES AND W AND SI PROBE TIPS

This Appendix describes the characterization of the electrical properties of conductive carbon nanotube (CNT) scanning probe microscope (SPM) tips. The project results and conclusions were presented at SEMATECH's AMAG/FMAG meeting in Monterrey, California on February 20 & 21, 2008.

B1 Introduction

The objective of this work was to produce CNT SPM tips which are suitable for nanometer scale measurement of carrier concentration profiles. The conductive CNT tips for this project were fabricated using: direct growth of a single carbon nanotube on an AFM silicon tip, manual mounting of a single carbon nanotube on an AFM silicon tip, and manual mounting of a single carbon nanotube on a sharp W wire. These three methods represent three alternative technologies for fabrication of CNT based tips. Typical CNT diameter was less than 10 nm, and typical CNT lengths were 200 nm to 1000 nm but other lengths were feasible.

We electrically characterized CNT tips using current-voltage (*I-V*) measurements. The main instrument used was Keithley 237 current-voltage source. The electrical measurements were conducted while the samples were inside an SEM and right after they were prepared. We used a nanomanipulator to assemble the samples and we used electron beam induced deposition (EBID) of platinum to make electrical connections between the CNTs and the probes. During this evaluation the CNT tip resistivity was determined.

B2 Experiments and Evaluation Procedures

We started our investigation by testing CNTs in contact to different substrates, such as a W tip and a Si tip from an SPM cantilever. The main electrical characterization test was by conducting *I-V* measurements.

The results from electrical characterization of a W tip connected to a single CNT which has been grown on a Si substrate are shown in Figure B1. The CNT is connected to the W tip via the Van der Waals force. The *I-V* curves for the assembled connection (multiple runs) are shown in Figure B1-b. The large flat region from -4 to 4 V indicated existence of a Schottky barrier resistance in the electrical circuit. Most probably the Schottky barrier is between the W tip and the CNT but may also exist between the CNTs and the Si substrate on which they were grown. The non-symmetry of the *I-V* curve indicated that the results are from real Schottky barriers.

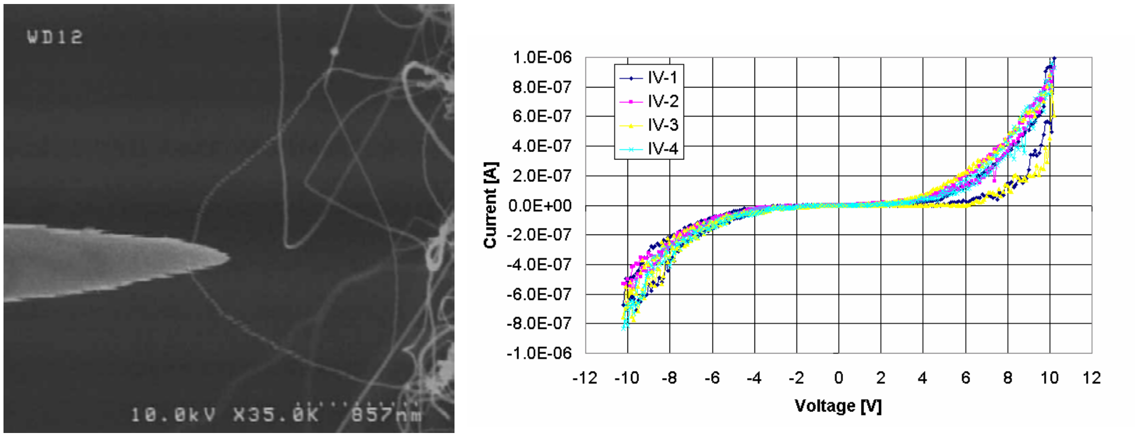

Figure B1: Electrical characterization of W tip to a CNT nanowire grown on Si. a) SEM image of the physical connection, b) *I-V* curves from the electrical measurement.

The results from electrical characterization of a CNT mounted on a W tip and in contact with a Si tip via the Van der Waals force are shown in Figure B2. The *I-V* curves are shown for the assembled W–CNT–Si Tip connection (Figure B2-b). Again, the flat region from -4 to 4 V indicated an existence of a Schottky barrier resistance in the electrical circuit. The measurement noise is better in this test (compared to the previous test) because there is probably better contact between a single CNT and the W and Si substrates with more of the CNT contacting both substrates.

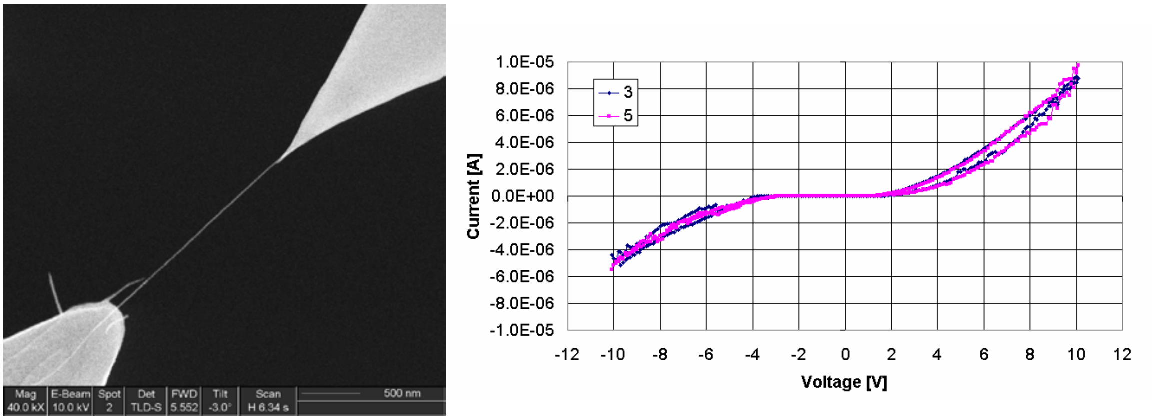

Figure B2: Electrical characterization of W tip to a CNT tip manually attached to the W and the Si tip. a) SEM image of the physical connection, b) *I-V* curves from the electrical measurement.

Our next goal was to eliminate one of the substrates (the silicon) and observe the change in the *I-V* measurements. First we confirmed that a contact between two W tips is very Ohmic and results in a linear *I-V* curve with resistance of few Ohms. Next, we placed a CNT between the two W probes. The results from electrical characterization of a single CNT connected between two W tips are shown in Figure B3. The CNT is connected to both W tips via Van der Waals force. We repeated this procedure for two different CNTs. The *I-V* curves for the assembled connection for both CNTs are shown in Figure B3-b. The two curves are different due to the different CNT lengths and the quality of their contact. We notice that the flat region in the *I-V* curve due to the existence of a Schottky barrier resistance in the electrical circuit was reduced to less than ± 2 V, indicating that the dominant Schottky barrier in the previous measurements was between the CNT and the Si substrate. Therefore, the remaining Schottky barrier was due to the contact resistance between the CNT and the W.

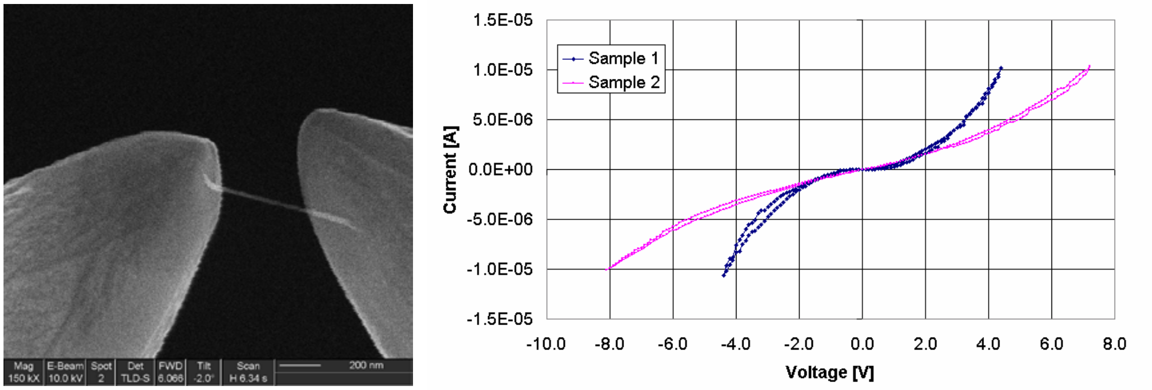

Figure B3: Electrical characterization of CNT manually attached to two W tips. a) SEM image of the physical connection, b) *I-V* curves from the electrical measurement.

The existence of the Schottky barrier resistance was expected but it does not prevent the use of the CNT as an electrical probe. The consequence of having a Schottky barrier is the increased bias voltage that has to be used for electrical measurements and the additional deconvolution of the data after the electrical measurement. Nevertheless, our next goal was to try to reduce the Schottky barrier resistance.

Therefore, in the next tests, we coated (welded) the contacts between the CNT and its substrate. We used a localized e-beam deposition technique inside an SEM tool to deposit Pt contacts to the CNT ends with nanometers precision. We repeated this test for two different CNTs. Results showing the effect of Pt welding on electrical characteristics of a W-CNT-W connection are shown in Figure B4. The *I-V* curves for the assembled W-CNT-W connection with Pt welds are shown. The legend shows the following curves:

3 & 1 = CNT is connected to both W tips via Van der Waals force.

6 & 11 = Both CNT-to-W contacts were welded with Pt.

8 & 15 = The W tips and the CNT were covered with a thin layer of Pt.

Legends 3, 6, and 8 refer to a Sample 1 and legends 1, 11, and 15 refer to a Sample 2. It can be seen that the resistivity of the circuit decreased after Pt welding of the W-CNT contacts and the Schottky barrier was almost eliminated. It can be seen that even for a completely Pt coated CNT there are still nonlinearities in the IV curve. This may be due to the non-complete coating process or due to the CNT wire resistance that is now in parallel to the Pt wire resistance.

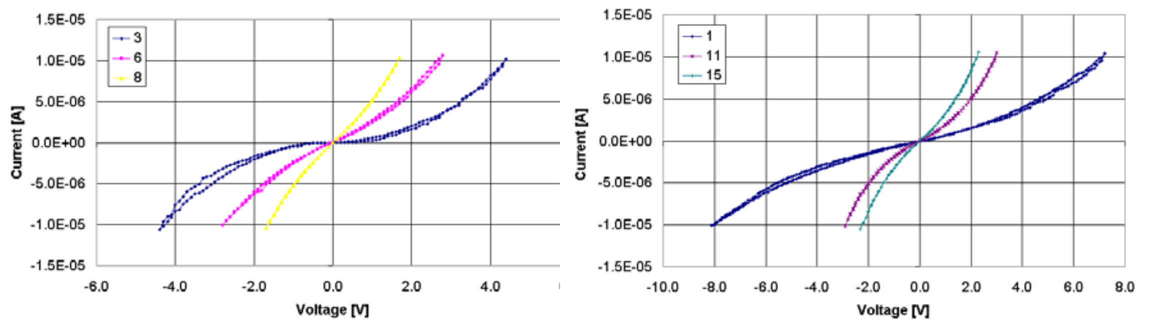

Figure B4: I-V results showing the effect of Pt welding (via electron induced precursor deposition) on electrical characteristics of a W-CNT-W connection. a) I-V curves for Sample 1 and b) for Sample 2.

Better understanding of the results is possible if we normalize the results accounting for the diameter and the length of the CNT. The resisitivity can be computed as:

$$\rho = R\frac{A}{L}\frac{1}{10^7} \qquad \text{(Eq. B1)}$$

where R is the measured resistance (Ω), L is the CNT length (m), A is the CNT gross section area (m^2), and ρ is the resisitivity (Ω-cm).

The effect of Pt welding on probe resistivity is shown in Figure B5, where we compare the probe resistivities before and after the Pt welding. The resistivity decreased after welding the W-CNT contacts with Pt. For Sample 1 (Figure B5a), the average resistivity dropped from 0.0335 to 0.0052 Ω-cm. For Sample 2 (Figure B5b), the average resistivity dropped from 0.0152 to 0.0061 Ω-cm.

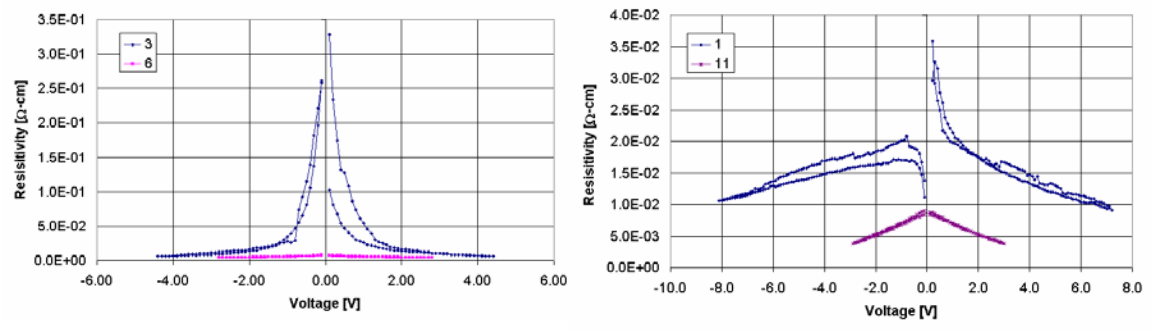

Figure B5: Comparative results showing the electrical characteristics of a W-CNT-W connection before (legend 3 and 1) and after Pt welding (legend 6 and 11). a) *I-V*curves for Sample 1 and b) for Sample 2.

Figure B6 shows the effect of Pt welding on the minimum resistivity of a W-CNT contact. For Sample 1, minimum resistivity dropped down to 0.0058 Ω-cm. For Sample 2, minimum resistivity dropped down to 0.0037 Ω-cm. For comparison, commercially available SPM probes for electrical measurements have resisitivities from 0.01 to 0.025 Ω-cm. In essence our probes are very conductive and compatible to or better than existing electrical probes.

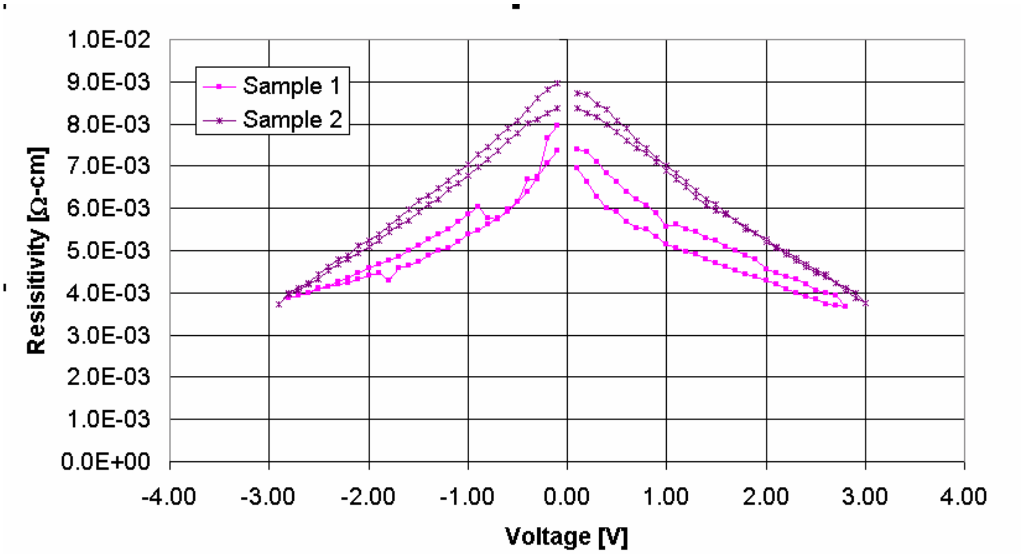

Figure B6: Minimum resistivity of a W-CNT contact dropped after the CNT was welded to the W with Pt.

B3 Conclusions

We have measured the CNT-probe resistance on 20-30 CNTs as grown directly on a Si substrate using *I*-*V* measurements. We recorded the overall measured resistance *R*. Because each CNT had a different length and diameter we did not report the resisitivity number. The typical CNT-probe resistance *R* was 500 kΩ and the minimum measured CNT-probe resistance *R* was 30 kΩ. This is well above the theoretical CNT resistance of a CNT which is 6.7 kΩ. We contribute the extra resistance to the contact resistance between the CNT and the substrate. The minimum measured probe resistivity ρ was 0.0037 Ω-cm. The resistivity of the conductive CNT probes is compatible to the existing metal coated Si tips or better, but with electrical properties and shape that are not expected do not degrade with use.

The research work presented here was partially funded by SEMATECH project number MFGM049M.

References

[2.1] R. H. Fowler and L. Nordheim, *Electron Emission in Intense Electric Fields,* Proc. R. Soc. Lond. A 1928 119, 173-181

[2.2] J. W. Gadzuk and E. W. Plummer, Field *Emission Energy Distribution (FEED),* Review of Modern Physics Vol. 45, No. 3, July 1973, p. 487

[2.3] Hawkes, P. W. & Kasper, E. 1996 Applied geometrical optics. Principles of electron optics, Vol. II. Academic.

[2.4] Saito, R., Dresselhaus, G. & Dresselhaus, M. S. 1998 Physical properties of carbon nanotubes. London: Imperial College Press.

[2.5] N. de Jonge, *Brightness of carbon nanotube electron sources*, J. of Applied Physics, Vol. 95, No. 2, Jan. 2004, 673-681.

[3.1] http://www.xidex.com/products/nanobot.html

[3.2] http://www.xidex.com/products/parallel-gas-injection-system.html

[4.1] Vladar, Andras E., Zsolt Radi, Michael T. Postek, and David C. Joy, *Nano-Tip Electron Gun for the Scanning Probe Electron Microscope,* prepublication manuscript of NIST report.

[4.2] N. de Jonge, J.-M. Bonard, *Carbon nanotube electron sources and applications,* Phil. Trans. R. Soc. Lond. A (2004) 362, 2239-2266.

[4.3] J.-M. Bonard, J.-P. Salvetat, T. Stockli, L. Forro, A. Chatelian, *Field emission from carbon nanotubes: perspectives for applications and clues to the emission mechanism*, Applied Physics A, 69 (1999), 245-254.

[4.4] Purcell, S. T., and N. Garcia, *64 meV measured energy dispersion from cold field emission nanotip,* Applied Physics Letters, Vol. 67, No. 3, 17 Jul 1995, 436-438.

[4.5] J.-M. Bonard, F. Maier, T. Stockli, A. Chatelian, W.A. de Heer, J.-P. Salvetat, L. Forro, *Field emission properties of multiwalled carbon nanotubes,* Ultramicroscopy 73 (1998), 7-15.

[4.6] W. Qian, M.R. Scheinfein, J.C.H. Spence, *Brightness measurements of nanometer-sized field-emission-electron sources*, J. of Applied Physics, 73(11), Jun. 1993, 7041-7045.

[4.7] A.H.V. van Veen, C.W. Hagen, J.E. Barth, P. Kruit, *Reduced brightness of the ZrO/W Schottky electron emitter*, J. Vac. Sci. Technol. B 19(6) Nov/Dec 2001, 2038-2044.

[4.8] N. de Jonge, *Brightness of carbon nanotube electron sources*, J. of Applied Physics, Vol. 95, No. 2, Jan. 2004, 673-681.

[4.9] N. de Jonge, N.J. de Druten, *Field emission from individual multiwalled carbon nanotubes prepared in an electron microscope,* Ultramicroscopy 95 (2003), 85-91.

[4.10] N. de Jonge, Y. Lamy, K. Schoots, T.H. Oosterkamp, *High brightness electron beam from a multi-walled carbon nanotube,* Nature, Vol. 420, Nov. 2002, 393-461.

[4.11] K. Hata, A. Takakura, A. Ohshita, Y. Saito, *Brightness of electron beam emitted from a single pentagon on a multiwall carbon nanotube tip,* Surf. Interface Anal. 36 (2004), 506-509.

[4.12] M.A. Guillorn, A.V. Melechko, V.I. Merkulov, E.D. Ellis, C.L. Britton, M.L. Simpson, D.H. Lowndes, *Operation of a gated field emitter using an individual carbon nanofiber cathode,* Applied Physics Letters, Vol. 79, No. 21, Nov. 2001, 3506-3508.

[4.13] Edgecombe, Christopher John, and Ugo Valdre, *Field emission and electron microscopy*, Microsc. Microanal. 6, 380-387, 2000.

[4.14] K.A. Dean, B.R. Chalamala, *The environmental stability of field emission from single-walled carbon nanotubes,* Applied Physics Letters, Vol. 75, No. 19, Nov. 1999, 3017-3019.

[4.15] D.S. Hsu, J.L. Shaw, *Regeneration of gated carbon nanotube field emission*, J. Vac. Sci. Technol. B 23(2) Mar/Apr 2005, 694-697.

[4.16] D.S. Hsu, J. Shaw, *Integrally gated carbon nanotube-on-post field emitter arrays,* Applied Physics Letters, Vol. 80, No. 1, Jan. 2002, 118-120.

[4.17] M.J. Fransen, Th.L. van Rooy, P. Kruit, *Field emission energy distributions from individual multiwalled carbon nanotubes*, Applied Surface Science 146 (1999), 312-327.

[4.18] Utsumi, T., *Keynote Address, Vacuum Microelectronics: What's New and Exciting,* IEEE transactions on Electron Devices, Vol. 38, No. 10, October 1991, 2276-2283

[4.19] A.V. Melechko, V.I. Merkulov, T.E. McKnight, M.A. Guillorn, K.L. Klein, D.H. Lowndes, M.L. Simpson, *Vertically aligned carbon nanofibers and related structures: Controlled synthesis and direct assembly,* J. of Applied Physics, Vol. 97, 041301, 2005.

[4.20] M.A. Guillorn, A.V. Melechko, V.I. Merkulov, E.D. Ellis, M.L. Simpson, D.H. Lowndes, L.R. Baylor, G.J. Bordonaro, *Microfabricated field emission devices using carbon nanofibers as cathode elements*, J. Vac. Sci. Technol. B 19(6) Nov/Dec 2001, 2598-2601.

[4.21] http://www.xidex.com/downloads/finish/3/7.html

[4.22] http://www.youtube.com/watch?v=Yefhs7vwToo

[4.23] B.C. Park, K.Y. Jung, W.Y. Song, B. O, and S. Ahn, *Bending of a Carbon nanotube in Vacuum Using a Focused Ion Beam*, Advanced Materials 2006, 18, 95-98.

[4.24] NanoScience Instruments, Phoenix, Arizona, **www.nanoscience.com**

[4.25] P.N. Minh, L.T.T.Tuyen, T. Ono, H. Miyashita, Y. Suzuki, H. Mimura, M. Esashi, *Selective growth of carbon nanotubes on Si microfabricated tips and application for electron field emitters*, J. Vac. Sci. Technol. B 21(64) Jul/Aug 2003, 1705-1709.

[4.26] J. Zhang, J. Tang, G. Yang, Q. Qiu, L-C Qin, O. Zhou, *Efficient Fabrication of Carbon nanotube Point Electron Sources by Dielectrophoresis*, Adv. Matter. (2004) 16(14) 1219-1222.

[4.28] N. de Jonge, *Brightness of carbon nanotube electron sources*, J. of Applied Physics, Vol. 95, No. 2, Jan. 2004, 673-681.

[4.29] N. de Jonge, N.J. de Druten, *Field emission from individual multiwalled carbon nanotubes prepared in an electron microscope*, Ultramicroscopy 95 (2003), 85-91.

[4.30] N. de Jonge, Y. Lamy, K. Schoots, T.H. Oosterkamp, *High brightness electron beam from a multi-walled carbon nanotube*, Nature, Vol. 420, Nov. 2002, 393-461.

[4.31] K. Hata, A. Takakura, A. Ohshita, Y. Saito, *Brightness of electron beam emitted from a single pentagon on a multiwall carbon nanotube tip*, Surf. Interface Anal. 36 (2004), 506-509.

[4.31] R. Morin, H.-W. Fink, *Highly monochromatic electron point-source beams*, Applied Physics Letters, Vol. 65 (18) Oct. 1994, 2362-2364.

[4.32] F. Charbonnier, *Arcing and voltage breakdown in vacuum microelectronics microwave devices using field emission arrays: Causes, possible solutions, and recent progress*, J. Vac. Sci. Technol. B 16(2) Apr 1998, 880-887.

[5.1] W.I. Milne, K.B.K. Teo, E. Minoux, O. Groening, L. Gangloff, L. Hudanski, J-P. Schnell, D. Dieumegard, F. Peauger, I.Y.Y. Bu, M.S. Bell, P. Legagneux, G. Hasko, G.A.J. Amaratunga, *Aligned carbon nanotubes/fibers for applications in vacuum microwave amplifiers*, J. Vac. Sci. Technol. B 24(1) Jan/Feb 2006.

[5.2] J.-M. Bonard, F. Maier, T. Stockli, A. Chatelian, W.A. de Heer, J.-P. Salvetat, L. Forro, *Field emission properties of multiwalled carbon nanotubes*, Ultramicroscopy 73 (1998), 7-15.

[5.3] Z. Chen, G. Cao, Z. Lin, and D. den Engelsen, *Synthesis and emission properties of carbon nanotubes grown by sandwich catalyst stacks*, J. Vac. Sci. Technol. B 24(2) Mar/Apr 2006.

[5.4] C. Bower, D. Shalom, W. Zhu, D. Lopez, G.P. Kochanski, P.L. Gammel, and S. Jin, *A micromachined vacuum triode using a carbon nanotube cold cathode*, IEEE Transactions on Electron Devices 49(8) August 2002.

[5.5] H.M. Manohara, M.J. Bronikowski, M. Hoenk, B.D. Hunt, and P.H. Siegel, *High-current-density field emitters based on arrays of carbon nanotube bundles*, J. Vac. Sci. Technol. B 23(1) Jan/Feb 2005.

[5.6] L. Nilsson, O. Groening, C. Emmenegger, O. Kuettel, E. Schaller, L. Schlapbach, H. Kind, J-M. Bonard, and K. Kern, *Scanning field emission from patterned carbon nanotube films*, Applied Physics Letters 76(15) April 2000.

[5.7] J.S. Suh, K.S. Jeong, J.S. Lee, I. Han, "*Study of the field-screening effect of highly ordered carbon nanotube arrays*," Applied Physics Letters 80(13) April 2002.

[5.8] G. Chai, L. Chow, *Emission from the side wall of an individual multiwall carbon Nanotube*, Carbon (2006), doi:10.1016/j.carbon.2006.09.030

[5.9] Y. Konishi, S. Hokushin, H. Tanaka, L. Pan, S. Akita, and Y. Nakayama, *Comparison of Field Emission from Side Wall and Tip of an Individual Carbon Nanotube*, Japanese Journal of Applied Physics Vol. 44, No. 4A, 2005, pp. 1648-1651.

[5.10] S.M. Jung, J. Hahn, H.Y. Yung, and J.S. Suh, *Clean Carbon Nanotube Field Emitters Aligned Horizontally*, Nano Letters 2006 Vol. 6, No. 7, 1569-1573

[5.11] Y. Chen, D.T. Shaw, L. Guo, *Field emission of different oriented carbon nanotubes*, Applied Physics Letters, Vol. 76, No. 17, 24 April 2000.

[5.12] http://www.xidex.com/downloads/finish/3/7.html

[5.13] S.J. Randolph, J.D. Fowlkes, P.D. Rack, Critical Reviews of Solid State and Materials Sciences, Vol. 31, p. 55-89 (October 2006)

[5.14] B. Yang, M. S. Marcus, D. G. Keppel, P. P. Zhang, Z. W. Li, B. J. Larson, D. E. Savage, J. M. Simmons, O. M. Castellini, M. A. Eriksson, and M. G. Lagallya, *Template-directed carbon nanotube network using self-organized Si nanocrystals*, APPLIED PHYSICS LETTERS 86, 263107 (2005)

[5.15] Y.J. Jung, Y. Homma, R. Vajtai, Y. Kobayashi, T. Ogino, and P.M. Ajayan, *Straightening Suspended Single Walled Carbon nanotubes by Ion Irradiation*, Nano Letters, 2004, Vol. 4, No. 6, 1109-1113

[5.16] Alan M. Cassell, Nathan R. Franklin, Thomas W. Tombler, Emory M. Chan, Jie Han, and Hongjie Dai, *Directed Growth of Free-StandingSingle-Walled Carbon Nanotubes*, J. Am. Chem. Soc. 1999, 121, 7975.

[5.17] N.R. Franklin and H. Dai, *An Enhanced CVD Approach to Extensive Nanotube Networks with Directionality*, Advanced Materials, 2000, 12, No. 12

[5.18] H.B. Peng, T.G. Ristroph, G.M. Schurmann, G.M. King, J. Yoon, V. Narayanamurti, and J.A. Golovchenko, *Patterned growth of single-walled carbon nanotube arrays from a vapor-deposited Fe catalyst*, Applied Physics Letters, Vol. 83, No. 20, 17 November 2003

[5.19] Goo-Hwan Jeong, Akira Yamazaki, Satoru Suzuki, Hideyuki Yoshimura, Yoshihiro Kobayashi, and Yoshikazu Homma, *Cobalt-Filled Apoferritin for Suspended Single-Walled Carbon Nanotube Growth with Narrow Diameter Distribution*, J. AM. CHEM. SOC. 2005, 127, 8238-8239

[5.20] Goo-Hwan Jeong, Satoru Suzuki, and Yoshihiro Kobayashi, Akira Yamazaki, Hideyuki Yoshimura, Yoshikazu Homma, *Effect of nanoparticle density on narrow diameter distribution of carbon nanotubes and particle evolution during chemical vapor deposition growth*, JOURNAL OF APPLIED PHYSICS 98, 124311 (2005)

[5.21] Wei Zhu, Vacuum Microelectronics, John Wiley & Sons, New York, Chapter 4, 2001.

[6.1] T. Liang and A. Stivers, SPIE Vol. 4688, pg. 375-383 (2002).

[6.2] T. Ogawa, K. Mochiji, I Ochiai, and S. Yamamoto, J. Appl. Phys. 75 (9), 1 May pg. 4680-4685 (1996).

[6.3] M.C. Peigon, Ch. Cardinaud, and G. Turban, J. Appl. Phys. 70(6), 15 September pg. 3314-3323 (1991).

[6.4] S.J. Randolph, J.D. Fowlkes, P.D. Rack, Critical Reviews of Solid State and Materials Sciences, Vol. 31, p. 55-89 (October 2006)

[6.5] M. S. Raghuveer, P. G. Ganesan, J. D'Arcy-Gall, G. Ramanath, M. Marshall, and I. Petrov, Applied Physics Letters 84, 4484-4486 (2004)

[6.6] C. S. Han, J. K. Park, Y. H. Yoon, and Y. H. Shin, Carbon 44, 3375-3378 (2006).

[6.7] D. H. Lien, K. Hsin-Fu, and H. Wen-Kuang, Applied Physics Letters 88, 93113-1 (2006).

[6.8] S. Suzuki and Y. Kobayashi, Chemical Physics Letters 430, 370-374 (2006).

[6.9] J. Hudson, Surface Science: An Introduction, 1992

[6.10] N.R. Franklin and H. Dai, *An Enhanced CVD Approach to Extensive Nanotube Networks with Directionality*, Advanced Materials, 2000, 12, No. 12

[6.11] P. Liu, F. Arai, and T. Fukuda, Applied Physics Letters 89, 113104-1 (2006).

[6.12] T. D. Yuzvinsky, A. M. Fennimore, W. Mickelson, C. Esquivias, and A. Zettl, Applied Physics Letters 86, 053109 (2005).

[6.13] J. Martinez, T. D. Yuzvinsky, A. M. Fennimore, A. Zettl, R. Garcia, and C. Bustamante, Nanotechnology 16, 2493-2496 (2005).

[6.14] P.C. Hoyle, J.R.A. Cleaver, and H. Ahmed, J. Vac. Sci Technol. B 14(2), Mar/Apr pg. 662-665 (1996).

[6.15] M. Toth et al., Journal of Applied Physics, 101, 054309 (2007)

[6.16] http://www.xidex.com/products/parallel-gas-injection-system.html

[6.17] Matthew G Lassiter and Philip D Rack, *Nanoscale electron beam induced etching: a continuum model that correlates the etch profile to the experimental parameters*, Nanotechnology **19** 455306, 2008

Vita

Vladimir Mancevski received his Bachelor of Science in Engineering from The University of Texas at San Antonio in 1990, and his Master of Science in Engineering from The University of Texas at Austin in 1994. In 1997 he co-founded Xidex Corporation to commercialize a novel sensing system that he co-invented while pursuing his graduate studies at UT Austin. While at Xidex he entered the Graduate Program in Physics at UT Austin. At Xidex he has served as the Chief Technology Officer up until today and has been the Principal Investigator of seven SBIR/STTR Phase II research projects and fifteen SBIR/STTR Phase I research projects with NSF, ARO, NIST, and DOE. He holds ten issued US patents, and several pending. He was a recipient of Best Paper awards at the 1994 International Symposium on Robotics and Manufacturing and the 2001 SPIE Conference on Micromachining and Microfabrication. He has been an invited speaker at SPIE in the area of nanofabrication and carbon nanotube tip development and has been invited as a reviewer for the National Science Foundation.

Permanent address: 4806 Alta Loma Drive, Austin TX 78749
This dissertation was typed by Vladimir Mancevski.